

29 January 1982 • Vol. 215 • No. 4532

\$2.50

SCIENCE

AMERICAN ASSOCIATION FOR THE ADVANCEMENT OF SCIENCE



Reports

Voyager 2 Encounter with the Saturnian System

Abstract. An overview of the Voyager 2 encounter with Saturn is presented, including a brief discussion of the trajectory, the planned observations, and highlights of the results described in the subsequent reports.

With the successful accomplishment of its encounter with Saturn, Voyager 2 completed the fourth step in the NASA Voyager program of exploration of the outer planets, which began with the launch of Voyager 2 from Cape Canaveral, Florida, on 20 August 1977 (1). Prior to the closest approach of Voyager 2 to Saturn on 26 August 1981, both Voyager 1 and Voyager 2 had completed successful encounters of Jupiter, with closest approaches occurring on 5 March 1979 and 9 July 1979, respectively (2), and Voyager 1 had preceded its twin through the Saturn system, with its closest approach on 12 November 1980 (3, 4). The

Voyager 2 encounter occurred almost exactly 2 years after the Pioneer 11 encounter on 1 September 1979 (5). This and the following reports summarize the preliminary findings from the scientific investigations conducted during the Voyager 2 passage through the Saturn system.

In order to use a gravity boost at Saturn to propel Voyager 2 on toward a 1986 encounter with Uranus, it was necessary for the spacecraft to arrive at Saturn considerably later than Voyager 1 so that Uranus and Saturn were suitably positioned. As a result, the Voyager 2 flight time to Saturn was just over 48

months and the flight distance almost 2.3 billion kilometers (1.4 billion miles). Voyager 1, on the other hand, completed that portion of its journey in just over 38 months. The slower pace of Voyager 2 permitted a somewhat more leisurely scientific investigation of the interplanetary environment between Jupiter and Saturn and of the Saturn system itself.

The Voyager 2 scientific investigations and principal investigators are identical to those listed for Voyager 1 (3). All instruments, including the Voyager 2 photopolarimeter, functioned nominally during the Voyager 2 encounter of Saturn. Two anomalies during the encounter did affect the acquisition of data, however. The most serious was a temporary cessation of operation of the science instrument scan platform, which points the imaging cameras, photopolarimeter, and infrared and ultraviolet spectrometers. The problem occurred about 110 minutes after Saturn closest approach, while the spacecraft was passing through Saturn's shadow and out of communication with the earth. During the period from Saturn closest approach until almost 5 hours after closest approach, the attitude of the spacecraft was referenced to internal gyroscopes. Because of a gyroscope calibration error, the space-

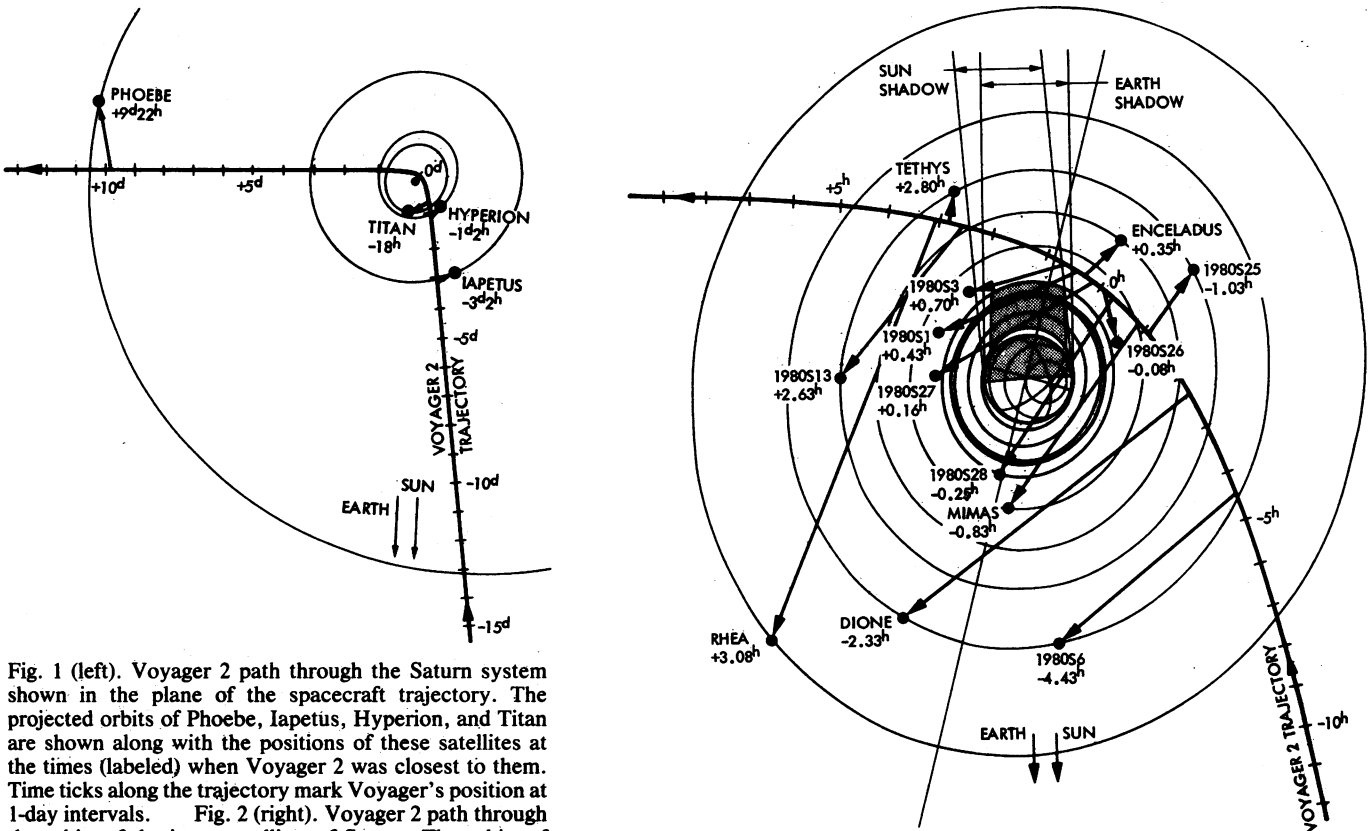


Fig. 1 (left). Voyager 2 path through the Saturn system shown in the plane of the spacecraft trajectory. The projected orbits of Phoebe, Iapetus, Hyperion, and Titan are shown along with the positions of these satellites at the times (labeled) when Voyager 2 was closest to them. Time ticks along the trajectory mark Voyager's position at 1-day intervals. Fig. 2 (right). Voyager 2 path through the orbits of the inner satellites of Saturn. The orbits of Mimas through Rhea are shown projected into the plane of the spacecraft trajectory. Positions of all of the satellites are shown at the times (labeled) when Voyager 2 was closest to them. The limits in the plane of the spacecraft trajectory of the sun and Earth "shadows" are shown. Time ticks mark Voyager's position at 1-hour intervals.

craft maneuvers resulted in a roll attitude offset of about 1°, which persisted until celestial references were reacquired. This attitude offset was too small to adversely affect radio science or wide-angle imaging observations, but infrared and narrow-angle imaging observations of the satellites were pointed just off the edge of their targets. Fortunately, most of the critical Voyager 2 observations had been completed before these anomalies occurred; lost were some close-approach observations of Enceladus and Tethys, some dark-side ring observations, and much of the southern hemisphere atmospheric high-resolution studies. Partial operation of the scan platform was restored about 2.8 days after closest approach, permitting lower-resolution ring and atmosphere studies to be pursued and providing the first views of Saturn's outermost satellite, Phoebe. Analysis of the anomaly continues, and there is reason to believe that the scan platform will remain operable for Voyager 2's Uranus encounter.

Although the trajectory at Saturn was dictated primarily by the desire to continue on to Uranus, the timing of the

encounter was chosen to provide close approaches to Enceladus and Tethys and closer observations of Hyperion, Iapetus, Phoebe, and several of the recently discovered satellites than were afforded by Voyager 1. Voyager 2's path through the satellite system of Saturn is illustrated in Figs. 1 and 2.

Voyager 2 encounter activities commenced on 5 June 1981, with the spacecraft 77 million kilometers (47 million miles) from Saturn. Closest approach, at a distance of 100,800 km (62,600 miles) above Saturn's cloud tops, occurred at 0324 UTC (coordinated universal time) on 26 August 1981. The encounter period extended until 25 September 1981, although observations by the four scan platform instruments ceased with the completion of the Phoebe observations on 5 September 1981. The remaining investigations continued through the end of the encounter period.

The design of the Voyager 2 science sequences was particularly responsive to the findings of Voyager 1. All known satellites of Saturn were targeted for observation by Voyager 2, with special emphasis on satellites or surface areas

not imaged by Voyager 1. The surprising ring detail seen by Voyager 1 led to a number of sequences for studying ring dynamics, especially in the vicinity of the F ring, the B ring spokes, and the eccentric rings. In light of its lack of visual detail due to its surface-obscuring atmospheric hazes, Titan observations were deemphasized, except for studies of the hazes themselves. Low-latitude, auroralike emissions discovered by Voyager 1 were studied in more detail with Voyager 2's ultraviolet spectrometer, and synoptic maps of the infrared emission of Saturn's atmosphere were moved closer to the planet to provide better latitude resolution. Imaging observations were designed for optimal measurement of zonal cloud velocities, extending those measurements to much higher latitudes than provided by Voyager 1. A number of unexpected details in Voyager 1 high time resolution plasma wave and planetary radio astronomy data led to a substantial increase in the amount of such data during the 24-hour period surrounding closest approach of Voyager 2, especially during and near the time of ring plane crossing (54 minutes after

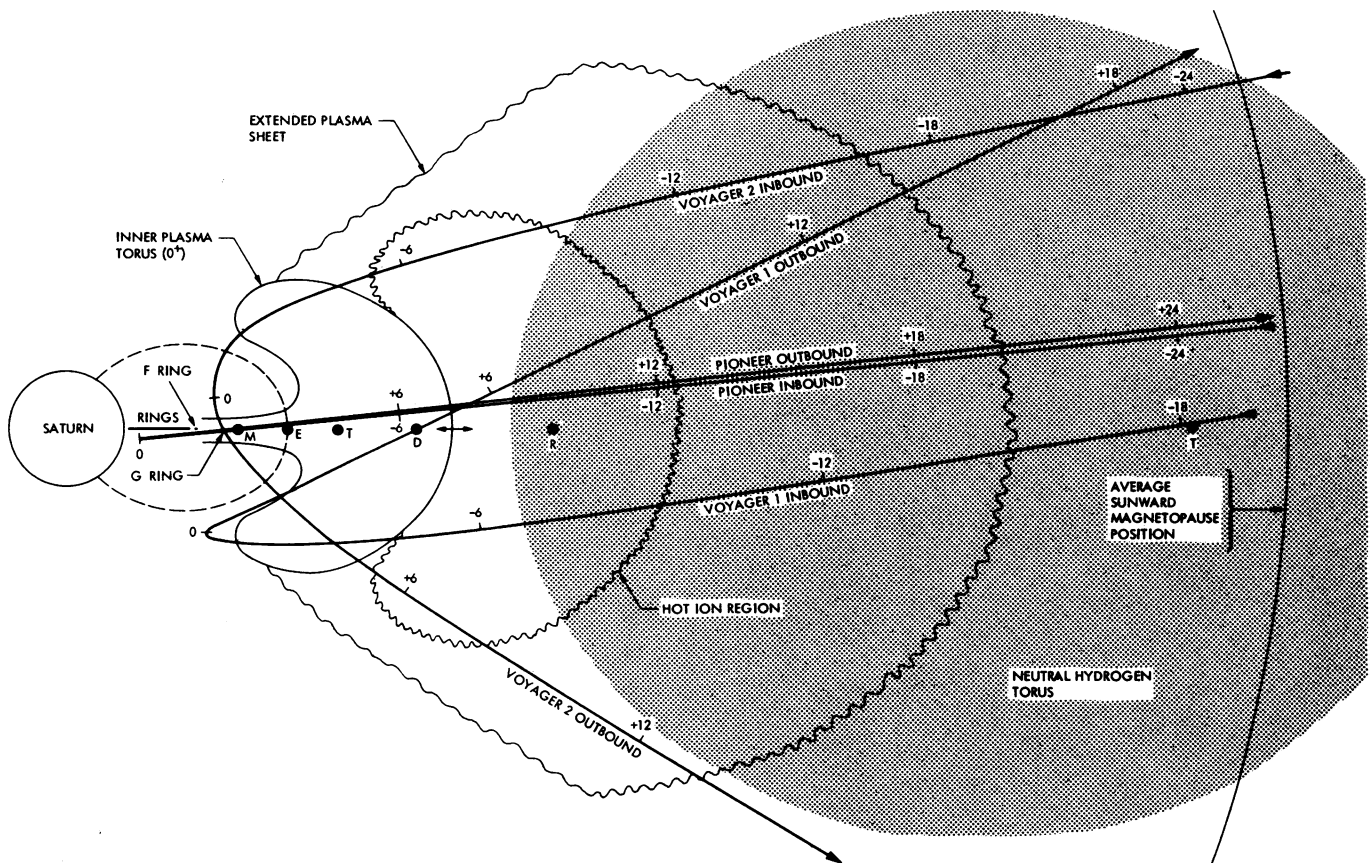


Fig. 3. Schematic cross section of Saturn's magnetosphere. Shown in meridional projection are the time-tagged (hours from Saturn closest approach) paths of Pioneer 11, Voyager 1, and Voyager 2. Ring plane (magnetic equator) crossings for Pioneer 11 occurred just outside (inbound) and inside (outbound) the G ring. Voyager 1 crossed the ring plane near the orbits of Titan (inbound) and Dione (outbound). Voyager 2's crossing occurred about 5000 km outside the center of the G ring. Shown schematically are cross sections of Enceladus' magnetic L shell, the inner plasma torus of ionized oxygen, the extended plasma sheet (including a hot ion region), the neutral hydrogen torus, and the average position of the sunward boundary of Saturn's magnetosphere.

closest approach to Saturn). Magnetospheric observation sequences were added to take advantage of the deeper penetration of the Saturn magnetic field by Voyager 2, especially near the Saturn equatorial plane, which very nearly coincides with the magnetic equator (and the plane of the rings). Figure 3 depicts in a meridional projection the paths of Pioneer 11 and the two Voyagers through the Saturn magnetosphere, showing the complementarity of the magnetospheric regions sampled by each of the three spacecraft.

Saturn's atmosphere. The Voyager 2 images of Saturn provided much new information on the dynamics of the atmosphere, both because the Voyager 1 experience permitted optimization of exposure times and filters and because the Voyager 2 vidicon was more sensitive. With the increase in detail, the Saturnian atmosphere appears to have a number of key similarities with that of Jupiter. A number of long-lived oval spots dynamically resembled the Jovian white ovals, which are anticyclonic wind systems. One such Saturnian oval was 7000 by 5000 km (4000 by 3000 miles) with 100 m sec^{-1} (200 mile per hour) circumferential winds. As on Jupiter, there are high-speed jet streams with directions alternating between eastward and westward with increasing latitude, except that the pattern occurs at higher latitudes on Saturn. There are also intermittent eruptions of convective clouds similar to the Jovian equatorial plumes. The largest longitudinal temperature variations occur at the same latitudes as these irregular convective clouds. Smaller convective clouds appear tilted in a manner which suggests that the jet streams are powered by small-scale eddies as in the Jovian atmosphere. The marked dominance of eastward jet streams on Saturn is an indication that the winds are not confined to the cloud layer but must extend at least 2000 km downward into the atmosphere. The winds may extend much deeper since the symmetry of the jet stream pattern in the northern and southern hemispheres is consistent with the concept that the wind pattern extends from north to south through the interior in the form of differentially rotating, coaxial cylinders. High-speed jet streams at high northern latitudes are also inferred from the temperature measurements.

Voyager 2's passage behind Saturn permitted the spacecraft radio beam to probe two more areas of the planet's atmosphere near 36.5°N and 31°S , complementing the near-polar and equatorial measurements made by Voyager 1.

These measurements indicate minimum temperatures of about 82 K near the 70-mbar level, increasing to $143 \pm 6 \text{ K}$ at the deepest level probed (1.2 bars), consistent with data from Voyager 1. At the 100-mbar level, infrared measurements revealed that north polar temperatures were about 10 K colder than mid-latitude temperatures at the same pressure level, presumably a seasonal effect.

Another similarity to Jupiter is the presence of ultraviolet-absorbing material in the upper atmosphere at latitudes above $\sim 65^\circ$. As on Jupiter, it is suggested that high-latitude auroral activity leads to the formation of complex hydrocarbon molecules, which are convected toward the equator. Direct observation of the ultraviolet emission from the aurora indicates that it occurs within 12° of the pole and is variable in intensity. The longitude and local time of maximum auroral activity is similar to that for the Saturnian kilometric radio emission, suggesting a direct connection. A similar ultraviolet emission from H_2 at lower latitudes appears to be unrelated to the precipitation of energetic particles that causes the aurora, since the low latitude emission depends on sunlight. The source of this emission is still a puzzle.

Rings. Voyager 2 returned significant information on the rings, both because it was possible to measure the amount of light from the star Delta Scorpii transmitted through the rings (the stellar occultation) and because it obtained much higher resolution images of the illuminated face of the rings. The stellar occultation measurements by the photopolarimeter provided a typical radial resolution of $\approx 300 \text{ m}$. It was found that even at this scale very few gaps exist in the rings. The edges of the rings at the gaps that do exist are so sharp, however, that the rings must be $\approx 200 \text{ m}$ thick at those locations.

Since there are so few gaps, most of the radial structure in the B ring must be due to variations in the optical thickness of the rings resulting from density waves, gravitational instabilities, or dynamical instabilities. Density waves are excited by the gravitational effects of the Saturnian satellites and propagate outward from the resonant orbits where the ring particles orbit Saturn in synchronism with the satellite. For example, at the 2:1 resonant point with satellite 1980S1, there is a series of outward propagating density waves with characteristics which indicate that in that region of the B ring there is $\sim 60 \text{ g}$ of material per square centimeter of ring area and that the relative velocities of the ring particles are $\approx 1 \text{ mm sec}^{-1}$.

The outer edge of the B ring is elliptical with a difference of $\approx 140 \text{ km}$ in the semimajor and semiminor axes, a somewhat larger difference than predicted by the 2:1 resonant interaction with Mimas. However, the axes of the ellipse rotate with the orbital motion of Mimas, as predicted. There are numerous radial variations with scales of 20 km in the outer B ring which are also noncircular, presumably the result of waves or instabilities. Radial features with scales of 500 km, however, appear to be circular.

In almost every case where clear gaps appear in the rings, eccentric ringlets are found. All seem to exhibit azimuthal brightness variations, due at times to variable radial extent of the rings and at other times to "kinks" or concentrations of ring particles or to nearly complete absence of ring material at various azimuthal positions. Two separate discontinuous ringlets were seen in the A ring gap near $2.21 \text{ Saturn radii } (R_S)$ from the center of Saturn ($1 R_S = 60,330 \text{ km} = 37,490 \text{ miles}$). At high resolution, at least one of these ringlets is multiply stranded.

Although the presence of gaps and eccentric ringlets suggests that there are imbedded moonlets that are responsible, a systematic search for small satellites in the ring gap at the inner edge of the Cassini division yielded negative results. The nondetection sets an upper limit to the diameter of any unseen moonlets of 5 to 9 km (3 to 6 miles), depending on the assumed surface reflectivity. Although no systematic searches were conducted in the other ring gaps, the limited regions that were imaged revealed no moonlets.

The multistranded narrow F ring received considerable attention in replanning the Voyager 2 observations. At 15-km (9-mile) resolution, the F ring was seen to consist of one bright strand and four fainter ones, each ~ 70 to 100 km across, which, at least in that segment of the ring, did not appear to be braided or intertwined. The photopolarimeter stellar occultation showed that even the brightest strand was subdivided into numerous narrower strands about 3 km wide, possibly as a result of larger particles in the ring. Clumps of material in the F ring were observed over 15 orbits. The clumps are quasi-uniformly distributed about the ring every $\sim 9000 \text{ km}$, a spacing that coincides with the relative motion of F ring particles and the shepherd satellites in one orbital period.

The "spokes" or clouds of micrometer-sized particles observed between $1.72 R_S$ and the outer edge of the B ring were also studied. Time-lapse sequences by Voyager 2 revealed that the spokes that are narrow and radial in alignment

(hence presumably more recently formed) very nearly corotate with Saturn's magnetic field. Broader, less radial spokes appear to be remnants from earlier epochs (perhaps as much as several orbits earlier) and follow Keplerian orbits. In some cases, "new" spokes may be reprinted over preexisting ones. Spoke formation is not limited to regions near the planetary shadow, although spokes are more readily seen at the ring ansa near which ring particles have most recently exited the shadow. Spokes are also seen at high phase angles in reflected Saturn light on the unilluminated face of the rings, suggesting that their formation may not be dependent on photoelectrically induced charging effects.

Voyager 2 provided higher resolution color images of the entire ring system than were previously available. These reveal color differences within each of the major rings in addition to the differences between rings noted in Voyager 1 images. The color differences may be due in part to differences in optical depth between various parts of the rings, but may also indicate small compositional differences that have been preserved over geologic time.

The general dimensions of the main rings are given in Table 1, based on Voyager 1 and Voyager 2 imaging, radio science, and ultraviolet observations. More precise numbers will eventually be available from Voyager 1 radio science and Voyager 2 photopolarimeter measurements. However, some of these features may not have constant radial distances from Saturn.

Improved images of the D, G, and E rings were also obtained by Voyager 2, providing better measurements of their positions, optical depths, and radial extents.

Satellites. Voyager 2 imaged all of Saturn's known satellites, which now number 17. There is an indication from charged particle shadowing effects that additional material, possibly another small satellite, exists in approximately the same orbit as Mimas [see also (6)]. New masses for Iapetus and Tethys were derived from Voyager trajectory measurements, leading in addition to a revised estimate of Mimas' mass. The resulting density estimates and other characteristics of the satellites are summarized in Table 2. It now appears that, with the exception of Titan, there may be a tendency toward decreasing density for the regular satellites with increasing radial distance from Saturn, as is the case for the Galilean satellites of Jupiter.

There is also a tendency for the

brighter satellites to be the most evolved, while the darker ones are more primitive and usually irregularly shaped. Thus the surfaces of the darker objects such as 1980S28 may be representative of the original mixture of rock and ice, while the brighter surfaces of evolved satellites such as Tethys and Enceladus may be the result of internal activity that melted the icy surfaces.

Phoebe is perhaps the most anomalous of the satellites. It orbits in a retrograde direction in a plane much nearer the ecliptic plane than Saturn's equatorial plane, leading to the suggestion that it is a captured asteroid. From Voyager 2 it is now known that Phoebe is roughly spherical with a 220-km diameter, spinning on its axis approximately once every 9 hours. Its surface is very dark (albedo = 0.06) and probably quite red, consistent with the properties of the class of asteroids believed to be very primitive and unmodified. If so, the images of Phoebe would be the first of such an asteroid.

Iapetus has long been known to have large albedo differences across its surface. Voyager 2 provided a view of this satellite that revealed a surface with the widest range of albedo values seen on any single body in the solar system: its dark material reflects only 5 percent of the sunlight, whereas the bright surface areas reflect 50 percent of the incident sunlight. The bulk of the dark material has a distribution that is precisely centered on the leading face of Iapetus in its orbital motion, supporting the conjecture that the dark material was swept up as it spiraled inward, presumably from Phoebe. The trailing face of Iapetus, however, has a number of craters with darkened floors, implying that the dark material originates in the interior of the satellite. It is possible that both processes occurred on Iapetus.

Hyperion appears to show no evidence for internal activity. Its irregular shape and the remaining evidence of heavy bombardment by meteoritic and asteroidal material indicate that it may have the oldest surface in the Saturn system. Its rather dark surface may also have been contaminated by the deposition of darker material.

Voyager 2 images of Tethys revealed an enormous impact structure, nearly one-third the diameter of Tethys itself and larger than the satellite Mimas. It appears to have formed when Tethys was relatively warm, since following the impact the satellite surface recovered almost to its original shape. Tethys' current surface temperature, however, is

only 86 ± 1 K. A gigantic fracture spans three-quarters of Tethys' circumference. If Tethys was fluid in its past, and its crust hardened before its interior, the freezing and consequent expansion of the interior would cause a surface spreading of approximately the dimensions seen for this feature, called Ithaca Chasma. However, such spreading would not be expected to be concentrated in a single, circumferential fracture.

By far the most active satellite surface yet seen in the Saturn system is that of Enceladus. At least five types of surface units have been identified, with the youngest, least cratered areas being less than a few hundred million years old. Indeed, it seems likely that the surface of Enceladus is still undergoing change. Other evidence for tectonic activity is provided by orthogonal patterns of rectilinear faults and ridged plains that have curvilinear valleys similar to those observed on Ganymede. It seems unlikely that radioactive nuclides could provide sufficient heating in such a small body to cause the changes noted. A more likely source of heating is tidal interaction with Dione, although current theoretical estimates seem to be too low, given the observed eccentricity of Enceladus' orbit. Because Enceladus is so reflective, its surface temperature is only 72 K.

Titan, which is a planet-sized satellite, was studied intensively by Voyager 1 and more remotely by Voyager 2, which concentrated on studies of Titan's photochemical haze layers. In the images, the main opaque haze layer peak occurs 183 ± 30 km above Titan's surface in the north and 50 km higher in the south, thought to be a seasonal difference. The absence of any measurable change in the haze albedo between Voyager 1 and Voyager 2 indicates a large seasonal lag in atmospheric changes, which therefore must be associated with the more massive deeper atmosphere. Although the mean radius of the particles in the haze layer is ~ 0.5 μm , polarization measurements require either that there be a range of particle sizes down to ~ 0.05 μm , or (perhaps more likely) that the particles be nonspherical. In the much thinner upper haze layer, which is 314 ± 30 km above Titan's surface, the mean radius of the particles is 0.3 μm .

Titan's atmosphere is also the source of a torus of neutral hydrogen atoms which surrounds Saturn between 8 and 25 R_S . The torus extends 7 to 8 R_S above and below the equatorial plane and has a mean density of 20 H atoms per cubic centimeter with a lifetime against ioniza-

tion of $\sim 10^8$ seconds, requiring a supply rate of 10^{27} H atoms per second from Titan.

Magnetosphere. The Voyager 2 flyby produced further puzzles about Saturn's internal magnetic field. The discovery of recurring radio emission by Voyager 1 suggested that the Saturnian magnetic field possessed a large-scale longitudinal asymmetry that resulted in radio emission every rotation of the planet. The Voyager 2 flyby, even though closer than that of Voyager 1 and at higher latitudes than Pioneer 11, found no evidence for any significant asymmetry of the magnetic field other than the $\sim 1^\circ$ tilt with respect to Saturn's rotation axis previ-

ously reported from Voyager 1 data. Also puzzling were observations of absorption of trapped particles by Mimas, Enceladus, and Tethys. Such absorption shadows, which extend to higher latitudes along the magnetic field lines threading the satellites, were not observed at the distances predicted by the magnetic field models.

The size of Saturn's magnetosphere is determined by external pressure from the solar wind. The pressure was high and the magnetosphere extended sunward only $\sim 19 R_S$ when Voyager 2 first entered it. Several hours later, however, the external pressure apparently dropped, followed by inflation of the

magnetosphere over an ~ 6 -hour period. Evidently the magnetosphere remained inflated for at least 3 days, since it was 70 percent larger at the time Voyager crossed the magnetospheric boundary outbound. During this time the Saturnian kilometric radio emission dropped below detectability, perhaps due to the reduction in the external pressure on the magnetosphere.

Since Voyager 2 had earlier detected the Jovian magnetotail extending at least three-fifths of the distance from Jupiter to Saturn, it is possible that the reduced pressure and absence of radio emission resulted from immersion of Saturn in the extended Jovian magnetotail or the asso-

Table 1. Saturn ring data.*

Feature	Distance (km)	Distance (R_S)	Comments
Equatorial radius	60,330	1.000	Near the 100-mbar level in Saturn's atmosphere
D ring inner edge	67,000	1.11	Onset of ringlet structure in images
C ring inner edge	74,400	1.233	Onset in radio data of signature of individual ringlets; C ring features seen in images down to $\sim 73,200$ km
B ring inner edge	91,900	1.524	Sharp increase in optical depth (radio plus ultraviolet)
B ring outer edge	117,400	1.946	Outer edge variable by at least 140 km; spokes between $1.72 R_S$ and outer edge of B ring = inner edge of Cassini division
A ring inner edge	121,900	2.021	Sharp increase in optical depth (radio plus ultraviolet); outer edge of Cassini division ambiguous in imaging data
A ring gap center	133,400	2.212	Encke or Keeler gap ~ 320 km wide
A ring outer edge	136,600	2.265	Sharp decrease in optical depth (radio plus ultraviolet)
F ring center	140,300	2.326	Eccentric ring; multiple strands; edges not well defined (radio plus ultraviolet)
G ring center	170,000	2.8	Optical depth $\sim 10^{-4}$ to 10^{-5}
E ring inner edge	180,000†	3†	Not well defined; maximum brightness near the orbit of Enceladus
E ring outer edge	480,000†	8†	Not well defined; maximum optical depth $\sim 10^{-6}$ to 10^{-7}

*Data presented here are preliminary. Some discrepancies exist between data sets. The R_S distances given to one decimal place are accurate to within about $0.05 R_S$; two-decimal precision implies an accuracy of about $0.02 R_S$; precision to three decimals implies an accuracy of about $0.003 R_S$; these numbers should eventually be improved to an accuracy of about 10 km = $0.0002 R_S$. †E ring dimensions are from Baum *et al.* (9). Voyager imaging shows little evidence of the E ring inside $3.5 R_S$ or outside $5 R_S$, presumably because of the low light levels involved.

Table 2. Saturn satellite data.

Name	Diameter (km)	Distance* (km)	Distance* (R_S)	Period* (hours)	Best imaging† resolution (km/lp)	Density (g/cm^3)	Albedo
1980S28	40 × 20	137,670	2.282	14.446	13(1)		0.4
1980S27	140 × 100 × 80	139,350	2.310	14.712	7(2)		0.6
1980S26	110 × 90 × 70	141,700	2.349	15.085	8(2)		0.6
1980S3	140 × 120 × 100	151,422	2.510	16.664	3(1)		0.4
1980S1	220 × 200 × 160	151,472	2.511	16.672	6(1)		0.4
Mimas	392 ± 6	185,540	3.075	22.618	2(1)	1.44 ± 0.18	0.7
Mimas companion	?	$\sim 186,000$	~ 3.1	?	-(2)		
Enceladus	500 ± 20	238,040	3.946	32.885	2(2)	1.16 ± 0.55	1.0
Tethys	1,060 ± 20	294,670	4.884	45.307	2(2)	1.21 ± 0.16	0.8
1980S13	34 × 28 × 26	294,670	4.884	45.307	12(2)		0.6
1980S25	34 × 22 × 22	294,670	4.884	45.307	5(2)		0.8
Dione	1,120 ± 10	377,420	6.256	65.686	3(1)	1.43 ± 0.06	0.5
1980S6	36 × 32 × 30	378,060	6.267	65.738	6(2)		0.5
Rhea	1,530 ± 10	527,100	8.737	108.42	1(1)	1.33 ± 0.09	0.6
Titan	5,150 ± 4	1,221,860	20.253	382.69	1(1)	1.88 ± 0.01	0.2
Hyperion	410 × 260 × 220	1,481,000	24.55	510.64	9(2)		0.3
Iapetus	1,460 ± 20	3,560,800	59.022	1,903.94	17(2)	1.16 ± 0.09	0.5, 0.05
Phoebe	220 ± 20	12,954,000	214.7	13,210.8	38(2)		0.06

*Note that most of the satellite orbit parameters published in the Voyager 1 Saturn issue (3) were in error by small amounts. Periods and distances given here for the five inner satellites and the Dione companion are from Synnott *et al.* (10); these periods and distances are for the time of Voyager 1 closest approach and are likely variable. 1980S6, for example, is likely to have the same orbital elements as Dione when averaged over a long time interval. Periods for the named satellites are from Newburn and Gulkis (7); distances for these satellites utilize updated values for Saturn's gravity harmonics (8). Periods and distances for Tethys' companions are assumed identical to those of Tethys. †Geometric resolution given in kilometers per imaging line pair; the number in parentheses indicates whether the best imaging was obtained by Voyager 1 or Voyager 2.

ciated wake. Before the encounter, when Jupiter and Saturn were nearly radially aligned from the sun and Saturn was therefore most likely to be affected by a Jovian magnetotail, there were a number of other periods during which the radio emission was undetectable. Although the observations are consistent with effects due to the Jovian magnetotail, there is currently no direct evidence that this was the situation.

Voyager 2 also acquired new information on the plasma and energetic particles in the magnetosphere. Combining these new results with the Voyager 1 and Pioneer 11 results, it is possible to identify several distinct regions, as shown in Fig. 3. Inside 6 or 7 R_S there is an inner torus of H^+ and O^+ ions, probably originating from the sputtering of water ice from the surfaces of Dione and Tethys and extending several R_S above and below the magnetic equator. Inside Enceladus' orbit, however, the torus is concentrated near the magnetic equator. At the outer edge of this inner torus, there are energetic ions with 30- to 50-keV temperatures. Strong plasma wave emissions also appear to be associated with the inner torus. Beyond the inner torus there is a very thick sheet of plasma extending out to $\sim 17 R_S$. The source of material for the outer plasma sheet is likely the ionosphere of Saturn, the atmosphere of Titan, and the neutral hydrogen torus that surrounds Saturn between ~ 8 and $\sim 25 R_S$. The observation of energetic H_2^+ and H_3^+ molecules strongly indicates an ionospheric source for some of the material.

Observations by Voyager 2 of Saturnian kilometric radio emission also provide evidence for a south polar source of emission. It appears to be much weaker than the radiation from the north polar region. Evidence for a frequency-dependent modulation of the radio emission by Dione was also obtained. Saturn electrostatic discharges were observed by Voyager 2 but at a rate approximately 10 percent that of Voyager 1 and with significantly different polarization characteristics, suggesting a dynamic source.

Summary. The Voyager 2 flyby completes the currently planned spacecraft observations of Saturn. The data acquired by the Pioneer and Voyager spacecraft have already revolutionized our knowledge and understanding of the Saturnian system. As the detailed analysis progresses over the next few years, our understanding will continue to grow and thoughtful consideration can be given to the nature of a future mission to Saturn.

In the meantime, the Pioneer and Voy-

ager spacecraft will extend the exploration of the interplanetary medium to ever-increasing distances from the sun. In 1990 Voyager 1 will be 40 AU from the sun, perhaps approaching the boundary of the heliosphere—the bubble that the solar wind is blowing in the surrounding interstellar medium. By that time, Voyager may already have detected the low-energy cosmic-ray particles from nearby sources which are excluded from the solar system by the outward flowing solar wind.

During this same time period, Voyager 2 will be encountering two more planets in the outer solar system. Voyager 2 is scheduled to begin observing Uranus in late 1985, with closest approach on 24 January 1986, and continuing on to an encounter with Neptune and its satellite Triton on 24 August 1989. Given that the spacecraft, which were designed for the 4-year mission to Saturn, will continue to operate well into the future, there will be the opportunity for still more major discoveries about the solar system.

E. C. STONE

California Institute of Technology,
Pasadena 91125

E. D. MINER

Jet Propulsion Laboratory,
California Institute of Technology,
Pasadena 91109

References and Notes

1. For an extensive discussion of the spacecraft, mission design criteria, trajectory selection, and the scientific investigations, see *Space Sci. Rev.* 21, 75 (1977); *ibid.*, p. 235. A detailed description of the design of the Voyager spacecraft was given by R. F. Draper, W. I. Purdy, and G. Cunningham, "The outer planet Mariner spacecraft," paper 75-1155, presented at the AIAA/AGU Conference on the Exploration of the Outer Planets, St. Louis, Mo., 1975.
2. Voyager 1 Jupiter results are outlined in *Science* 204, 945 (1979); *Nature (London)* 280, 725 (1979); *Geophys. Res. Lett.* 7, 1 (1980). Voyager 2 Jupiter results are outlined in *Science* 206, 925 (1979). Combined Voyager Jupiter results are contained in *J. Geophys. Res.* 86, 8123 (1981).
3. Voyager 1 Saturn results, *Science* 212, 159 (1981).
4. Voyager 1 Saturn results, *Nature (London)* 292, 675 (1981).
5. Pioneer 11 Saturn results, *Science* 207, 400 (1980); *J. Geophys. Res.* 85, 5651 (1980).
6. J. A. Simpson, T. S. Bastian, D. L. Chenette, R. B. McKibben, K. R. Pyle, *J. Geophys. Res.* 85, 5731 (1980); J. A. Van Allen, B. A. Randall, M. F. Thomsen, *ibid.*, p. 5709.
7. R. L. Newburn, Jr., and S. Gulikis, *Space Sci. Rev.* 3, 179 (1973).
8. Improved gravity coefficients for Saturn are given by G. W. Null, E. L. Lau, E. D. Biller, and J. D. Anderson [*Astron. J.* 86, 456 (1981)]. Null (private communication) used these coefficients to calculate improved values for the orbital distances of the satellites. These are the values given in Table 2.
9. W. A. Baum, *Icarus* 47, 84 (1981).
10. S. P. Synnott, C. F. Peters, B. A. Smith, L. A. Morabito, in (3), p. 191.
11. We wish to pay special tribute to the dedicated members of the Voyager Project team, without whom the scientific data reported in this issue could not have been collected. The Voyager Program is one of the programs of the Planetary Division of NASA's Office of Space Science. The Voyager Project is managed by the Jet Propulsion Laboratory of the California Institute of Technology under NASA contract NAS 7-100.

13 November 1981

A New Look at the Saturn System: The Voyager 2 Images

Abstract. *Voyager 2 photography has complemented that of Voyager 1 in revealing many additional characteristics of Saturn and its satellites and rings. Saturn's atmosphere contains persistent oval cloud features reminiscent of features on Jupiter. Smaller irregular features track out a pattern of zonal winds that is symmetric about Saturn's equator and appears to extend to great depth. Winds are predominantly eastward and reach 500 meters per second at the equator. Titan has several haze layers with significantly varying optical properties and a northern polar "collar" that is dark at short wavelengths. Several satellites have been photographed at substantially improved resolution. Enceladus' surface ranges from old, densely cratered terrain to relatively young, uncratered plains crossed by grooves and faults. Tethys has a crater 400 kilometers in diameter whose floor has domed to match Tethys' surface curvature and a deep trench that extends at least 270° around Tethys' circumference. Hyperion is cratered and irregular in shape. Iapetus' bright, trailing hemisphere includes several dark-floored craters, and Phoebe has a very low albedo and rotates in the direction opposite to that of its orbital revolution with a period of 9 hours. Within Saturn's rings, the "birth" of a spoke has been observed, and surprising azimuthal and time variability is found in the ringlet structure of the outer B ring. These observations lead to speculations about Saturn's internal structure and about the collisional and thermal history of the rings and satellites.*

The Voyager 1 encounter with the Saturn system in November 1980 extended the U.S. program of planetary exploration to nearly 1½ billion kilometers from the sun, adding more than a dozen new worlds as well as Saturn's extraordinary ring system to our catalog of solar system discovery. About 9

months later Voyager 2 followed on a different trajectory through the Saturn system, en route to more distant rendezvous with Uranus (in 1986) and Neptune (in 1989).

The Voyager 2 trajectory, although constrained by the requirements of a transfer to Uranus, was able to provide a

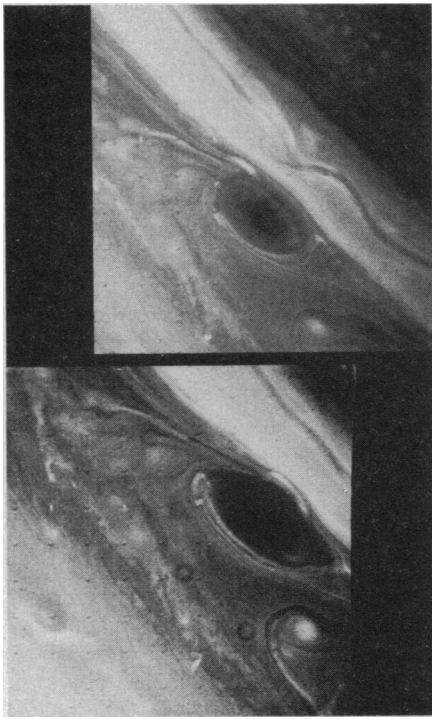


Fig. 1. Brown Spot 1 on two successive Saturn rotations, showing anticyclonic (clockwise in the northern hemisphere) rotation around its periphery. North is to the upper right. The spot's latitude is 42.5°N and it drifts to the east at 5 m sec^{-1} . The major diameter of the spot is 5000 km. A green filter was used in these narrow-angle images taken about 2 days before Voyager 2's encounter with Saturn.

between the encounters. Finally, the Voyager 2 vidicons are about 50 percent more sensitive than those on Voyager 1, enabling us to expose for maximum signal (approximately 200 levels of intensity above background) without a corresponding increase in image smear. This improved capability was particularly important for studying low-contrast cloud patterns in Saturn's atmosphere.

Saturn's atmosphere. With the wealth of detail visible in the Voyager 2 images, Saturn's cloud structures now look more like Jupiter's (1-3). Long-lived oval spots (Figs. 1 and 2), tilted features in east-west shear zones (Fig. 3), and a pattern of zonal (eastward and westward) velocity alternating in latitude (Fig. 4) are some of the major similarities. The greater wind speeds and latitudinal spacings of the zonal jets on Saturn are the major differences (4).

As on Jupiter, winds are measured with respect to a uniform rotation defined by radio observations of Saturn's magnetic field (5). The measurements reported here were made with the AMOS system of JPL's Image Processing Laboratory (6). In most cases, narrow-angle, green filter images (7) separated by about 10 hours were used to

measure displacements of features. For the northern hemisphere the resolution was usually about 50 km per picture element pair (for instance, Fig. 1). (As used here, image resolution is defined as twice the spacing between adjacent scan lines in an image.) For the southern hemisphere the resolution was usually 150 to 200 km (for instance, Fig. 2). Velocities derived from violet images, from images at 500-km resolution, from Voyager 1 images (8), and from measurements at other facilities (8) show no systematic differences from those of Fig. 4.

The zonal velocity profile of Fig. 4 enables us to address a fundamental question about Jupiter's and Saturn's atmospheres, namely, how far down do the wind patterns extend into the planets' fluid interiors? The following quantitative argument, based on dynamic meteorology (9), suggests that the atmosphere at the base of the clouds cannot rotate at the radio period. In other words, the winds observed at the cloud tops imply flow at great depths below cloud base.

The geostrophic relation (9) allows us to compute the height variations, measured in units of total gravitational and centrifugal potential Φ , of constant-pressure surfaces

$$\Phi(\lambda, p) - \Phi(0, p) = - \int_0^{\lambda} 2\Omega r u(\lambda', p) \sin \lambda' d\lambda'$$

Here λ is latitude, p is pressure, r is the planet's radius, and u is eastward zonal velocity in a reference frame rotating at the radio angular velocity Ω . Surfaces

look at the Saturn system in many respects complementary to that of Voyager 1. The viewing geometry for the rings was considerably improved, particularly for observations of the sunlit side at resolutions much greater than those in 1980. Higher resolution observations were permitted of the classical satellites missed by Voyager 1—Enceladus, Tethys, and Iapetus—as well as the smaller objects Hyperion, Phoebe, and recently discovered satellites. The ring observations were also helped by the increase in solar illumination angle, from 4° to 8° ,

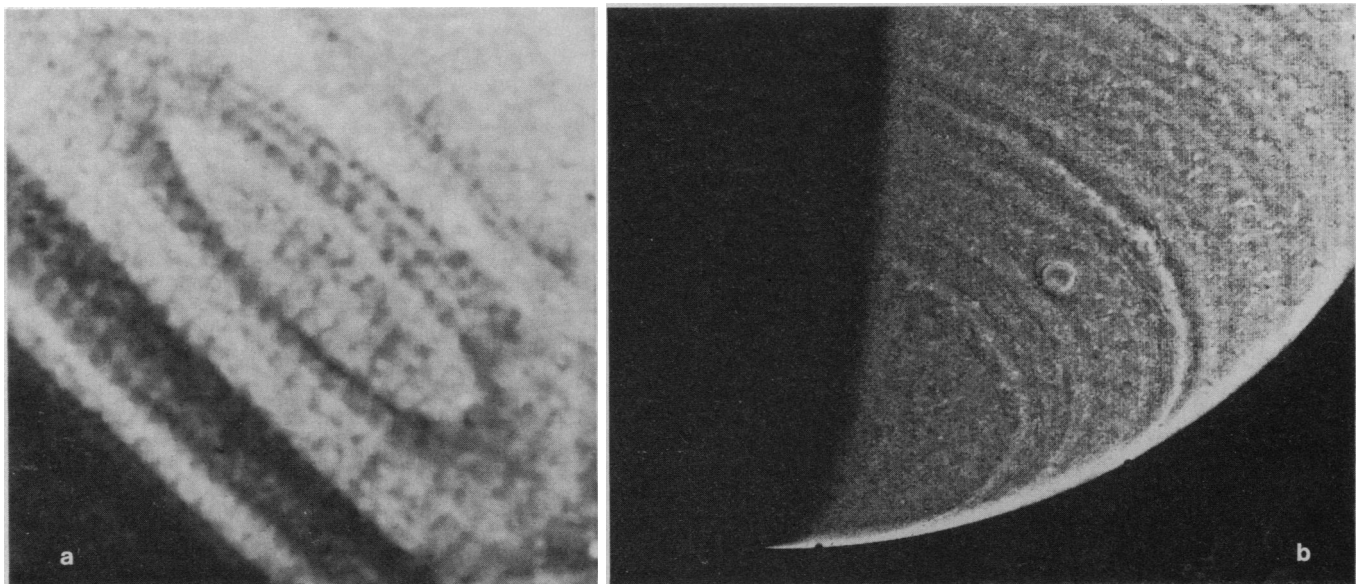


Fig. 2. Two views of Anne's Spot in Saturn's southern hemisphere at 55° latitude. The first view (a) was taken 2 days before encounter, the second view (b) 8 days after encounter. Both images were taken through a green filter. Anne's Spot has a red color resembling that of Jupiter's Great Red Spot. It is about 3000 km in diameter and moves to the east at 30 m sec^{-1} .

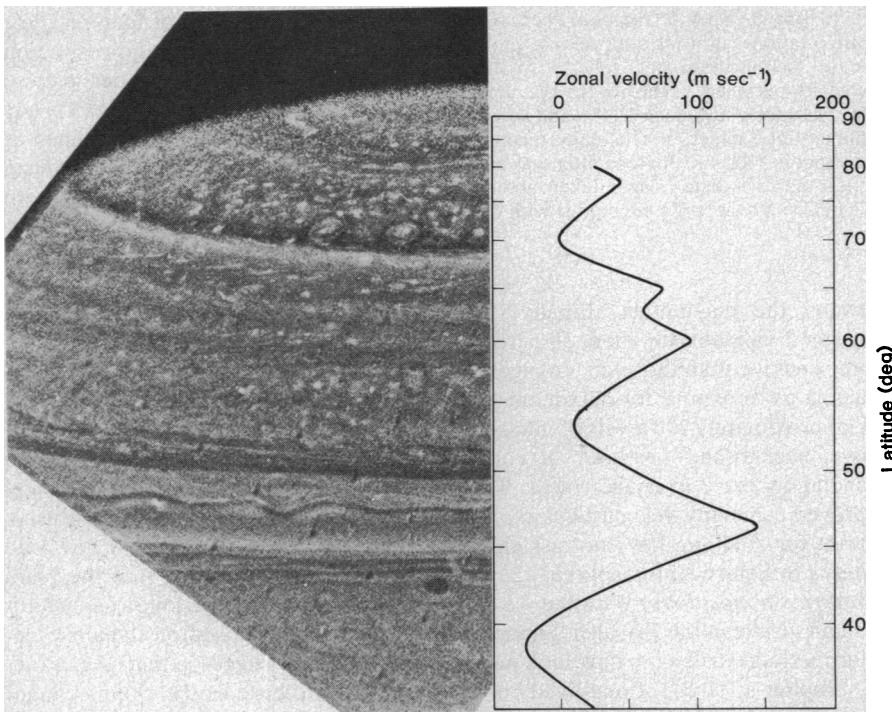


Fig. 3. High-contrast green image of Saturn's northern hemisphere with observed zonal (eastward) velocities at right. The north pole is in the field of view at the top of the image. The latitude scale matches the image along the center line. Note the correlation between the slope of the zonal velocity profile and the tilt of the cloud features.

$\Phi = \text{constant}$ are the level surfaces of the rotating planet. If the gravitational acceleration g were constant, the left side would be simply gz , where z is the height, relative to the surface $\Phi = \Phi(0,p) = \text{constant}$, of the surface for which $p = \text{constant}$. For a steady zonal

flow, the geostrophic relation is valid provided accelerations due to eddy stresses are less than the Coriolis acceleration. Since the eddy velocities are less than u and the eddy time constants are greater than Ω^{-1} , this condition is satisfied for both Jupiter and Saturn.

Figure 5 shows the integral above evaluated from zonal velocity data for Jupiter (2) and Saturn (Fig. 4). The data were assumed to represent a constant-pressure surface near cloud top. This assumption is justified below, where we show that zonal velocity variations with respect to pressure are likely to be small within the clouds. The integral has been normalized by a constant, $C_p \Delta T$, where C_p is the specific heat at constant pressure of a hydrogen-helium mixture ($1.3 \times 10^4 \text{ J kg}^{-1} \text{ K}^{-1}$) and ΔT is a characteristic temperature difference (200 K). This normalization factor is the thickness, measured in units of Φ , of an adiabatic layer spanning a temperature range ΔT . For both Jupiter and Saturn, it is roughly equal to the mean thickness of the cloud zone, which spans the range from about 300 to 100 K (10). In ordinary height units it is $C_p \Delta T / g$, which for Jupiter is about 110 km and for Saturn about 250 km.

According to Fig. 5, the normalized equator-to-pole drop in the height of a constant-pressure surface near the cloud top is about 0.4 for Saturn and about 0.05 for Jupiter. Saturn's greater drop is due to two factors: the generally higher wind speeds and the absence of substantial westward winds. If the cloud base were rotating at the radio rate such that $u = 0$, there would be no equator-to-pole drop in the height of a constant-pressure surface near the cloud base. The thickness of the layer bounded above and below by

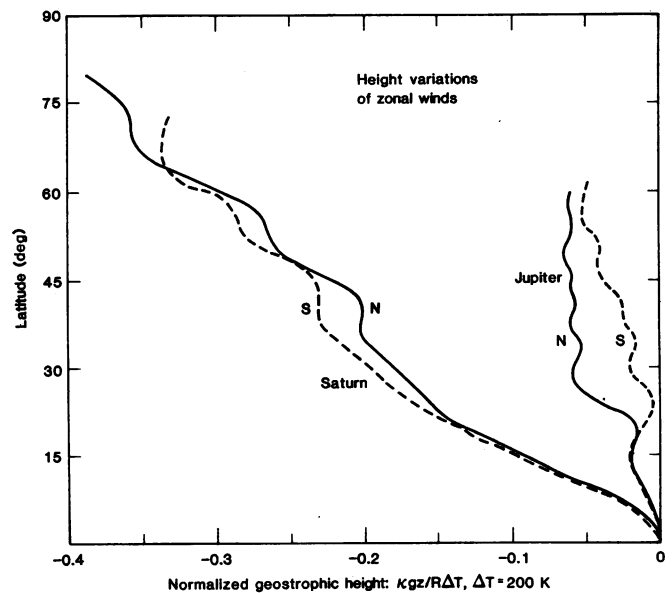
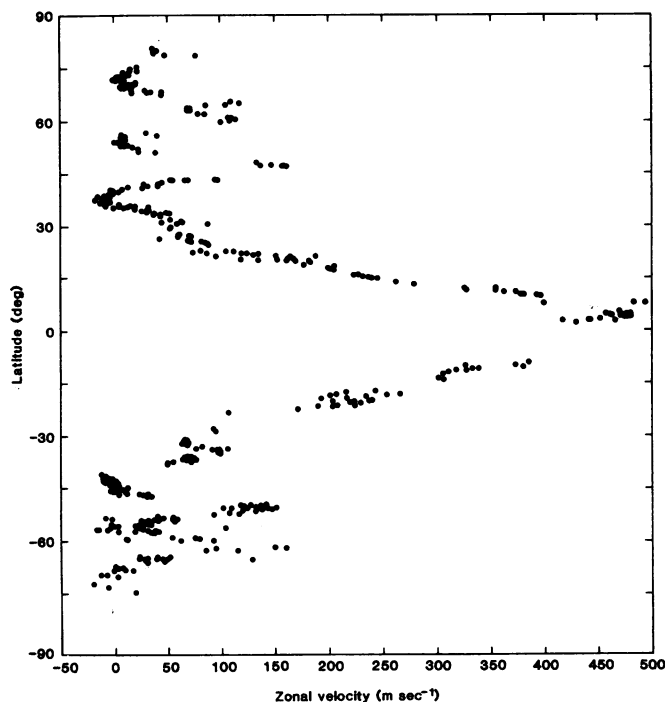


Fig. 4 (left). Zonal (eastward) winds in the reference frame of Saturn's magnetic field (5). Each point refers to a single cloud feature that has been followed for one Saturnian rotation. Points from 7° to 20°S are from Voyager 1 (8). Note the north-south symmetry of the profile, high eastward winds, and absence of strong westward winds. Fig.

5 (right). Height of a constant-pressure surface near cloud top computed from the data of Fig. 4 and (2). Height variations are expressed relative to the mean thickness of Saturn's and Jupiter's cloud zones. Note the large (40 percent) height decrease from Saturn's equator to poles. Such a decrease implies that the wind speed cannot be zero at the base of the clouds.

constant-pressure surfaces near cloud top and cloud base, respectively, would have to decrease by 40 percent from Saturn's equator to Saturn's pole, according to Fig. 5.

Such a large thickness change is inconsistent with Voyager infrared observations (11, 12) and estimates of Saturn's condensable gas abundances (10). The thickness of a layer between constant-pressure surfaces is proportional to the average of T/m for the layer, where the weighting is done with equal increments of $\log p$ (9). Here T is absolute temperature and m is mean molecular weight of the gas. A 40 percent thickness decrease implies a 40 percent drop in T/m from equator to pole. At levels around 500 mbar the temperature change is less than 1 or 2 K from Saturn's equator to the south pole, according to Voyager 1 infrared observations. At the same pressure levels the north and south poles have the same temperature, according to Voyager 2 infrared observations (11, 12). Since the 500-mbar temperature is about 100 K, these observations imply no more than a 1 or 2 percent thickness change. Of course, the Voyager infrared observations refer to regions above the cloud tops, but it seems unlikely that a 40 percent drop in T from equator to pole could occur within the clouds without causing a substantial drop in the region above.

Variations of m on the order of 1 or 2 percent also seem possible, but a 40 percent variation does not. For instance, if all the major condensable gases in an atmosphere of solar composition were to precipitate out, m would drop by 1.5 percent. Spectroscopic evidence (13) suggests that the solar composition model gives condensable gas abundances correct to a factor of 2. In sum, it appears that the thickness of the cloud zones on Jupiter and Saturn cannot vary by more than a few percent.

Notice that the 40 percent thickness change becomes a 4 percent change if we spread it out over a layer ten times deeper, that is, with $\Delta T = 2000$ K instead of 200 K. Since the maximum variation of T/m compatible with observation is about 4 percent, the minimum temperature range from cloud top to the level of no motion ($u = 0$) is about 2000 K. However, the pressure at the 2000 K level is greater than 10^4 bars, more than 1000 times the pressure at cloud base (10). Therefore, the mass involved in the zonal motions is at least 1000 times the mass of the cloud zone where sunlight is absorbed. This is a new conclusion, made possible by Voyager observations of Saturn's zonal velocity profile and

radio rotation period. The various thin-layer models of Jupiter's and Saturn's atmospheric circulations must be reexamined with this conclusion in mind (14, 15).

Imaging data provide no further information on the deep zonal flow beneath the clouds. It is possible that the fluid there has a uniform rotation rate close to the average rate of Saturn's visible atmosphere. Such a possibility is equivalent to adding a term, proportional to $\cos^2 \lambda$, to the curves in Fig. 5. The period that minimizes the height variation for Saturn in Fig. 5 is between 10 hours 31 minutes and 10 hours 32 minutes, about 8 minutes shorter than the radio period. If this were the rotation period of Saturn's interior from cloud base to metallic core, one would need a mechanism to maintain the internal differential rotation implied by the 10 hour 39.4 minute period of the magnetic field (5).

Alternatively, it is possible that the zonal velocity profile of Fig. 4 extends essentially unchanged into Saturn's interior. If Jupiter's and Saturn's fluid interiors were adiabatic (constant entropy per unit mass throughout the fluid), any steady zonal motion would take the form of differentially rotating, concentric cylinders whose common axis is the planetary axis of rotation. Such a coaxial

cylinder flow pattern, driven by deep-seated convection cells, was proposed before the Voyager encounters (15). Cylinders that do not intersect the metallic core would extend from the top of the adiabatic zone in the north to the top of the adiabatic zone in the south. The zonal velocity profiles would therefore be symmetric from north to south at the top of this zone, which might extend up to the base of the clouds. Departures from symmetry would have to arise as a result of nonadiabatic conditions (variations of T/m) within the cloud zone. According to Fig. 5, the difference between the normalized height of a constant-pressure surface near cloud top in the north and the north-south mean height is never more than 2 percent for both Jupiter and Saturn. As we have seen, thickness variations of this magnitude could arise within the clouds. Therefore, the departures from symmetry in the observed zonal velocity profiles are not inconsistent with the hypothesis of cylinders extending up to the cloud base.

According to the cylinder hypothesis (16), the density jump at the top of the metallic hydrogen core (17) decouples Saturn's northern and southern hemispheres poleward of about 65° latitude. For Jupiter, because the core is larger,

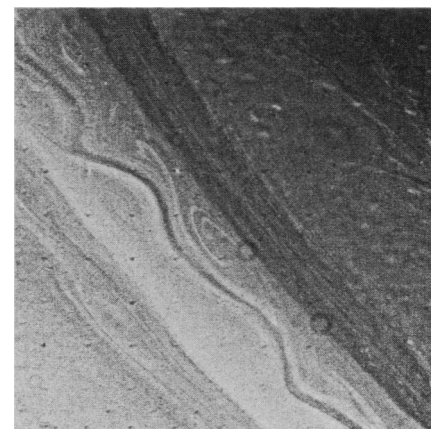
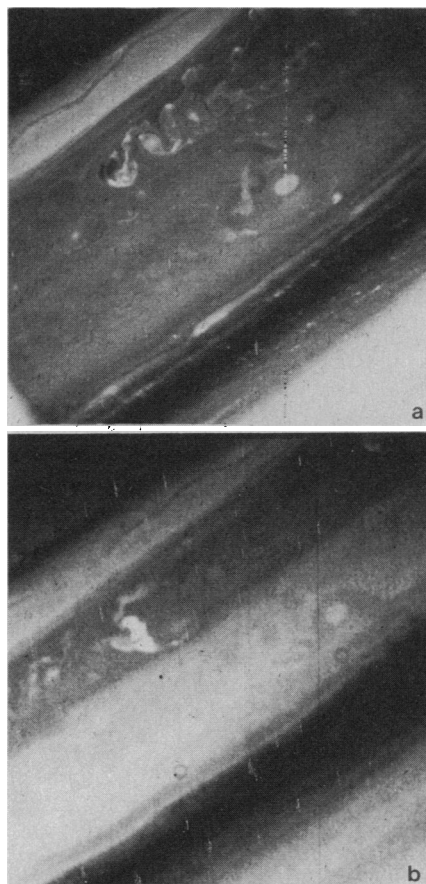


Fig. 6 (left). The UV Spot at 27°N observed by (a) Voyager 2 and (b) Voyager 1. North is to the upper left. A convective feature is visible to the north (at 39°N) of the UV Spot in both images. Fig. 7 (right). Details of the ribbon at 46°N . North is to the upper right. Note the laminar cyclones and anticyclones to north and south of the ribbon, respectively.

decoupling occurs at 40° to 45°. Again, the observed profiles are consistent with this hypothesis. In both hemispheres of both planets there are about three complete cycles of alternating eastward and westward winds from the equator to the latitudes at which decoupling occurs.

Any significant differential rotation in Saturn's interior implies substantial power dissipation unless the internal eddy viscosity is extremely small. Since the dissipated power cannot greatly exceed the internal heat release, a stringent upper bound on the viscosity is implied. Theories of convection in Jupiter's and Saturn's interiors must be reexamined with this upper bound in mind (16).

Two other similarities between Jupiter's and Saturn's zonal wind profiles are significant (2). First, there is evidence in Fig. 4 of a zonal velocity minimum at the

equator, with a local maximum at about 7°N latitude. Lack of data at 7°S latitude is due to interference by rings and ring shadow at the time of the Voyager encounters. Second, the curvature d^2u/dy^2 of the zonal velocity profile exceeds the planetary vorticity gradient β at most westward jet latitudes. Here y is northward coordinate $r\lambda$, and β is $2\Omega\cos\lambda/r$. Absolute values of d^2u/dy^2 at the eastward jet latitudes are several times β . The significance of these facts depends on one's model of how the winds are maintained and how deep they extend. For barotropic motion in a thin spherical shell (9) the fact that d^2u/dy^2 exceeds β means that the observed profiles are unstable to waves varying sinusoidally in the east-west direction.

We still do not have a direct measurement of the rate of poleward transport of

eastward momentum by eddies. For Jupiter we found that eddies were feeding momentum into the mean zonal jets (2), in accord with both thin-layer and thick-layer models (15, 16). For Saturn we have only the correlation shown in Fig. 3, indicating that cloud features (left) are tilted by the shear du/dy [computed from $u(y)$, right]. If these tilted cloud features were associated with tilted flow lines crossing latitude circles, the eddy momentum transport on Saturn would be into the jets as on Jupiter.

We next report on the stability and long-term behavior of the larger eddies (Figs. 1, 2, and 6). During Voyager 2 the locations of several such features were predicted 6 weeks in advance, so that commands to the scan platform could be prepared for narrow-angle imaging 2 days before closest approach to Saturn. The features were tracked in early Voyager 2 images beginning in June 1981. Using the AMOS system, constant drift rates with respect to longitude were established. Between mid-July, the deadline for scan platform pointing changes, and 23 August, when the images were taken, some features drifted by almost 360° of longitude (speeds of 100 m sec⁻¹) relative to other features. All features appeared at their predicted locations at the appropriate times, implying that the drift rates were constant to ± 5 m sec⁻¹.

As on Jupiter, the spots are of several kinds. First are the stable, symmetric ovals of various colors (white, brown, red), which acquired informal names (Big Bertha at 75°N, Brown Spots 1, 2, and 3 at 42°N, the UV Spot at 27°N, Anne's Spot at 55°S) and were successfully captured in high-resolution images (Figs. 1, 2, and 6). Most are located in anticyclonic shear zones (Fig. 4). Brown Spot 1 is 5000 by 3300 km along its long and short diameters (Fig. 1). Its anticyclonic circumferential flow reaches 30 m sec⁻¹, and its mean relative vorticity is 5×10^{-5} sec⁻¹, approximately one-fifth the local planetary vorticity. These numbers are similar to those for Jupiter's white ovals (3).

Features of the second kind, whose active behavior resembles Jupiter's equatorial plumes (18) and disturbed regions at higher latitudes (1), are the so-called convective features (Figs. 1 and 6) that flow westward with the jet at 39° latitude (Fig. 3). Individual cloud elements are bright, white, irregular, and short-lived. They seem to originate from several source regions in this latitude band, and resemble vortices shed by a solid vertical cylinder moving to the west. We do not know why such regions are found only at these latitudes, or why

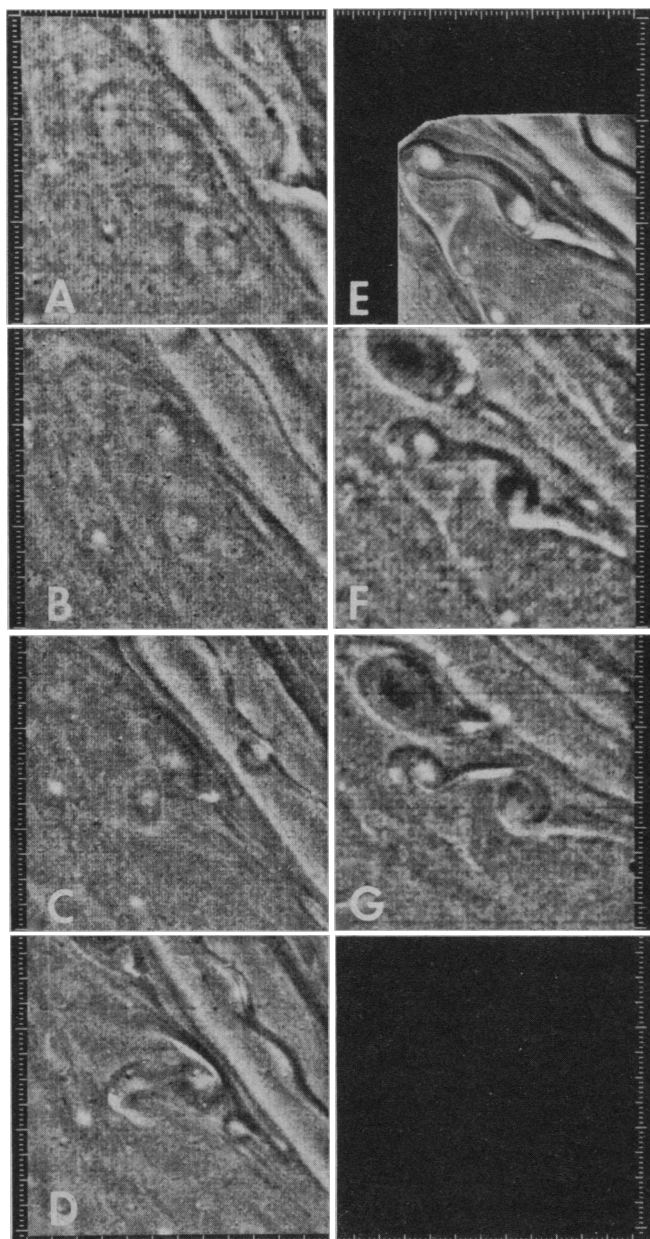


Fig. 8. Sequence of Voyager 2 images, spanning just over 7 days, recording the mutual interaction of two white spots as they approach larger Brown Spot 1. (A) Narrow-angle green image acquired on 17 August 1981, 8.3 million kilometers and 8.2 days prior to closest Saturn approach. Frame (B) was taken three Saturnian rotations later, with images (C) through (G) following at additional intervals of four, two, five, one, and one rotations, respectively. Frames (F) and (G) are long wavelength, wide-angle images, since they were taken too close to Saturn (1.8 million and 1.3 million kilometers, respectively) for the narrow-angle field of view to contain both white spots. All seven images were digitally filtered to exaggerate the contrast of small-scale features and normalized to a uniform scale. The width of each panel is approximately 16,000 km.

the convective activity occurs only in these source regions.

A third kind of feature, perhaps unique to Saturn, is the ribbon at 46° latitude (visible in Figs. 1, 3, 6, and 7). This dark wavy line moves with the peak eastward winds at that latitude (Fig. 3). Each crest or trough covers about 5000 km in the east-west direction. To the north of the ribbon, nestled in the troughs, are cyclonic vortices whose filaments (appearing laminar at 50-km resolution) spiral toward the center as one traces them counterclockwise (Fig. 7). To the south, nestled under the crests, are anticyclonic vortices that spiral inward as one traces them clockwise. Persistent laminar filaments of the type seen here are unknown on the earth.

A complex interaction of two westward-moving white spots ($u = -15$ and -20 m sec^{-1}) with Brown Spot 1 (BS1; $u = 5 \text{ m sec}^{-1}$) was observed during the last 8 days before encounter (E - 8 days to E - 1 day). At the start of this period the two white spots were at approximately the same latitude and about 10,000 and 15,000 km east of BS1, respectively (Fig. 8). All three spots have

anticyclonic (clockwise in the northern hemisphere) circulation, judging from the motion and morphologies of cloud features at their peripheries. This circulation is in the same sense as the wind shear in the surrounding flow.

At E - 8 days the white spot farthest east (WS1) appears to be slightly south of WS2; thus, if they follow the mean flow, they should move closer together as WS2 overtakes WS1. However, instead of colliding, WS1 moves farther south and goes around WS2. This "orbiting" action is consistent with each spot being influenced by the extended anticyclonic circulation of the other. This is in contrast to noninteracting solitary waves, which can pass through each other (19), and to the interactions occasionally seen on Jupiter in which two anticyclonic spots merge into one (1, 20). By E - 4 days WS2 is past WS1. Some merging does take place, for at this time they form a "double comma" structure with a wide dark band between them. There appears to be a connected circulation between the two spots. The dark band stretches out considerably during the next few days as WS2 continues to

move eastward relative to WS1. By E - 2 days the band is nearly 5000 km long. During the next two Saturn rotations the dark band becomes much narrower, as BS1 approaches within a few thousand kilometers of the two white spots. At E - 1 day it appears that the band between the two smaller spots is on the verge of disappearing. The nature of subsequent interactions between these three spots is unknown.

Examples of changes in the appearance of Saturn's northern hemisphere between the Voyager 1 and Voyager 2 encounters are shown in Figs. 6, 9, and 10. During Voyager 1 at visual wavelengths there was a broad (about 8° in latitude) dark band centered at 19°N (A in Fig. 10). During Voyager 2, this band was considerably narrower at long wavelengths (green) but unchanged in other colors, including ultraviolet, wherein it is the brightest region in Saturn's northern hemisphere. Immediately to the north (23°N), a narrow boundary region (B in Fig. 10) was, in November 1980, intermediate in brightness between adjacent bright and dark bands. This configuration persisted in August 1981 for ultravi-

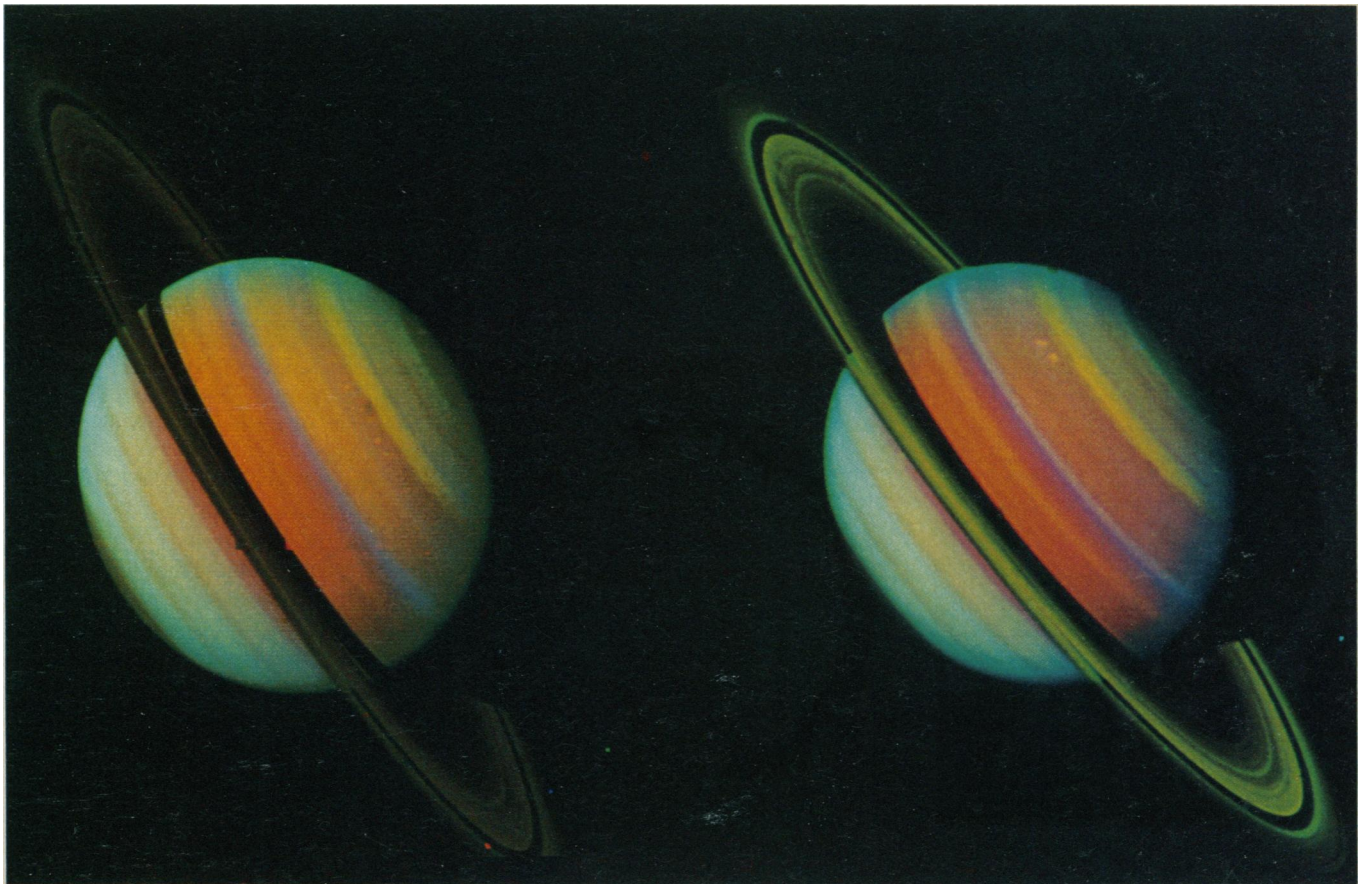


Fig. 9. False color images from Voyager 1 (left, 18 October 1980, range 34 million kilometers) and Voyager 2 (right, 12 July 1981, range 43 million kilometers), illustrating some of the changes that have occurred in the northern hemisphere. These versions were produced by deriving the blue, green, and red intensities from Voyager images taken through the ultraviolet, violet, and green filters, respectively. Changes seen in the Voyager 2 image include the development of a thin, whitish band at 23°N (due to brightening in the violet image) and the merging of light and dark orange bands into a single dark belt just to the north of the whitish zone.

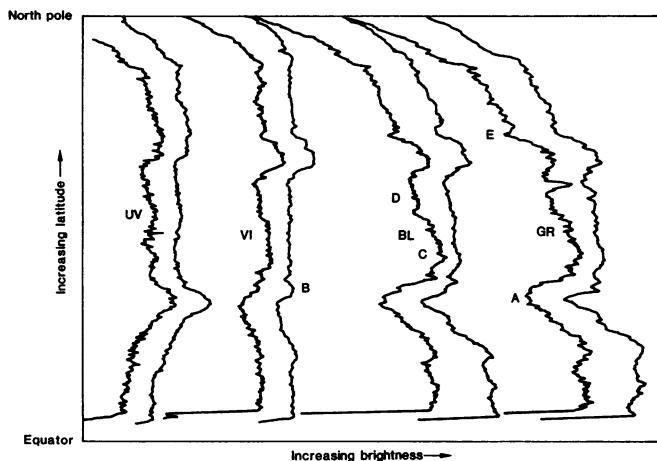


Fig. 10. Meridional brightness scans through both Voyager 1 and Voyager 2 images taken in each of four colors (*UV*, ultraviolet; *VI*, violet; *BL*, blue; and *GR*, green). For each color the left scan is from Voyager 1 data, while the right scan presents the Voyager 2 appearance. Letters *A* to *E* denote specific regions of change described in the text. Since the two spacecraft approached from slightly different

Saturncentric latitudes, there is not exact latitude correlation between the Voyager 1 and Voyager 2 scans. Also apparent is the greater noise content of the Voyager 1 images, caused by the lower exposure levels used during the encounter. [Color comparisons were prepared by E. P. Korsmo, JPL Image Processing Laboratory]

olet, blue, and green wavelengths, but had changed substantially in violet, wherein the boundary had become a thin bright zone. Farther north Voyager 1 observed a bright zone (23° to 36°N) and a dark belt (36° to 42°N)—*C* and *D*, respectively, in Fig. 10. By August 1981 the zone had darkened so that its albedo was equal to that of the belt. Yet farther north (50°N) Voyager 1 observed a thin band that was dark at visual wavelengths (*E* in Fig. 10). Voyager 2 found this belt to have become a pair of belts in blue and green, while remaining singular in violet. During both encounters, this feature was conspicuous in green to the limb of Saturn, suggesting that it was not overlain by a significant obscuring haze.

The Voyager encounters were separated by only 9.3 months (less than 0.03 Saturn year), so seasonal conditions were equivalent. Ground-based observations (21) demonstrate long-term seasonal variations, with the summer hemisphere appearing brightest at short wavelengths and the winter hemisphere brightest in green and red, a trend with which these short-term changes show no obvious correlation. Further, despite seasonal hemispheric differences, the velocity profiles (Fig. 4) are remarkably similar in the two hemispheres, suggesting again that zonal velocity is a deep-seated property. With Jupiter, which is virtually without seasons (its obliquity is only 3°), there is abundant variability in

the planet's banded appearance (1) but substantial long-term stability of the zonal velocities (2, 22). Saturn's ground-based record is less complete, but it also appears to exhibit short-term, nonseasonal variability in its banded appearance and long-term stability in its zonal wind velocity profile.

Titan. Titan is the only satellite in the solar system known to have a substantial atmosphere. Observations during the close flyby of Titan by Voyager 1 established that the atmospheric pressure is 1.6 bars and nitrogen is the dominant gaseous species (23). The next most abundant gases are methane (about 6 percent), molecular hydrogen (0.2 percent), and possibly argon (12 percent) (24). In addition, a number of lower order hydrocarbons such as C_2H_2 , C_2H_6 , and C_3H_8 and nitriles such as HCN have been detected at parts per million (11, 25, 26). Presumably these trace constituents as well as H_2 are produced from N_2 and CH_4 through a series of chemical steps initiated by solar ultraviolet radiation and the energetic particles of Saturn's magnetosphere (27). Further chemical reactions permitted by escape of hydrogen are thought to produce complex organic compounds that condense to form tiny "smog" particles or aerosols (28).

Voyager 1 photographs of Titan failed to show surface details, a result attributed to the ubiquitous aerosols with an optical depth of at least 5 at visual wavelengths (4). The presence of an optically thick particulate layer is further supported by the fact that the radius of Titan in the Voyager images is more than 200 km larger than the radius of the surface (23). In addition to smog particles, cloud particles composed of methane ice may be present in the lower 50 km of the atmosphere (23). The optical depth at the surface is nevertheless low at 20 μm wavelength (24).

Voyager 2 images of Titan were designed to provide observations at a more complete set of phase angles and full-disk coverage at high phase angles to aid analysis of the aerosols' physical characteristics and possibly see discrete atmospheric features that could be tracked for wind speed determination. Unfortunately, no unambiguous discrete features are present on any of the pictures studied to date, even with extreme contrast enhancement. However, as illustrated in Figs. 11, 12, and 13, Titan is not entirely bland. An upper haze layer is present above the main haze (Figs. 11 and 12), a hemispheric asymmetry of brightness is found (Fig. 13), and a dark band is present in the north polar region (Fig. 13).

Figure 11 illustrates the relation be-

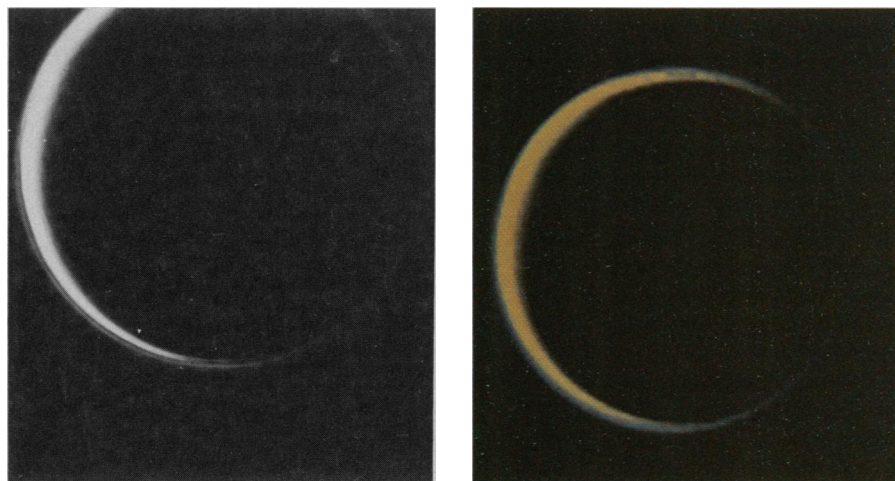


Fig. 11 (left). Photograph of Titan obtained with the clear filter of the narrow-angle camera at a phase angle of 155°. A distinct upper haze layer is present over much of the circumference of the disk, except in the north polar region. The subspacecraft latitude is 12.4°N. Fig. 12 (right). Color composite of Titan constructed from violet and green filtered pictures obtained with the wide-angle camera at almost the same time as the narrow-angle picture of Fig. 11. Colors have been exaggerated. Note the occurrence of blue light around the entire circumference of the limb.

tween the upper haze layer and the main haze layer as a function of latitude. At high northern latitudes, the two layers tend to blend together, owing to an increase in the altitude of the main haze layer and a decrease in the altitude of the upper haze. At northern mid-latitudes and equatorial and southern latitudes, the altitudes at which the peak brightness is reached for the two layers are separated by about 100 km, although, as the photometric profiles in Fig. 14 illustrate, the two layers merge. At the most southerly latitudes seen in Fig. 11, at least one additional layer appears to be present, due chiefly to a bifurcation of the main haze layer.

We obtained good estimates of the altitudes of the upper and main haze layers from analysis of Fig. 11. First, the picture was geometrically rectified. Second, photometric profiles, such as that in Fig. 14, were obtained along the circumference of the limb, including the faintly visible night side. From these profiles, it was possible to determine key positions in the haze structure, such as the location of peak brightness in the upper haze

layer (point A), the inflection point along the rise in brightness for the main haze layer (point B), and the peak brightness of the main haze layer (point C). Finally, a least-squares fit was performed to find the radius and center of the circle that best fit the circumferential positions of the upper haze and the altitude separation of the three features were found at various locations.

We find that the peak brightness of the upper haze layer is 2884 ± 20 km from the center of Titan. Using 2575 ± 2 km (29) for the radius of Titan's surface, we infer that this peak is at an altitude of 309 ± 22 km. A somewhat smaller value, 2825 km, was obtained from a less rigorous analysis of a poorer quality picture from Voyager 1. The corresponding altitudes for the inflection and peak of the main haze layer are 232 ± 22 and 178 ± 22 km, respectively, at northern mid-latitudes and 253 ± 22 and 229 ± 22 km at southern mid-latitudes (30). These results confirm the conclusion that almost all the light reflected to space by Titan is scattered from an optically thick layer of particles. Furthermore, since the

top of this layer is located far above the altitude at which any hypothetical methane cloud is expected to exist, the smog particles are the major and probably dominant scatterers of incident sunlight. Previous estimates for the optical radius of Titan— 2860 ± 20 km from very low resolution Pioneer 11 images (31), and 2900 ± 200 km from an earth-based observation of a stellar occultation (32)—are consistent with the Voyager 2 values.

As shown in Figs. 11 and 12, the atmosphere is bright along the entire circumference of the satellite at high phase angles. Such an extension of the "horns" of the illuminated crescent is the result of scattering of sunlight by aerosols from the sunlit side of the terminator to the night side, where other aerosols reflect the light back to space. This complete extension of the crescent provides additional evidence that much of the light reflected by Titan originates from the atmosphere and not the surface. The bluer color of the night side crescent is due in part to narrowing of the diffraction peak of the aerosols toward shorter wavelengths, which leads to a larger

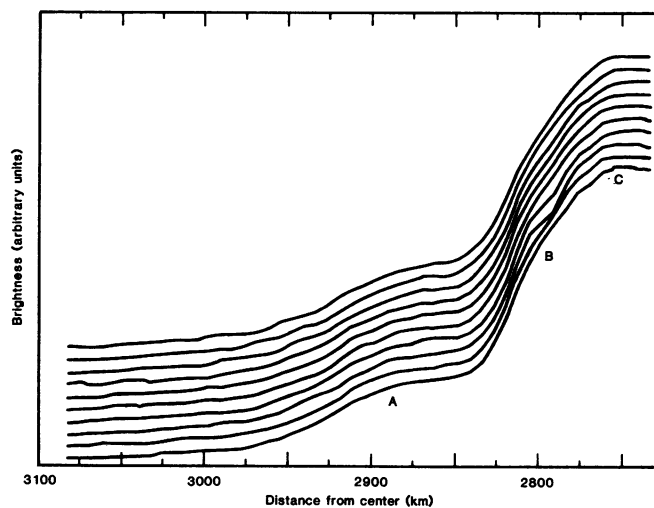
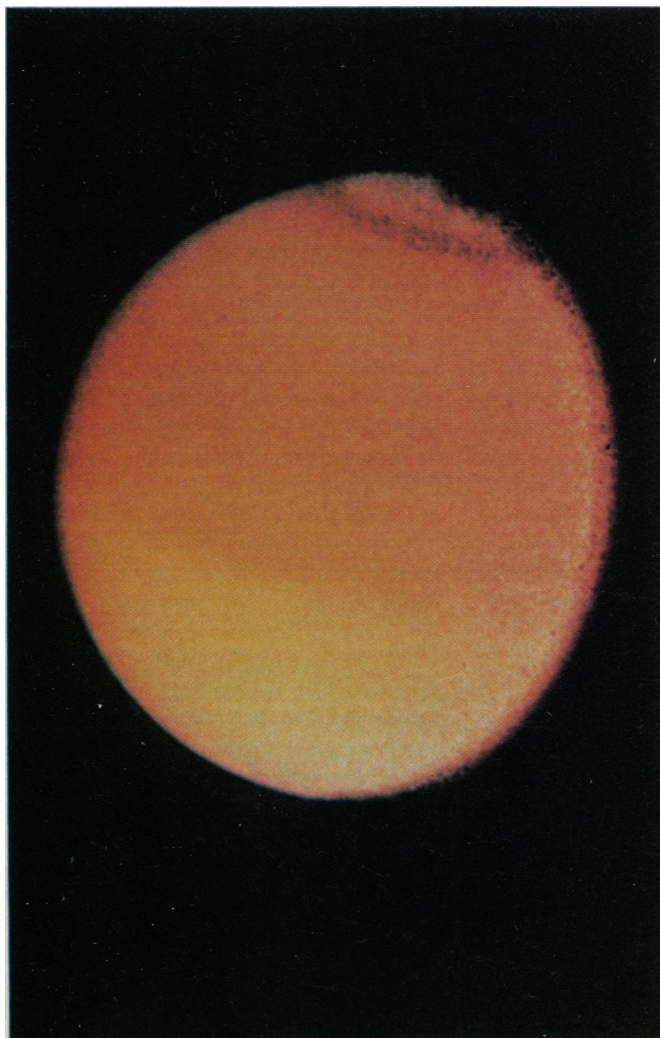


Fig. 13 (left). Color composite of Titan constructed from blue, green, and violet frames at a phase angle of 35° . As explained in the text, a correction for limb darkening was made in deriving this image. The northern hemisphere (top) is somewhat darker and redder than the southern hemisphere. Also, a dark ring situated at about 70°N is present in the northern polar region. [Processing by J. U. Reimer, JPL Image Processing Laboratory] Fig. 14 (right). Line scans of the brightness of Titan at adjacent locations perpendicular to its northern mid-latitude limb. These were derived from the high-phase angle picture of Fig. 11. The vertical scale is proportional to brightness in arbitrary units, with successive scans being vertically displaced from one another. Brightness reaches a value of zero on the left side. Peak brightness occurs within the main haze layer, while the shoulder at higher altitudes is the region of the upper haze level.

fraction of sunlight being scattered into the night side at short wavelengths.

As can be seen in Fig. 14, the upper haze layer extends almost 100 km above its peak brightness location. We searched for fainter higher altitude hazes by increasing the exposure time of a number of images in various colors up to a factor of 8 above the nominal exposure times. There is no evidence of higher altitude hazes on any of these pictures. These results set an upper bound of about 10^{-4} on the vertical optical depth of any such haze if it is present over an altitude range of 50 km. A somewhat lower value for the upper bound applies if the width of the layer is smaller.

As shown in Fig. 13, the northern hemisphere of Titan is somewhat darker and redder than the southern hemisphere, a phenomenon first observed on Voyager 1 images (4). Figure 13 was generated by removing approximately the dependence of the observed brightness on the illumination and viewing geometry and thus deriving "normal" albedos, that is, ones that would be observed for normal incidence and reflection. We approximated the limb darkening function by a Minnaert law (33), whose exponent was based on a limb darkening analysis of Voyager 1 photographs (33, 34).

Figure 15 shows the dependence of Titan's relative normal albedo on latitude for the 35° phase angle, blue-filtered picture used in constructing Fig. 13. The scale for these albedos was adjusted so that they have a value of 1 at 30° S. The relative normal albedos were obtained from a meridional scan at a longitude midway between the subspacecraft and subsolar points. The latitudinal variation of relative normal albedo is characterized by an approximately constant high value at southern mid-latitudes, a smoothly varying transition zone at equatorial latitudes, an approximately constant value at northern mid-latitudes that is about 25 percent smaller than that at southern mid-latitudes, and a dark polar cap area.

The solid line in Fig. 15 shows the same information obtained from a Voyager 1 blue-filtered picture of Titan at a phase angle of 30° . The relative normal albedo curves derived from Voyager 1 and Voyager 2 images at comparable phase angles agree remarkably well with one another. The only hint of a disagreement occurs at high southern latitudes, where the closeness of the Voyager 2 points to the limb and hence the increased inaccuracy in the limb darkening correction makes this apparent differ-

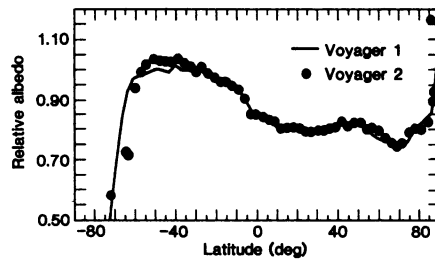


Fig. 15. Comparison of relative normal albedos of Titan derived from Voyager 1 and Voyager 2 images obtained at low phase angles. The hemispheric brightness asymmetry is virtually the same for these images taken 9 months apart. See text for details.

ence questionable. Below, we use this comparison between Voyager 1 and Voyager 2 albedos to constrain a model of the hemispheric asymmetry.

Smith *et al.* (4) suggested that Titan's north-south brightness asymmetry was a phase-shifted response to seasonal variations in solar heating of Titan's atmosphere (35). Since Titan was close to equinox at the time of the Voyager 1 observations, with the northern hemisphere just emerging from the winter season, a significant phase shift is required. Further, comparisons with ground-based observations of secular variations in Titan's disk-integrated brightness indicated that a large phase shift would be required if the north-south asymmetry was the principal source of secular brightness changes. Sromovsky *et al.* (34) used low-resolution images of Titan obtained from Pioneer 11, earth-based photometry (36), and the phase angle dependence of the north-south contrast on Voyager 1 images to assess the ability of this seasonal model to explain the observed secular brightness changes (37). They concluded that more than half of the secular variation was due to seasonal changes in hemispheric brightness and that there was probably also a significant contribution from 11-year modulations in the solar ultraviolet output, as suggested by Pollack *et al.* (38).

The two observational values that most directly constrain the seasonal model of contrast are the ratio of normal albedos for the mid-latitudes of the hemispheres and the position of the equatorial transition zone. If the brightness contrast varies seasonally with a phase lag of 83° (34), then the normal albedo ratio should decrease very slightly, from about 1.25 to 1.235. A greater decrease would imply a smaller phase lag. The comparison of the Voyager 1 and Voyager 2 albedo observations shown in Fig.

15 indicates that there is no obvious decrease in the albedo ratio over the 9-month interval between the two flybys. This is consistent with the large phase shift suggested by comparisons of Voyager 1 and Pioneer 11 data (34). Such a large phase shift implies that the contrast-producing mechanism involves the deeper, more massive regions of Titan's atmosphere.

The position of the transition zone is extremely important for assessing the relative contributions of the seasonal and solar cycle mechanisms for generating secular changes in Titan's disk-integrated brightness. If the zone remained fixed, the seasonal mechanism can account for 50 to 70 percent of the observed secular brightness variation, with the solar cycle mechanism presumably accounting for the remainder. If the zone moved in the opposite direction to the subsolar point, as vaguely suggested by comparison with Pioneer 11 data, the seasonal mechanism could account for all of the secular variation. The apparent movement of the zone suggested by the latter comparison indicates that the transition zone should be shifted 5° farther south at the time of the Voyager 2 observations. No such shift is apparent in Fig. 15, suggesting that the secular variation in Titan's brightness is caused by a combination of the seasonal and solar cycle mechanisms.

Several physical properties of the aerosols can be derived from analyses of Titan's brightness on selected images. These include the aerosols' cross-section-weighted mean particle radius, \bar{r} , and their optical depth at visible wavelengths, τ . Good estimates of \bar{r} can be obtained from simulations of the peak brightness of Titan at high phase angles, as much of the observed light is due to sunlight scattered at small deflection angles; therefore the observed brightness is strongly influenced by the diffraction component of the aerosols' angular scattering function (39). We simulated such brightness values on pictures obtained with the clear filter (effective wavelength, $0.5 \mu\text{m}$) of the narrow-angle camera at phase angles 140° and 155° . The theoretical calculations were performed by using a Mie scattering code (one in which the scatterers are dielectric spheres) to define the single-scattering properties of the model aerosols and a doubling code to solve the multiple-scattering problem (40). The main haze layer was assumed to be optically thick and the upper haze layer to be optically thin (4). The real part of the index of refraction was set equal to 1.6, as inferred from

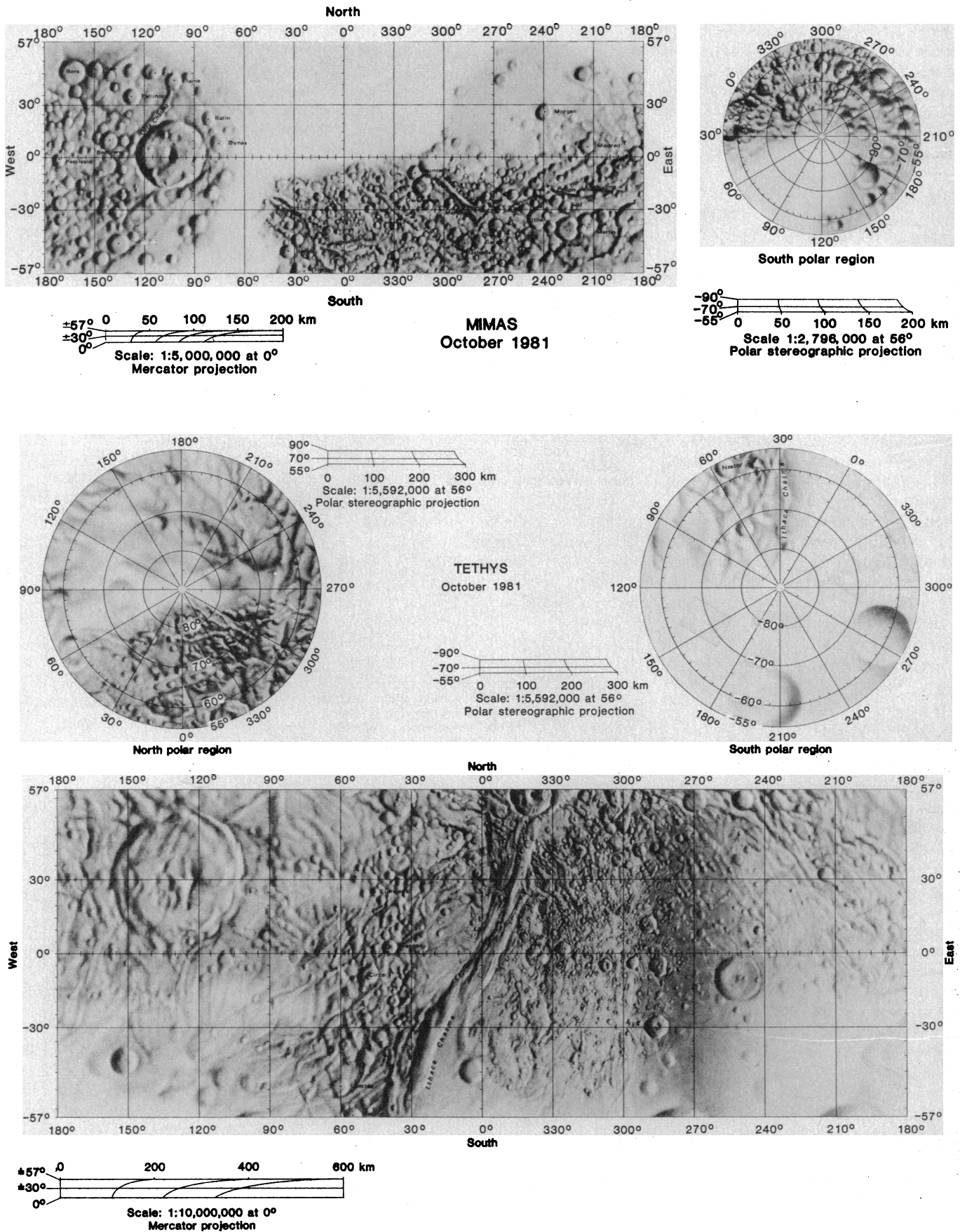
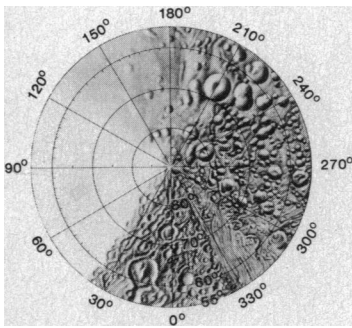
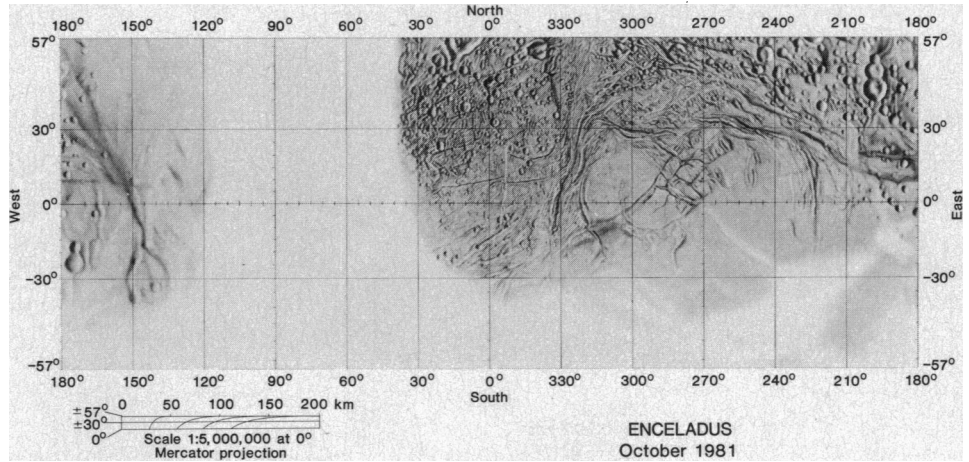
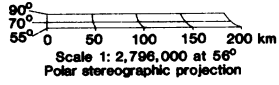


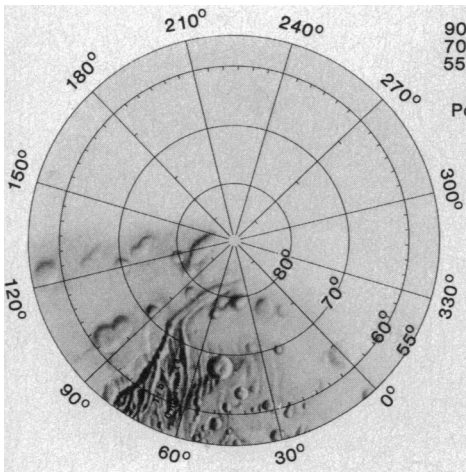
Fig. 16. Cartographic base maps (pages 513–516) of six of Saturn's classically known satellites, based on a combination of Voyager 1 and Voyager 2 data. Both albedo variations and topographic forms are portrayed.



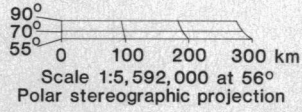
North polar region



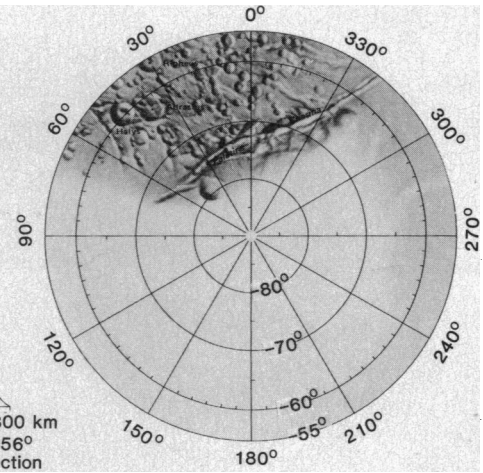
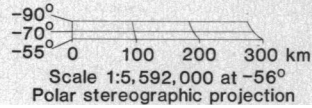
ENCELADUS
October 1981



North polar region



DIONE
October 1981



South polar region

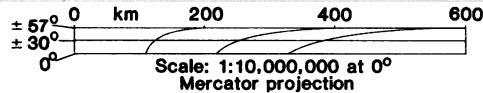
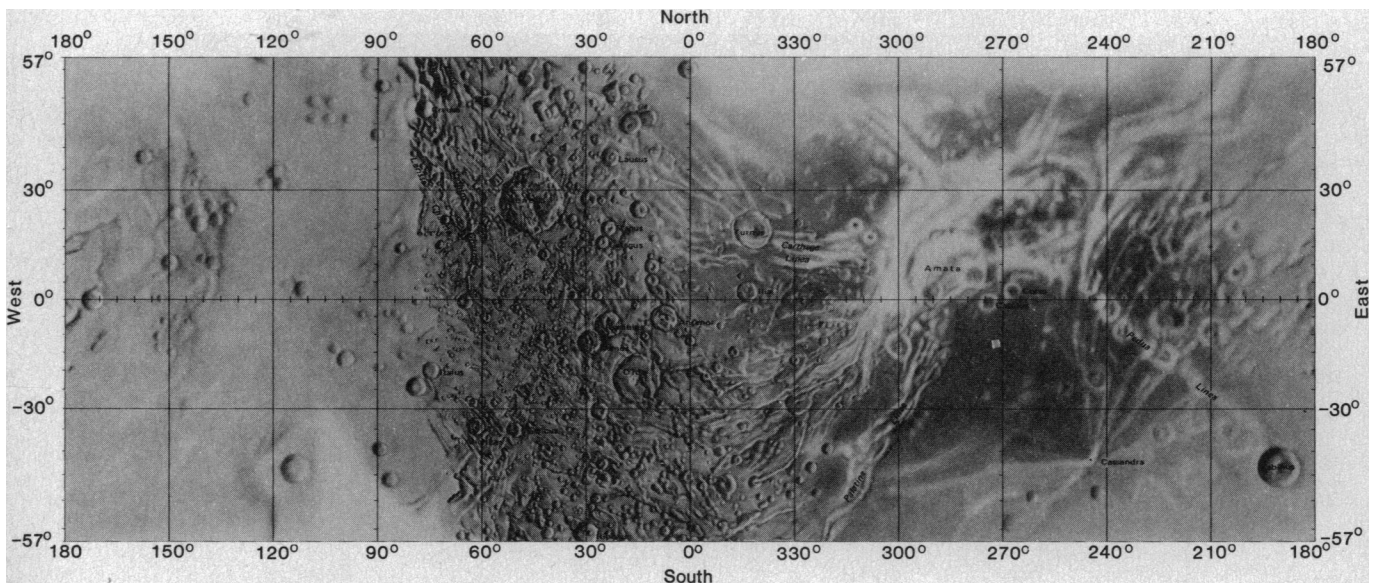


Fig. 16 (continued)

earth-based (small phase angle) observation, and the imaginary part was determined in each case by requiring the computed geometric albedo to agree with the observed value (40).

At northern mid-latitudes, the ratio of the peak brightness of the main haze layer at phase angle 155° to that at 140° was observed to be 2.0 ± 0.2 . This ratio can be reproduced by aerosols having $\bar{r} = 0.25$ or $0.5 \mu\text{m}$. By also using the observed absolute value of the peak brightness at 155°, which is 0.7 that of a perfectly reflecting normally illuminated Lambert surface, we find that the larger value of \bar{r} is correct. The inferred value of \bar{r} depends somewhat on the choice of the real part of the refractive index, larger values of which lead to smaller values of \bar{r} .

Preliminary analyses of high phase angle images from Voyager 1 resulted in a somewhat smaller value for \bar{r} (4). How-

ever, more refined analyses yield a value closer to the one cited above. At this point there is no evidence that \bar{r} varied over the 9-month interval between the two encounters. A preliminary study of the dependence of the peak brightness ratio on latitude shows that this ratio varies by no more than 20 percent over the entire limb, and therefore \bar{r} does not vary greatly with latitude.

The estimate of $0.5 \mu\text{m}$ for \bar{r} is in crude agreement with a value determined from very low phase angle ground-based observations (40) and in poor agreement with a value of about $0.08 \mu\text{m}$ determined from Pioneer 11 polarization data (41). As pointed out in (4), one explanation for the latter discrepancy may lie in the assumption that the single-scattering behavior of spheres adequately represents the true behavior of the Titan aerosols. On theoretical and experimental grounds, the high phase angle brightness

values should be far less sensitive to particle shape than is polarization (39). That is, the derived \bar{r} is such that the mean cross-sectional area of the particles is $\pi\bar{r}^2$ to a good approximation. We verified this conclusion in preliminary calculations for prolate spheroids. Furthermore, we found that the high polarization needed to reproduce the Pioneer 11 observations, and presumably the corresponding data obtained by the Voyager 2 photopolarimeter experiment (42), can be achieved with very elongated particles having \bar{r} values in the range required by the high phase angle brightness results. By contrast, we were not able to simultaneously fit the various data sets with spherical particles that had either a very broad or a bimodal size distribution.

We also conducted a preliminary study of the physical properties of the upper haze layer. At northern latitudes,

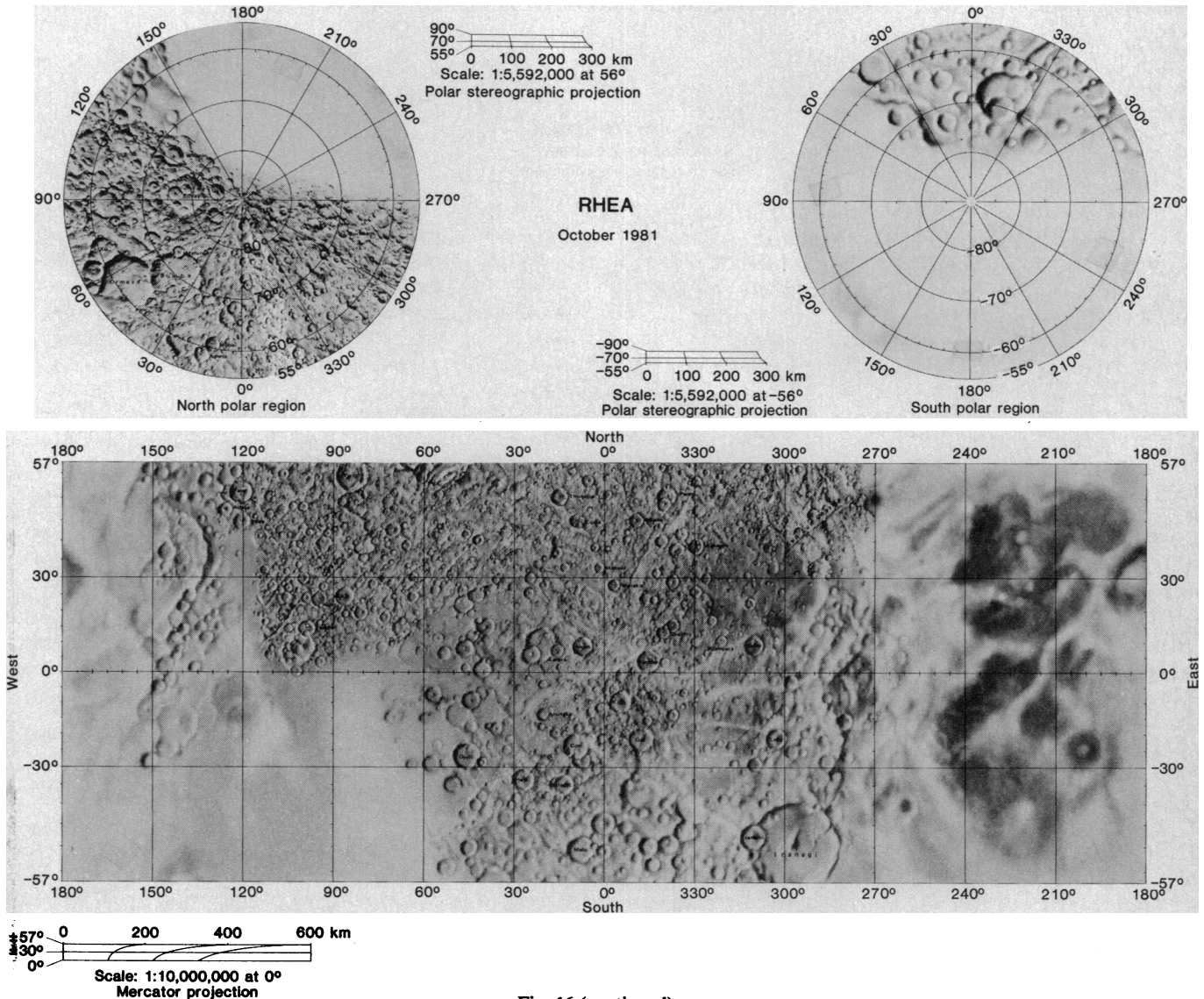


Fig. 16 (continued)

the ratio of the brightness at the center of this layer (point A of Fig. 14) at 155° and 140° phase angles is 3.3 ± 0.3 . We simulated this ratio with a single-scattering calculation, as the upper haze layer is optically thin and Titan has a low albedo. We found a unique r value of $0.3 \mu\text{m}$, as the observed ratio lies close to the maximum in the plot of this ratio as a function of \bar{r} .

The optical depth τ above the center of the upper haze can be found from the observed absolute value of the brightness at the center of the layer at 155° phase angle. For this purpose we used the value of \bar{r} found above to define the single-scattering phase function, assumed the single-scattering albedo is similar to that for the main haze layer, and used the solution to the radiative transfer equation for single scattering and a spherical atmosphere. In accord with Fig. 14, we set the haze scale height at 40 km. In this way we found $\tau = 0.0065 \pm 0.002$ from the center of the upper haze layer to the top of the atmosphere and hence $\tau = 0.013 \pm 0.003$

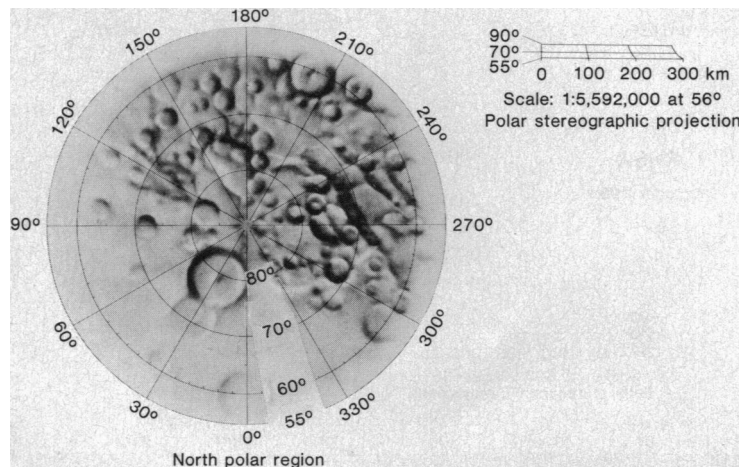
for the entire upper haze layer. This value is significantly smaller than the one quoted in (4), primarily because of an error in the latter. In view of this small value and the fact that the brightness of the upper haze layer does not vary greatly along the limb, we conclude that it cannot play an important role in generating the north-south brightness asymmetry.

Very severe constraints on the occurrence of breaks in the aerosol layer can be placed as a result of the high surface pressure and correspondingly large Rayleigh scattering optical depths. Because Titan's surface pressure is 1.6 times that of the earth and its surface gravity is about six times smaller, molecular scattering optical depths are approximately ten times larger for Titan. For example, the optical depths are about 3.8, 1.6, and 0.75 at wavelengths of 0.4, 0.5, and 0.6 μm , respectively. The corresponding geometric albedos for a clear atmosphere and a nonreflective surface are about 0.47, 0.35, and 0.24, respectively. The uniform reddish color of Titan (Fig. 13)

Fig. 17. Montage of the eight satellites of Saturn (Mimas, Enceladus, Tethys, Dione, Rhea, Iapetus, Hyperion, and Phoebe) shown to scale. Relative albedo and color have been preserved qualitatively for comparison. Except for Phoebe, the albedos are all values scaled to zero phase angle, although some of the pictures themselves depart significantly from zero phase. The Phoebe image has been arbitrarily brightened to compensate for its low albedo. The images of Mimas, Dione, and Rhea are from Voyager 1 (4); Voyager 2 data are used for Enceladus (2 km/lp), Tethys (10 km/lp), and Iapetus (21 km/lp). [Montage prepared by J. A. Mosher, JPL Image Processing Laboratory]

and its uniform low albedo at all visible wavelengths imply that the smog layer is omnipresent.

As illustrated in Fig. 13 and more quantitatively in Fig. 15, the normal albedo has a local minimum at about 70°N. This dark ring was probably also present at the time of Voyager 1, although it was less sharply defined in the images because of the more oblique views of the north polar region obtained from that spacecraft.



IAPETUS

October 1981

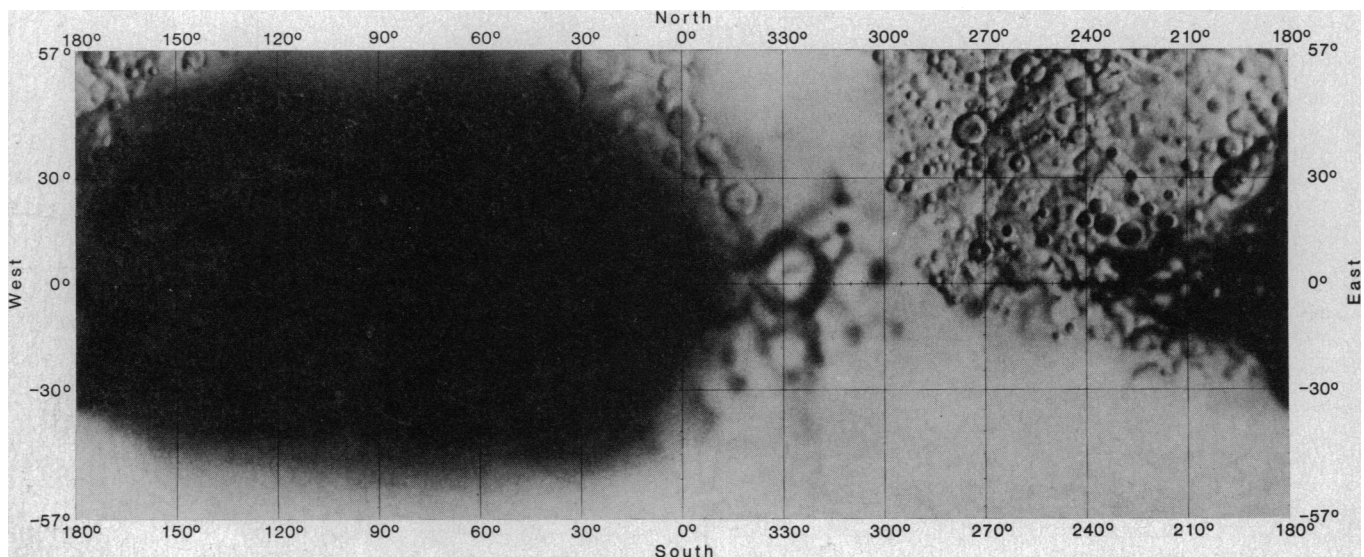
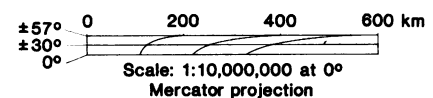


Fig. 16 (continued)

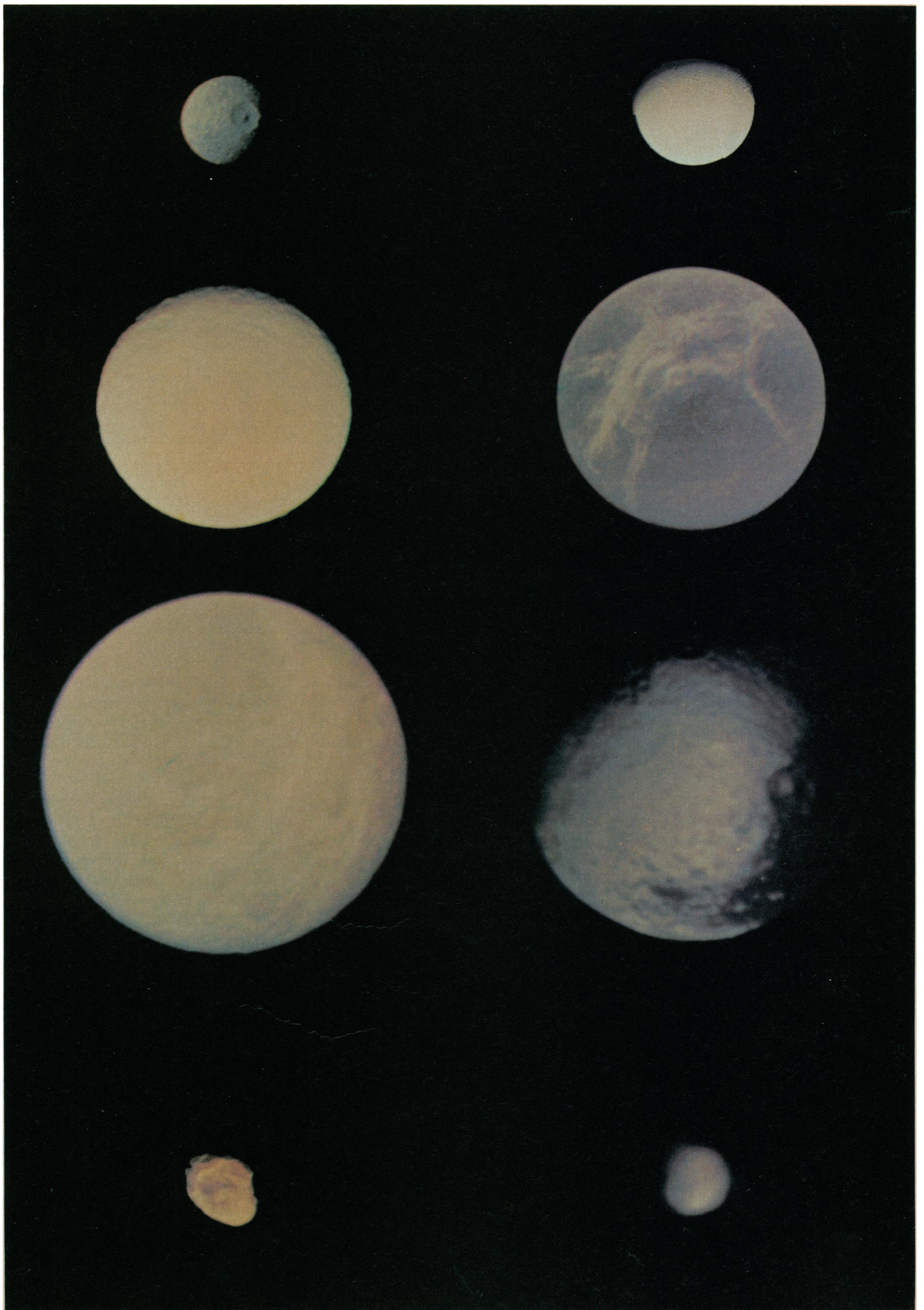




Fig. 18. Montage of the eight known small satellites of Saturn. From left: 1980S28 (the A ring shepherd); 1980S27 and 1980S26 (the F ring shepherds); 1980S1 and 1980S3 (the coorbitals); 1980S13 and 1980S25 (the Tethys Lagrangians); and 1980S6 (Dione B). Images are to correct relative scale.

The IRIS spectra of Titan obtained by Voyager 1 had sufficient spatial resolution to distinguish between Titan's northern and southern hemispheres (11, 25). At 68°N most of the minor species were enhanced, especially C₃H₄, C₂N₂, and HC₃N. This was not an effect of the difference in slant path, since the acetylene, ethane, ethylene, and methane peaks were reduced (it is colder at this latitude and altitude) and HCN and C₃H₈ abundances were uniform at all latitudes. Strobel (43) pointed out that formation of the more complex molecules is favored at low temperatures because these reactions are exothermic. As a result, the pathway toward the production of aerosols may be enhanced, thereby providing a possible explanation for the relative darkness of the satellite's northern hemisphere.

It seems likely that these hemispheric abundance differences are associated with the observed differences in color and albedo between the main haze layer near the north pole and elsewhere. Both sets of observations are presumably related to the seasonal difference in solar insolation in the two hemispheres (spring has just begun in the north). Details of the processes connecting these observations remain to be elucidated.

Satellites. The Saturnian satellite system is now known to consist of 15 regular satellites (those with nearly circular direct orbits approximately in Saturn's equatorial plane) and two other satellites, Iapetus and Phoebe. Iapetus is in a direct orbit inclined 15° to the plane of

the system; it orbits near the Laplace plane and therefore may also be counted among the regular satellites (44). Phoebe is in a retrograde orbit with an inclination of about 150°. In addition to the classically known nine satellites (those discovered before 1900), eight Saturnian satellites have been discovered since 1965 through a combination of earth-based, Pioneer 11, and Voyager 1 observations (45–48). The major distinction of the new satellites is that their orbits, while regular, display special dynamical features; they occur as paired coorbitals in the Lagrangian libration regions of larger satellites, or as ring "shepherds." Table 1 shows the general characteristics of the known Saturnian satellites.

The satellite observations by Voyager 1 included, along with a very close flyby of Titan (6500 km), close encounters with Mimas, Dione, and Rhea that yielded images with resolutions between 1 and 3 km per line pair (lp). Voyager 1 was also programmed to observe the coorbital satellites 1980S1 and 1980S3 and to search for new satellites (4). The Voyager 2 Saturn sequence was designed to complement the Voyager 1 observations with relatively high resolution coverage of Enceladus and Tethys, moderate resolution views of Hyperion and Iapetus, and the first observations of distant Phoebe. In addition, the preliminary Voyager 2 sequence was substantially modified to respond to Voyager 1 discoveries and recent earth-based discoveries of the small satellites (49). The final planned sequence was successfully

executed, except for the loss of the highest resolution Enceladus and Tethys coverage as a result of the seizure of the scan platform (50). In retrospect, the losses turned out to be relatively minor. Table 1 shows the best resolution obtained from the two encounters for each satellite, along with viewing and lighting conditions. Preliminary maps showing albedo and topographic features have been prepared from both Voyager 1 and Voyager 2 images (Fig. 16).

The Saturnian satellites are the first collection of intermediate-size objects in the solar system to be observed closely; their dimensions range from asteroidal to lunar. Figures 17 and 18 show 16 satellites to the same scale with approximately the correct relative albedo and color. Titan, which is treated separately, is omitted. The relative brightness of Phoebe has been increased in this presentation. If portrayed in its true relative brightness it would not be visible against dark sky. Earth-based telescopic visible and near-infrared data and Voyager 1 observations show that most of the satellites are bright objects, with water ice or frost on their surfaces. Where measured, they all have low densities (less than 2 g cm⁻³; see Table 1), which suggests that large fractions of their bulk composition must be low density, nonrocky material, probably predominantly water and ice (4, 51). Despite these indications of a primitive compositional character and speculations of a cold origin, the Voyager images show a surprising diversity of evidence for endogenic activity on many

of the satellites. Along with data for the Galilean satellites, these observations suggest that there may be many combinations of energy sources (tidal heating, short-lived radionuclides, accretion of impact heating, as well as long-lived radionuclides) and composition (particularly low melting point condensates) that can give rise to internal melting and geological activity in small, predominantly icy bodies.

The spectral reflectance of the satellites provides clues to their surface composition and state. Studies in the near infrared showed that all the larger satellites have strong absorption bands due to water ice or frost (53). Spectral reflectance in the visible and ultraviolet for most of the satellites indicates a redder color than would be expected for pure frost. In this respect, their color is similar to that of Ganymede and Callisto although somewhat less red. Figure 19 shows preliminary values of spectral albedo from Voyager data. The curves represent average properties for specific regions of the satellites calculated from raw image data. Camera calibration factors were derived from instrument calibration sequences and observations of the Galilean satellites (54); these data have not yet been compared in detail to ground-based measurements. Zero-phase normal albedos have been crudely approximated by dividing the raw photometry by $\cos \alpha$, where α is phase angle; in most cases the estimates agree to within 10 percent with the integral disk geometric albedos in Table 1. Important points illustrated by Figs. 17 and 19 and Table 1 are the extraordinarily high albedo of Enceladus (which may be the most reflective object in the solar system), the generally high albedo of the larger satellites (mostly above 0.5), and the very low values for Phoebe and the dark side of Iapetus (0.05 to 0.06).

Small satellites. Images were obtained from Voyager 1 and Voyager 2 of the eight minor (as opposed to classical) satellites in the inner part of the Saturnian satellite system. The outer three are trapped in the Lagrangian libration regions of Dione and Tethys, which are stable regions along the orbit centered at 60° ahead of or behind the major satellite. Dione has one leading Lagrange satellite (1980S6), discovered by the French astronomers P. Laques and J. Lecacheux (46). Tethys has one leading Lagrange satellite (1980S13), discovered by B. A. Smith and co-workers at the University of Arizona (47), and one trailing one (1980S25), discovered in ground-based tests of the Space Telescope wide field camera (48). All three of these ob-

Table 1. Saturn satellite properties.

Name	Orbit (km)	Orbit (R_S)	Period (hours)	Additional name	Radius ^a (km)	Mass ^b (10^{23} g)	Density (g cm^{-3})	Visual albedo	I/F at 0°	Best resolution (km/lp)	Phase angle (deg)	Voyager
1980S28	137,670	2.282	14.446	A ring shepherd	10×20				0.4	13	14	1
1980S27	139,350	2.310	14.712	F ring shepherd	$70 \times 50 \times 40$				0.6	7	30	2
1980S26	141,700	2.349	15.085	F ring shepherd	$55 \times 45 \times 35$				0.6	8	67	2
1980S3	151,422	2.510	16.664	Trailing coorbital	$70 \times 60 \times 50$				0.4	3	57	1
1980S1	151,472	2.511	16.672	Leading coorbital	$110 \times 100 \times 80$				0.4	6	75	1
Mimas	185,540	3.075	22.618	S1	196 ± 3	0.375 ± 0.008 (0.455 ± 0.054)	1.19 ± 0.05 (1.44 ± 0.18)	0.6	0.7	2	77	1
Enceladus	238,040	3.946	32.885	S2	250 ± 10	0.84 ± 0.30	1.2 ± 0.4	0.9	1.0	2	42	2
Tethys	294,670	4.884	45.307	S3	530 ± 10	7.55 ± 0.90	1.21 ± 0.16	0.8	0.8	2	37	2
1980S13	294,670	4.884	45.307	Lagrangian	$17 \times 14 \times 13$				0.6	12	30	2
1980S25	294,670	4.884	45.307	Lagrangian	$17 \times 11 \times 11$				0.8	5	39	2
Dione	377,420	6.256	65.686	S4	560 ± 5	10.5 ± 0.3	1.43 ± 0.06	0.62	0.7	3	66	1
1980S6	378,060	6.267	65.738	Lagrangian	$18 \times 16 \times 15$				0.5	6	88	2
Rhea	527,100	8.737	108.42	S5	765 ± 5	24.9 ± 1.5	1.33 ± 0.09	0.65	0.6	1	70	1
Titan	1,221,860	20.253	382.69	S6	2575 ± 2	1345.7 ± 0.3	1.88 ± 0.01		0.2	1	36	1
Hyperion	1,481,000	24.55	510.64	S7	$205 \times 130 \times 110$				0.2	9	72	2
Iapetus	3,560,800	59.022	1903.94	S8	730 ± 10	18.8 ± 1.2	1.16 ± 0.09		0.5	17	80	2
Phoebe	12,954,000	214.7	13210.8	S9	110 ± 10				0.06	38	8	2

^aTitan radius is from Lindal *et al.* (29); all others are from Voyager images. ^bThe first Mimas mass and the Enceladus mass are from Kozai (52); all others are from Tyler *et al.* (51).

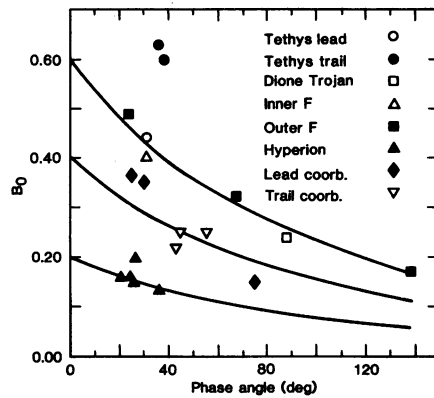
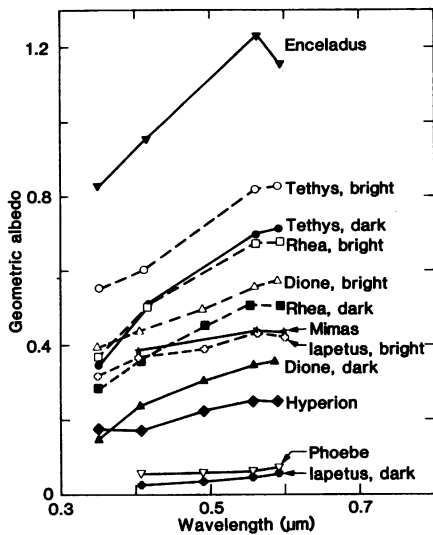


Fig. 19 (left). Spectral albedo curves for several satellites derived from photometric analysis of Voyager 2 images taken through ultraviolet (325 ± 45 nm), violet (400 ± 50 nm), blue (480 ± 50 nm), green (570 ± 40 nm), and orange (590 ± 30 nm) filters. Filter spectral

ranges indicate the half-maximum response of the entire optical and detector system. Fig. 20 (right). Photometric measurements of the surface brightness of the small satellites from Voyager 2 images taken with clear (450 ± 150 nm) filter plotted as a function of phase angle. Also shown are a family of plausible phase curves.

jects are approximately 15 km in mean radius. Interior to the orbit of Mimas are two coorbital satellites, discovered by A. Dollfus and by J. Fountain and S. Larson from plates taken in the 1960's (55). These two objects were observed by Voyager 1 to be in orbits separated by

about 50 km (4); consequently, they have different orbital periods and approach and interact gravitationally about every 4 years. During this interaction the innermost, trailing coorbital satellite approaches its companion and gravitationally extracts orbital momentum from it.

The added momentum raises it to a higher orbit, slowing it down relative to its companion, which is dropped to a lower, faster orbit. The remaining three minor satellites were discovered in Voyager 1 images in October and November 1980. Two were orbiting as a pair, one inside and one outside the narrow F ring, while the third orbited just outside the A ring and may be partly responsible for the sharpness of the ring edge.

Table 1 includes the orbital characteristics and sizes of the eight minor Saturnian satellites, as they are now known. Figure 20 summarizes the Voyager 2 clear-filter photometry, which was analyzed for us by P. Thomas of Cornell University. There is no significant trend of surface brightness or color as a function of distance from Saturn among the small satellites. The outer F ring shepherd and the trailing coorbital satellite have green/violet ratios similar to that of Hyperion and somewhat higher than that of the B ring and Enceladus.

Voyager observations of the outer F ring shepherd (1980S26) span a sufficient range of phase angles to allow us to define the phase dependence of brightness with some confidence. This phase curve leads to a normal reflectance at

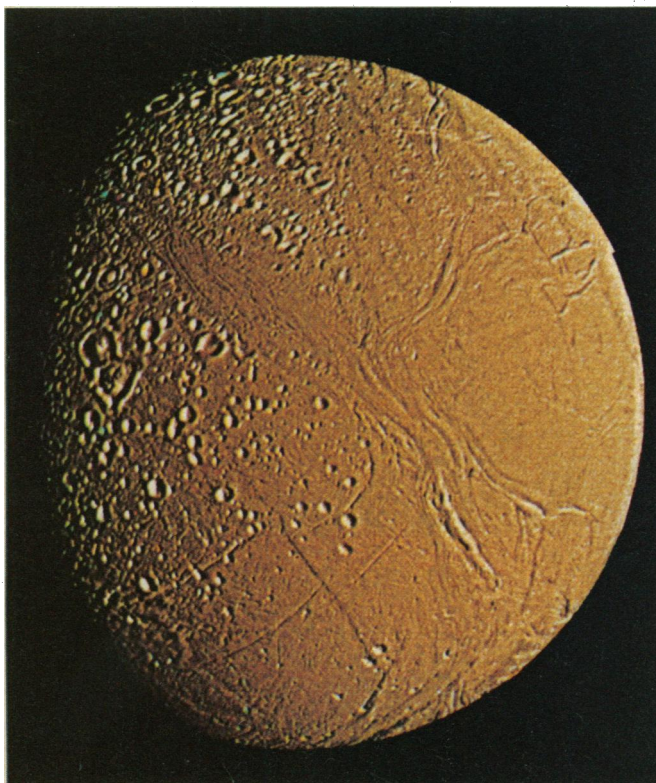
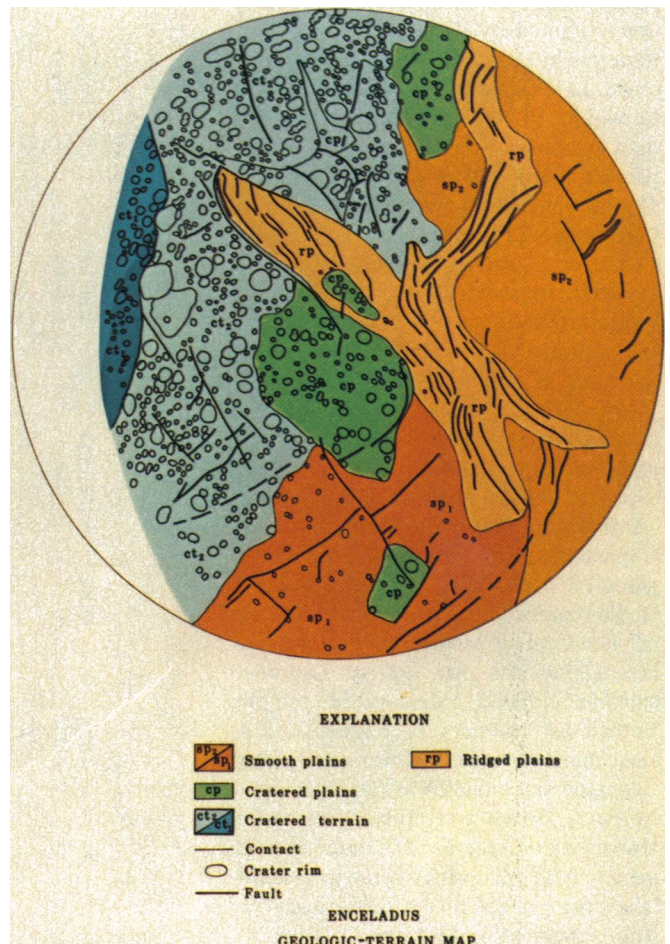


Fig. 21 (left). Voyager 2 mosaic of highest resolution images of Enceladus (2 km/lp), filtered for maximum spatial discrimination. [Color mosaic prepared by C. C. Avis, JPL Image Processing Laboratory] Fig. 22 (right). Sketch map of terrains on Enceladus. The abundance of craters and the occurrence of other landforms (faults and ridges) have been used to differentiate among the terrains.



opposition of 0.63 for this satellite, and a phase coefficient of 0.017 mag/deg for an equivalent spherical body. A family of phase curves of this sort superimposed on the data in Fig. 20 yields normal reflectances of about 0.6 for the inner F ring shepherd and the leading Lagrange satellites on the orbits of Tethys and Dione. The coorbital satellites appear to have normal reflectances of about 0.5, and Hyperion has a normal reflectance of about 0.3. Note that all of these values refer to clear-filter observations, which have a bandpass centered at 0.48 μm , somewhat bluer than the standard visual filter. We conclude that there is a wide range of normal reflectances of the small satellites, even allowing for the modest differences in phase coefficients possible for these objects.

Enceladus. Voyager 1's best observations of Enceladus were of low resolution (25 km/lp) but revealed a body of anomalously high albedo (normal albedo close to 1.0) and low relief. Its surface lacked the deep pockmarks observed on its sister satellite, Mimas. A variety of observations indicated that an unusual surface would be revealed on Enceladus when the satellite was viewed by Voyager 2 at higher resolution. Yoder (56) noted that Enceladus' orbital eccentricity is forced by an orbital resonance with Dione, much like the orbital resonance between Io and Europa (57). Therefore Enceladus might have been subjected to tidal heating. Questions were raised, however, about whether tidal heating would be effective (58). The coincidence of the densest part of the E ring with Enceladus' orbit further suggested that current eruptive activity on the satellite might be the source of the ring (59). These factors, together with Enceladus' extremely high albedo, suggested that Enceladus might be geologically active at present.

Voyager 2 images of Enceladus showed that the object is the most geologically evolved and youthful of the Saturnian satellites and has a wide diversity of terrains (Fig. 21). At least five distinct terrains have been identified on the basis of crater populations and other landforms (Fig. 22). These terrains include two types of cratered plains observed along the terminator. One terrain has craters 10 to 20 km in diameter that are highly flattened (ct_1) and the other has 10- to 20-km craters whose topography is well preserved (ct_2); evidently the thermal histories of these two regions have been different. A third cratered plains unit occupies the central part of the disk visible in Fig. 21. In this unit (cp), bowl-shaped craters 5 to 10 km in

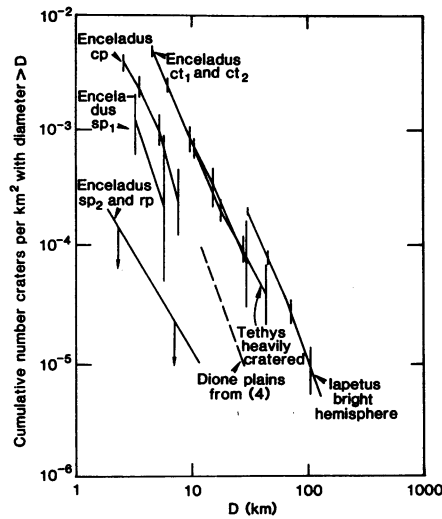


Fig. 23. Cumulative size-frequency distribution of presumed impact craters on Enceladus, compared with distributions for other objects. Error bars represent counting statistics and are proportional to \sqrt{N} , where N is the number of craters in the sample.

diameter are the principal landform, and the crater population is roughly a third that of the older terrains (ct_1 and ct_2). In the lower part of the image (roughly in the equatorial region), a fourth major province of smooth plains is identified (sp_1); here an open rectilinear pattern of grooves is the dominant landform. These grooves extend northward into unit sp_1 . Craters 2 to 5 km in diameter are sparsely distributed over the grooved surface. This crater population on the unit is about an order of magnitude lower than that of cp . The youngest units consist of smooth plains (sp_2) and ridged plains (rp), which are nearly free of craters at the limit of the Voyager 2 resolution (2 km/lp). This terrain consists of a variety of landforms, including smooth plains and complex, subparallel ridges that bound the unit along its contacts with older terrain. Some ridges have more than 1 km of relief. A corridor of the ridged plains unit extends nearly to the north pole (near the terminator in the upper part of the image). Along the margin of the corridor several stages in the development of ct_2 can be recognized. Evidently a section of the older ct_2 unit was replaced, and craters formed on the new crust became highly flattened. Later, ridged plains were formed in the corridor, clearly at the expense of part of ct_2 . Closer inspection reveals that much finer (but perhaps less convincing) subdivision of terrains of different ages is possible. In any case, Enceladus has had a complex geologic history during which the surface has been replaced in multiple stages.

Figure 23 presents the crater size-fre-

quency distributions for units ct_1 and ct_2 (combined), cp , sp_1 , an upper limit of the crater density for sp_2 and rp (combined), and comparison distributions for other satellites. The cratered plains on Enceladus (cp) have a crater density comparable to the least cratered surface seen on any of the other Saturnian satellites by Voyager 1, the smooth plains in Dione's leading hemisphere. The crater density on the ridged plains of Enceladus is lower by at least a factor of 50. The present global mean rate of cratering on Enceladus' surface by impact of comet nuclei is estimated to be $1.0 \times 10^{-14} \text{ km}^{-2} \text{ year}^{-1}$ (Table 2), which is about equal to the present rate of lunar cratering by both asteroids and comets. On the basis of the global mean rate, a maximum of about 10^9 years is implied for the ridged plains by the upper bound of crater density. It should be noted that much of the ridged plains unit occurs in the trailing hemisphere, where the rate of cratering by comet impact is very much less than the global average. The corridor of ridged plains that extends to the pole (see Fig. 16), however, is crater-free at this resolution and occurs in a region where the cratering rate would be close to average. Hence, an upper limiting age of 10^9 years is the best estimate. This age is on the order of one-fourth the age of the satellite. A major episode of resurfacing of Enceladus appears to have occurred relatively late in the history of this unusual body.

Two styles of tectonic deformation are observed on Enceladus. Linear grooves in sp_1 that intersect in orthogonal patterns are probably graben; they probably indicate crustal segmentation by extension and brittle fracture. The curvilinear valleys and ridges of the ridged plains, on the other hand, suggest crustal folding or faulting under compression. The ridges on Enceladus most nearly resemble some features of the grooved terrain found on Ganymede, particularly in the north polar region, although the latter displays greater regularity in spacing and height of ridges and grooves. On Enceladus there are double ridges with intervening valleys, one-sided valleys (possible fault scarps), and simple grooves resembling graben. The character of the ridges commonly changes along their length. Most models for formation of the grooved terrain on Ganymede involve normal faulting accompanied by extrusion of fluids (water or water slurries). The Enceladus ridged plains in the corridor extending to the north pole may have been formed by a similar process. In the major region of ridged plains, however, the ridges tend to form a concentric

pattern near the border of the unit. One possibility is that they are pressure ridges formed by convective upwelling and formation of new crust in the center of the unit and compression and folding of the crust along the margins.

The question of what drives the geologic activity on Enceladus remains. For such a small icy body, significant heating by radionuclide decay at a late stage in its history seems implausible. Although there remain theoretical difficulties with achieving the efficiencies required to heat Enceladus by tidal interactions, this mechanism, in some form, is the best candidate for supplying the energy to heat the satellite at intervals through its history. It has been suggested that early melting of a mixture of water and ammonia ices might have produced enough internal differentiation to allow efficient tidal coupling to a solid crust over a soft or fluid interior (60).

The large difference in topographic relaxation of craters in ct_1 and ct_2 provides an important clue to the early thermal history of Enceladus. Calculations carried out by Q. R. Passey, California Institute of Technology, show that

a thermal gradient of the order of tens of degrees per kilometer must have existed under ct_1 for craters as small as 10 km to collapse by viscous or plastic flow of the icy crust. This implies depths of water, water-ammonia solutions, or warm convecting ice of only a few kilometers during the period of viscous relaxation. Yet the shapes of 10-km and larger craters on nearby parts of ct_2 are essentially unaffected by flow of the crust. Evidently, subsurface fluids or warm convecting ice approached the surface only in restricted regions. This may indicate that the dissipation of tidal energy occurred chiefly in restricted parts of the subsurface. Development of local fracture systems, perhaps initiated by large impacts, may have allowed the tidal heating to be strongly localized.

Tethys. The best Voyager 1 images of Tethys were of low resolution (15 km/lp), but revealed a densely cratered surface with an enormous trough (Ithaca Chasma) centered in the Saturn-facing hemisphere. Those images showed Ithaca Chasma extending more than 140° with an average width of about 100 km. Rough estimates, based on the bright-

ness of the sun-facing walls, suggest that the trench might be 3 to 5 km deep.

Voyager 2 viewed principally the opposite hemisphere at substantially higher resolution. Figure 24 shows an enormous flattened crater in the leading part of the outward-facing hemisphere. This crater is about 400 km in diameter, about 40 percent of the diameter of the satellite. It is the largest crater with a well-developed central peak found so far in the solar system. Images of this large impact feature on the limb of Tethys show that the floor has rebounded tens of kilometers above the subdued rim. The circular profile of the limb was evidently restored by creep or viscous flow in the lithosphere of Tethys. A large crater on Mimas with about one-third this diameter is extremely well preserved, and its floor remains depressed well below the surrounding surface (4). Calculations by Q. R. Passey show that, assuming similar thermal gradients and compositions for the lithospheres of the two satellites, the great crater on Tethys could be largely flattened over geologic time, while that on Mimas could retain its original shape. A deeper and warmer part of the litho-

Table 2. Present cratering rates and past production of large craters on the satellites of Saturn derived from observed crater density on Iapetus.

Satellite	R_{sat}^a (km)	Present cratering rate		Frequency for entire satellite (km^{-2})			Fate
		$\Gamma_{10\text{km}}^b$ (10^{-14} km^{-2} year^{-1})	$D_{3.3\text{GY}}^c$ (km)	$D =$ 10 km ^d	$D =$ R_{sat}^e	$D =$ D_{sat}^f	
Phoebe	110	0.128	8	0.0037	2.9	0.63	Probably captured near time of last global resurfacing of Iapetus
Iapetus	745	0.079	31	0.0023	0.83	0.18	Last global resurfacing is starting time for following events
Hyperion	139	0.18	10	0.0053	2.7	0.59	Probably formed by fragmentation of precursor near time of last resurfacing of Iapetus
Titan	2560	0.13	120	0.0038	1.1	0.24	Safe from disruption, probably accreted fragments from Hyperion precursor
Rhea	765	0.15	43	0.0038	1.4	0.29	Probably not disrupted
Dione	560	0.27	42	0.0079	3.0	0.66	Probably disrupted and reaccreted once
1980S6	16	0.61	2.5	0.018	14	3	Formed during last disruption of Dione
Tethys	530	0.43	52	0.013	4.9	1.1	Probably disrupted and reaccreted once
1980S13	15	0.84	2.6	0.025	19	4	Formed during last disruption of Tethys
1980S25	13	0.84	2.4	0.025	19	4	Formed during last disruption of Tethys
Enceladus	255	1.0	46	0.030	20	4.3	Disrupted and reaccreted about four times
Mimas	195	1.6	36	0.046	22	4.7	Disrupted and reaccreted about five times
(Coorbital parent) ^g	130	2.4	30	0.070	36	7.9	Disrupted early to form 1980S3 and 1980S1
1980S1	98	2.4	23	0.07	38	8	Disrupted and reaccreted about eight times
1980S3	61	2.4	15	0.07	42	9	Disrupted and reaccreted about nine times
(F ring parent) ^h	80	3.2	22	0.094	53	12	Disrupted early to form 1980S27 and 1980S26
1980S26	46	3.2	13	0.09	59	13	Disrupted and reaccreted about a dozen times
1980S27	55	3.2	16	0.09	57	12	Disrupted and reaccreted about a dozen times
1980S28	16	3.9	6	0.10	78	17	Formed as a fragment of 1980S27 at time of its last disruption
(A ring parent) ⁱ	200	3.9	86	0.114	54	12	Ground to "medium" size ring particles
(B ring parent) ⁱ	280	3.5	120	0.101	45	9.6	Ground to "medium" size ring particles
(C ring parent) ⁱ	70	7.9	30	0.23	134	29	Ground to "fine" ring particles

^a R_{sat} is root-mean-square radius of satellite adopted for calculation of crater production. ^b $\Gamma_{10\text{km}}$ is present rate of production of craters equal to and larger than 10-km diameter. ^c $D_{3.3\text{GY}}$ is most probable diameter of largest crater produced 3.3 billion years ago at present rate of cratering. ^d $D = 10$ km is density of craters equal to and larger than 10-km diameter that corresponds to observed crater density on Iapetus. ^e $D = R_{\text{sat}}$ is frequency of craters equal to and larger than radius of satellite that were produced since last global resurfacing of Iapetus. ^f $D = D_{\text{sat}}$ is frequency of craters equal to and larger than diameter of satellite that were produced since last global resurfacing of Iapetus. ^gHypothetical spherical parent body large enough to contain 1980S1 and 1980S3 as solid fragments. ^hHypothetical spherical parent body large enough to contain 1980S26 and 1980S27 as solid fragments. ⁱHypothetical spherical parent bodies large enough to contain the volume of the ring particles of A, B, and C rings.

sphere would flow under the Tethys crater than under the Mimas crater. A viscosity gradient corresponding to a thermal gradient of about 0.1 K/km is indicated for a thermal conductivity close to that of pure water ice.

Voyager 2's best global view of Tethys showed that Ithaca Chasma passes close to the north pole and down at least to the equator in this region (see Fig. 16). It extends at least 270° around the satellite. If the satellite were once a ball of liquid water covered with a thin solid crust, freezing of the interior would have produced expansion of the surface comparable to the area of the chasm. It is not clear, however, why the extension would be concentrated in a single narrow lane rather than distributed among multiple faults over the surface. Figure 16 shows that Ithaca Chasma lies roughly along the intersection with the surface of a plane that is approximately normal to the radius through the center of the large crater on the leading hemisphere. This suggests that there may be a connection between the giant crater and the development of the chasm.

The best global view of Tethys (Fig. 25) shows that it, like several other Saturnian satellites, exhibits terrains of different geologic ages. The region north of the equator has an extremely rough, hilly, densely cratered topography; most of the craters are highly degraded. The highest resolution images of Tethys expected from Voyager 2 were lost owing to the scan platform problem. Fortunately, one high-resolution image of the limb (Fig. 26) shows the hilly cratered unit. From this image the crater density can be estimated down to diameters less than 5 km.

Part of the trailing hemisphere seen in Fig. 26 exhibits a less rugged surface; a few large craters are present that are surrounded by plains with a considerably lower crater density than the hilly terrain. The plains were probably produced by a flood of material erupted from the interior. The flood may have surrounded large preexisting craters and overlapped their associated rim deposits. Alternatively, the size-frequency distribution of craters formed after the plains is bimodal.

Hyperion. This satellite, which moves in an elliptical orbit exterior to Titan, was imaged by Voyager 2 at resolutions down to 9 km/lp at phase angles of about 75°. Hyperion is an irregularly shaped object, approximately 410 by 260 by 220 km, with angular features and facets as well as rounded areas. The irregular shape suggests that the satellite is the remnant of a larger body that was de-

stroyed by collision. This is vividly illustrated in the stereo pair presented in Fig. 27.

Several large impact craters are visible on Hyperion. One is about 120 km in diameter and has 10 km of relief, judging from limb topography. Other deep craters 40 to 50 km across can be recognized in stereoscopic pairs of images. In addition, the surface is peppered with dozens of craters about 10 km in diameter and smaller. The most prominent topographic features are a series of scarps; they are

linked into one sinuous scarp nearly 300 km long that defines the boundary of a crude crateriform feature more than 200 km in mean diameter. In the center of this feature is a broad hump or dome. Limb profiles suggest relief of well over 30 km for some of the scarps. It is possible that the looping system of scarps defines the margin of a spall face 200 by 300 km across.

Clear filter data are consistent with the Voyager 1 estimate of a geometric albedo of ~ 0.3 . Hence Hyperion is one

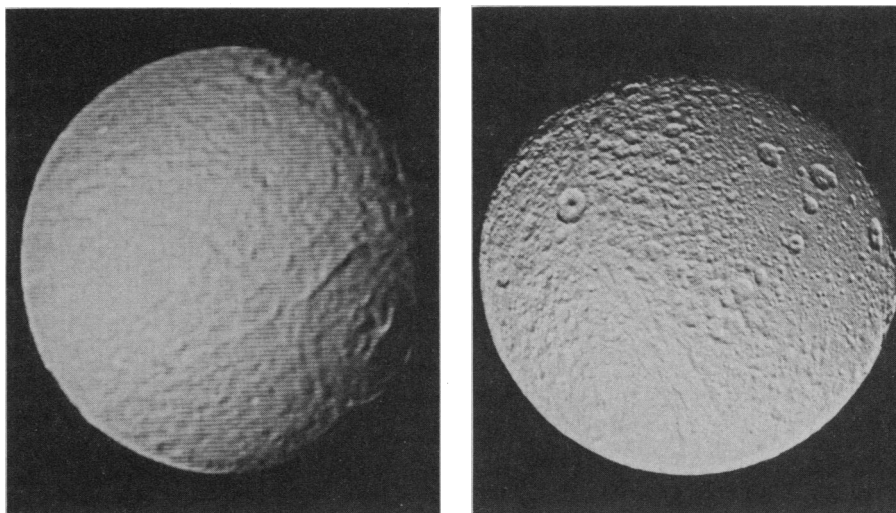


Fig. 24 (top left). View of the leading hemisphere of Tethys showing what is probably a 400-km-diameter impact scar. The image, which has been enhanced for maximum discriminability of small detail, has a resolution of 15 km/lp. Fig. 25 (top right). Highest resolution global view of Tethys, showing the trailing hemisphere at a resolution of 5 km/lp. Fig. 26 (bottom right). Highest resolution (2 km/lp) image of Tethys, showing a region of heavily cratered terrain. This image was to have been part of a mosaic that was lost when the spacecraft developed a small error in pointing near the time of closest Saturn approach but before its azimuthal motion failed.

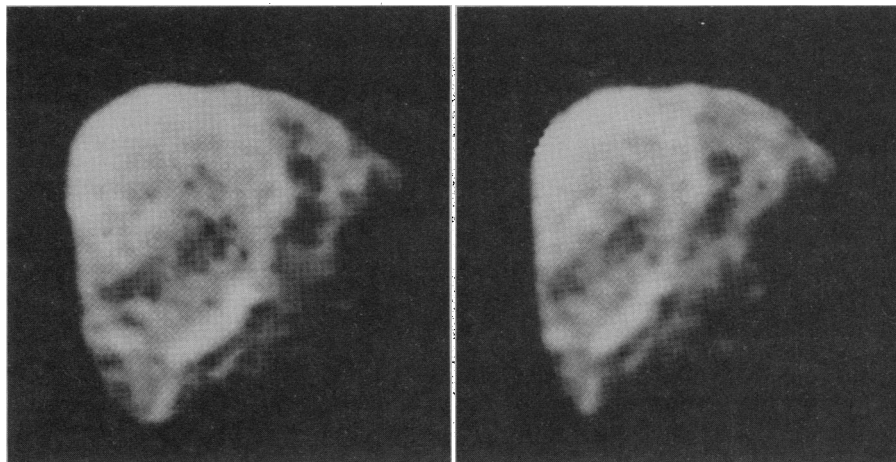


Fig. 27. Stereo pair of images of Hyperion with a resolution of 9 km/lp.

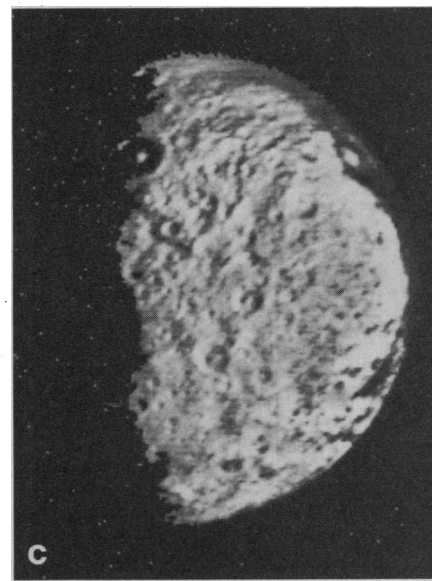
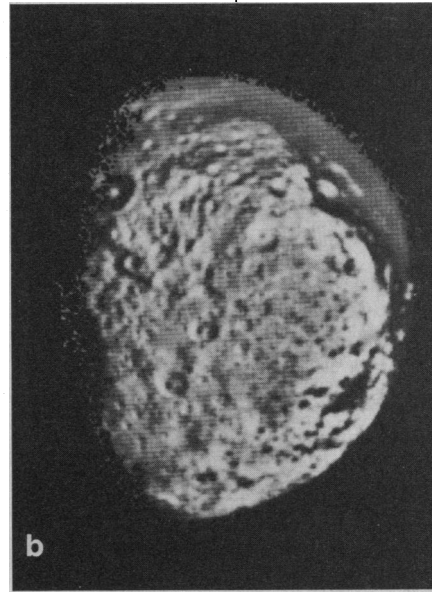
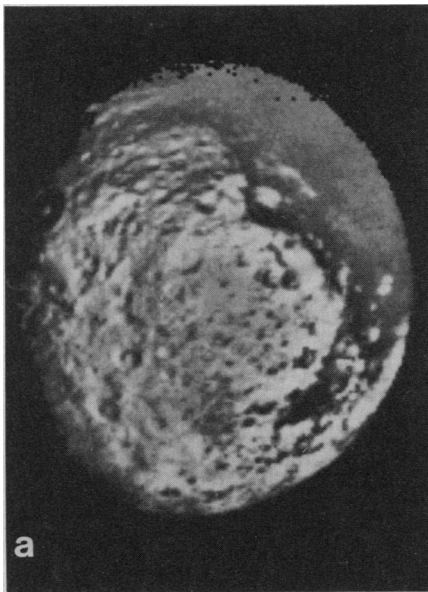


Fig. 28. (a to c) Sequence of Voyager 2 images of Iapetus' anti-Saturn-facing hemisphere. The border of the dark leading hemisphere is on the right, with some dark material extending into the bright trailing hemisphere near the equator. These images have a resolution of about 20 km/lp. Iapetus' north pole is very near the large crater at the terminator.

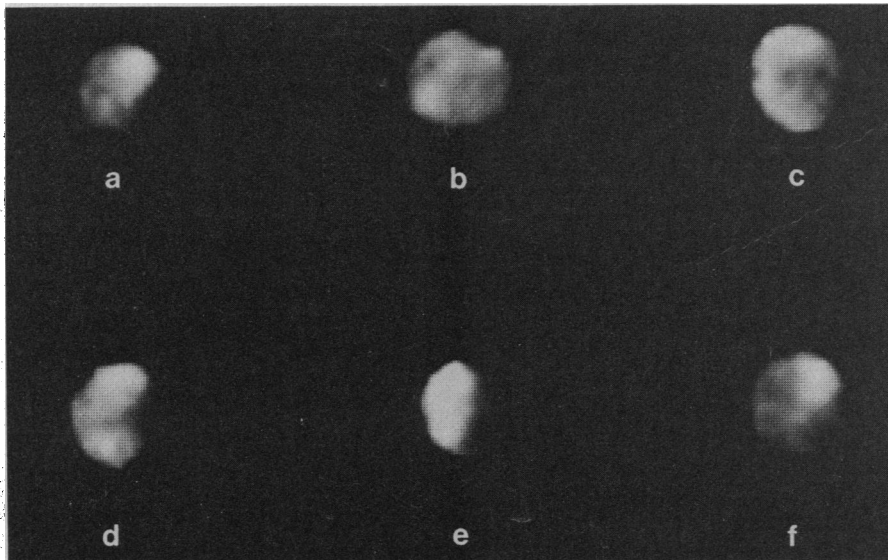


Fig. 29. Six views of Phoebe at a resolution of 40 km/lp. Frames (a) through (e) are spaced at approximately 70° longitude intervals, and (f) was taken one rotation after (a). The north pole of Phoebe's orbit is to the bottom and of Phoebe's rotation is to the top. The bright surface features, with contrasts up to 50 percent, are of unknown origin. The rotation period is 9 hours.

of the darkest objects in the Saturnian system. Its phase coefficient is 0.026 mag/deg, a value reasonable for a body of moderate albedo. Albedo variations of 10 to 20 percent are present over the surface.

Hyperion has the darkest surface in the Saturnian system from which absorption bands of water frost have been observed (61). While no mass estimate for Hyperion is available from the Voyager encounters, it is reasonable to suppose that, like all the regular satellites of Saturn, Hyperion contains a significant fraction of ice in its interior. If this is true, the moderate surface albedo and incomplete frost cover may be due to contamination by extrinsic dark rocky material. If the dark material on the leading side of Iapetus is derived in part from Phoebe, as suggested by Soter (62), some of this material should also reach Hyperion and could darken and redden its surface. Titan would effectively eliminate any dust ejected from Phoebe that was not swept up by Iapetus or Hyperion but had spiraled in farther. Thus the surfaces of the satellites interior to Titan would not be contaminated by the dark material. This method of darkening requires that the rotation of Hyperion not be tidally locked to Saturn; otherwise it should show the same leading-trailing asymmetry of the darkened surface as does Iapetus.

Iapetus. Voyager 1 observations of Iapetus (4) confirmed ground-based observations (going back to the discovery of the satellite by J. D. Cassini in 1671) which show that the hemisphere leading in orbital motion about Saturn is about an order of magnitude darker than the trailing hemisphere. Although Voyager 1 images did not have sufficient resolution to show much topographic detail, a dark ring about 400 km in diameter centered near 5°N and 245°W was discovered that extends from the dark hemisphere into the bright hemisphere. A number of craters, just at the limit of resolution, were also seen. Surface resolution was improved from about 50 km/lp in the Voyager 1 images to about 20 km/lp in the Voyager 2 images. The highest resolution observations were obtained for the bright, trailing hemisphere at high northern latitudes. The Voyager 2 images (Fig. 28) reveal large numbers of craters and clarify the character of the boundary of the dark region, particularly where it extends into the trailing hemisphere (Fig. 16).

The airbrush map of Iapetus shown in Fig. 16 was derived from a combination of Voyager 1 and Voyager 2 images. The principal dark region is seen to be cen-

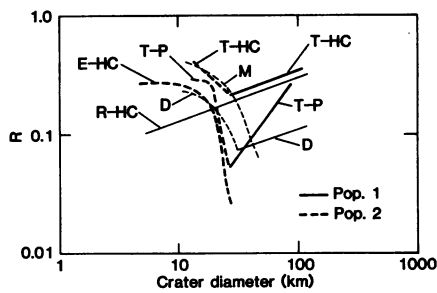


Fig. 30. Relative abundances of craters on the Saturnian satellites as a function of crater diameters. Voyager 1 data were used for the surfaces of Mimas (M), Dione (D), and Rhea's heavily cratered surface (R-HC). Voyager 2 data were used for Enceladus' cratered terrains (E-HC), Tethys' plains (T-P) and Tethys' heavily cratered terrain (T-HC). Parts of the curves inferred to be dominated by populations 1 and 2 are depicted by solid and dashed lines.

tered almost perfectly in the leading hemisphere. Ground-based telescope observations of the leading hemisphere must include bright regions near the poles; hence no ground-based observations of Iapetus are completely restricted to the dark material. Circular dark patches, probably dark-floored craters, occur in the bright region near the boundary and deep inside the trailing hemisphere. There are also some craters (for instance, near 200°W) that exhibit low-albedo patches suggestive of dark areas on their floors, perhaps parts of their walls facing the dark region. The contact relations in the trailing hemisphere strongly suggest that the dark material is superimposed on the bright, densely cratered terrain and is therefore younger than the cratered terrain. Although craters are clearly seen at the boundaries of the dark region, there is no hint, even in images in which many individual pictures have been summed to increase the signal-to-noise ratio, of bright-floored or bright-rimmed craters within the dark region that are well away from the boundary. Either the dark material is very thick or it is replenished at such a rate that fresh craters which penetrate the dark layer are quickly covered again.

Preliminary Voyager 2 broadband visible spectrophotometry indicates that the average normal albedo for the bright terrain is about 0.5, and for the dark region about 0.04 to 0.05. Thus the albedo contrast between bright and dark regions on Iapetus is a factor of at least 10. Both dark and bright areas are red (that is, the albedo increases at longer wavelengths) but there seems to be substantial variation in color from region to region. Typical green/violet color ratios are about 1.6 for the dark region and about 1.2 for bright areas. Substantial mixing

of bright and dark material may have occurred by ballistic diffusion. The red color of the bright areas may be due to a small admixture of redder dark material in a predominantly icy regolith. The very low albedo and red color of the dark material are inconsistent with dark silicates and suggest complex carbonaceous material of the type found in some carbonaceous meteorites and suspected on some dark red asteroids. Telescopic measurements of the dark hemisphere of Iapetus that cover a spectral range to 2.5 μm show a strong resemblance in spectral reflectance between the dark region and material extracted with organic solvents from a carbonaceous meteorite (63).

The origin of the dark, red, presumed carbonaceous material on Iapetus poses problems. The almost perfect symmetry of the principal dark area about the apex of motion suggests an exogenous origin, either through preferential ablation of ice by impacting debris revealing an underlying low-albedo material (64), or by accretion of low-albedo material spiraling in toward Saturn, under the influence of the Poynting-Robertson effect, from some source exterior to Iapetus, perhaps Phoebe (62). If the source of the dark material is endogenous, this remarkable alignment would have to be ascribed to coincidence, or perhaps to a secondary effect of some internal or impact event. In any event, examples of such hemispheric alignments are common in the solar system: the plains of Mars in the northern hemisphere, the lunar maria on the earth-facing hemisphere, the dark volcanic deposits on Io in the trailing hemisphere. The presence of dark-floored craters near the center of the trailing hemisphere, where they would be shielded from direct impact of particles encountered in Iapetus' orbital motion, points strongly to an internal origin. The nature of the contact between dark and light regions, moreover, suggests that the bright region was partially flooded with dark material that occupies topographically low areas. Notable is a large ring of dark material extending into the bright hemisphere photographed by Voyager 1 (4). This feature resembles large flooded multi-ring impact basins on the terrestrial planets. Overall, data from Voyager and from ground-based observations do not settle the question of an endogenous versus an exogenous origin for the dark material on Iapetus, and some combination of external and internal processes may be required.

Phoebe. Saturn's outermost satellite is in a retrograde orbit at a distance from the planet of nearly 13 million kilometers

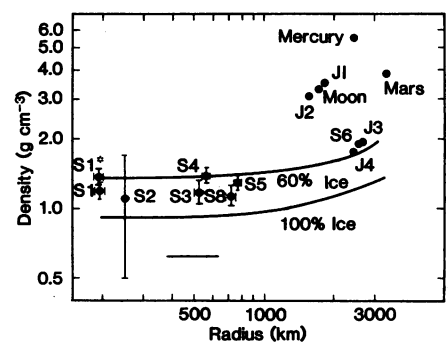


Fig. 31. Comparison of sizes and densities of the icy Saturnian satellites. Values for radii and densities are taken from Table 1. Two points are shown for Mimas; the lower value is based on the classical mass determination, the upper on the suggested revision by Tyler *et al.* (51) based on the new Tethys mass determination. Model curves for compression of ice and rock mixtures are from Lupu and Lewis (70).

(215 R_S); like the irregular outer satellites of Jupiter, it has been thought to be a captured object. Voyager 1 obtained no data on this distant body, so it was with considerable anticipation that images of Phoebe were received more than a week after the Voyager 2 Saturn encounter.

The Voyager 2 images (Fig. 29), acquired at a range of 2 million kilometers at 40 km/lp, show that Phoebe is a dark, approximately spherical object with a diameter of about 200 km. The observed surface brightness (I/F) at a phase angle of 30° was 0.03, and the measured phase function over the range 10° to 30° was 0.025 mag/deg. The corresponding albedo at zero phase is 0.06, approximately the same as for the dark side of Iapetus. Preliminary Voyager 2 color data also suggest that the surface is less red than the dark hemisphere of Iapetus, in agreement with ground-based multicolor photometric results (63). The combination of low albedo and UBV color (63, 65) are suggestive of a class of asteroids (RD) which apparently is common in the outer solar system and believed to be of primitive composition. Phoebe is possibly the first relatively unmodified primitive object in the outer solar system to be imaged from a spacecraft.

Although the Voyager images do not permit resolution of topographic features, its generally spherical appearance suggests that Phoebe has not been subjected to the catastrophic bombardment that apparently led to the fragmentation of satellites closer to Saturn. This does not indicate that Phoebe is a recently captured object; the gradient in flux of impacting bodies caused by the gravitational focusing of Saturn provides a plausible explanation for this difference. Phoebe is not uniform in appearance,

however; it shows a variety of features (probably albedo markings) with contrasts as great as 50 percent. From the motion of these features, a rotation period of about 9 hours is estimated.

Crater populations. Two distinct populations of craters (called populations 1 and 2) were discovered on the Saturn satellites imaged at close range by Voyager 1 (4). Figure 30 presents the crater statistics for the satellites in the form in which the two populations are most easily separated, that is, as frequency of occurrence as a function of crater diame-

ter relative to a standard distribution ($N \propto D^{-2}$, where N is the number of craters per unit area with diameters greater than D). Population 1 is characterized by a relatively high abundance of craters larger than 20 km, and population 2 by abundant craters smaller than 20 km and relatively few larger craters. Both populations were observed on Dione and Rhea; most craters observed on Mimas belong to population 2.

It was hypothesized in the Voyager 1 preliminary science report (4) that (i) population 1 was generated during the

tail-off of a postaccretional heavy bombardment, similar to that which cratered the highlands of the inner planets, and (ii) population 2 resembles, statistically, secondary populations on the terrestrial planets and has the form expected for debris generated by collision of objects with the satellites or other orbiting debris.

Voyager 2 observations show that the craters on even the oldest terrains of Enceladus belong to population 2. Craters on the hilly, heavily cratered terrain of Tethys belong to population 1, and most craters on the Tethys cratered plains region, particularly the smaller ones, represent population 2. A few large craters on the plains are anomalous, as can be seen in Fig. 30 (curve *T-P*). These are apparently population 1 craters that are older than the plains unit, and their rims project above the level of the eruptive material that formed the plains. They appear fresher than the typical degraded craters of the hilly terrain; it is conceivable that they represent a discrete pulse of large fragments generated late in the population 2 cratering.

Collisional evolution of the Saturnian satellites. The cratering record preserved on the Saturnian satellites provides a basis for inferring the history of collisional disruption of the satellites. In our model, the population on distant Iapetus is critical for understanding this history. The rate of cratering by impact of bodies external to the Saturnian system has been lowest on Iapetus and Phoebe and up to two orders of magnitude higher on the inner satellites. Therefore, if the craters on Iapetus were produced chiefly by external projectiles, then during the same period the inner satellites were cratered many times over with equal intensity.

Present cratering rates (Table 2) were derived from the estimated flux of long-period comets in the neighborhood of Saturn and from an estimated equilibrium population of short-period comets captured by Saturn from the long-period comet flux (66). Methods of estimating the size and flux of long-period comets in the vicinity of Jupiter have been presented (67). The flux of long-period comets crossing Saturn's orbit was obtained by extrapolation from the Jupiter-crossing flux by using a predicted distribution of perihelion distances of the long-period comet swarm (68).

Concentration and acceleration of impacting comet nuclei by Saturn's gravity field produces a steep gradient in cratering rate from the outermost to the innermost satellites. The present cratering rate on Rhea, for example, is about twice

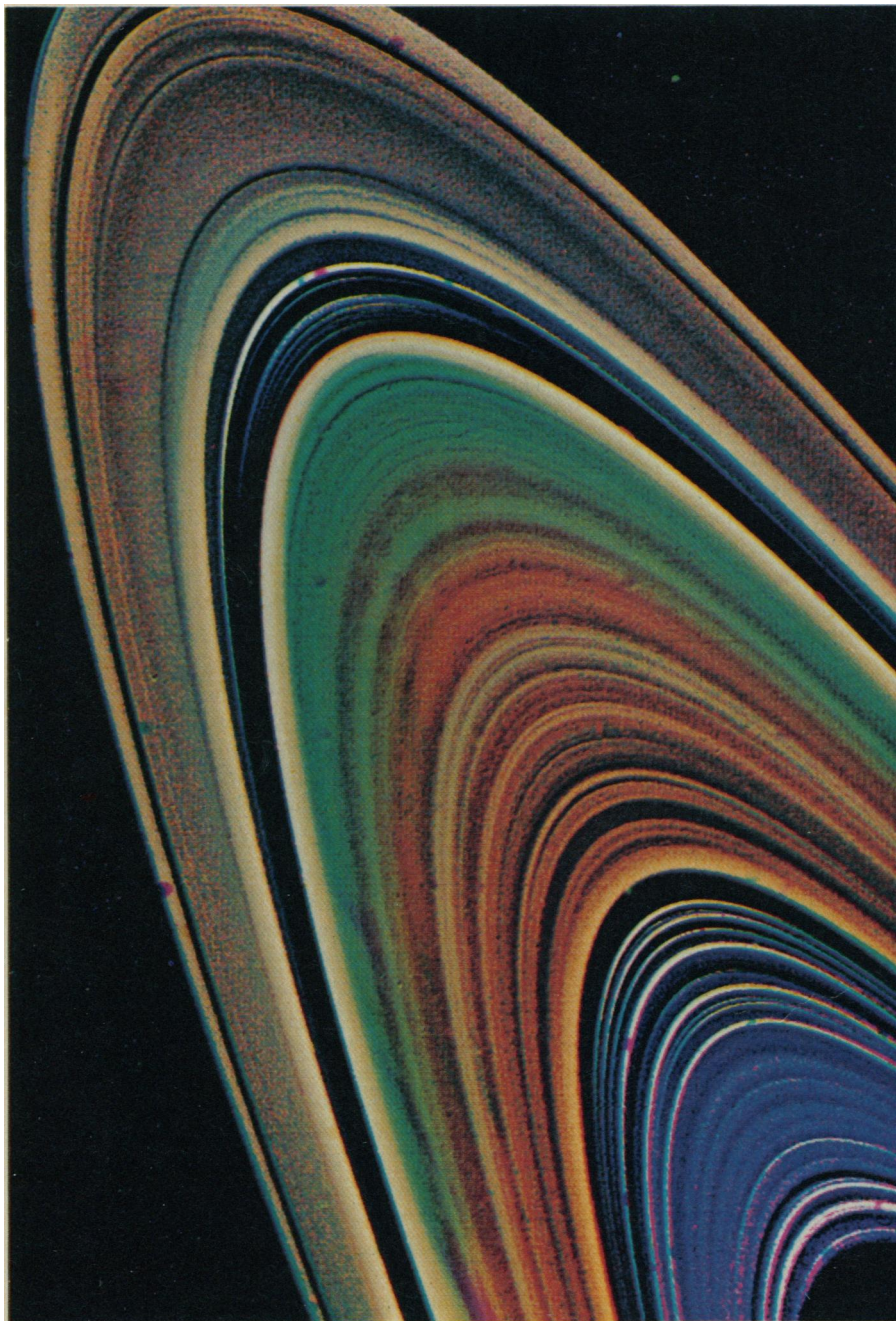


Fig. 32. False color view of Saturn's rings. This highly enhanced color view was assembled from clear, orange, and ultraviolet frames obtained from a range of 8.9 million kilometers. In addition to the previously reported relative blue color of the C ring and Cassini division (4), the picture shows color differences between the inner and outer B ring and between these and the A ring.

that on Iapetus; the rate on Mimas is 20 times that on Iapetus (Table 2). Minor deviations from a monotonic relation between cratering rate and distance from Saturn, shown in Table 2, arise from differences in surface gravity that influence the size of the craters produced. The cratering rates given are the average for each satellite. The variation over the satellite ranges up to 20:1 from leading to trailing hemisphere (4).

If the crater population on Iapetus was produced by an early heavy flux of external objects such as comets, then the relative rates of bombardment of the satellites would have been similar to the relative rates calculated for the present. This is because the variation in cratering rate with increasing distance from Saturn, for virtually any external debris source, is largely controlled by Saturn's gravity rather than initial velocities relative to the Saturnian system.

Scaling the frequency of craters observed on Iapetus to the other satellites, by using the estimated relative rates, yields the results in the last four columns of Table 2. The predicted population density of craters more than 10 km in diameter and of those equal to or larger than satellite radii or diameters are based on a cumulative power function with a slope of -2.2 comet nuclei flux (67). The net cratering estimated for each surface given in the last three columns of Table 2 is that which occurred since the bright cratered terrain of Iapetus was last resurfaced—probably very shortly after the satellites or their parent bodies were formed. From Dione inward, all the satellites were probably struck at least once since that time by a body with enough kinetic energy to produce a crater equal in diameter to the satellite. On the inner satellites this would have occurred many times. As a very rough gauge, an impact that energetic would probably disrupt the satellite. Large satellites would have been disrupted and dispersed at somewhat higher relative impact energies, as they are more strongly bound by their own gravity.

When disrupted and dispersed by collision, the inner satellites of Saturn, which are in nearly circular orbits, would generally have been reassembled by reaccretion of the pieces (4). This is unlikely to have occurred, however, in the case of the satellites in the Lagrange libration regions of Dione and Tethys. Fragments of disrupted Lagrange satellites would be quickly swept up by the primary satellite. This is consistent with the idea, based on their shapes, that the Lagrangians are fragments of larger bodies. They may have been formed at the

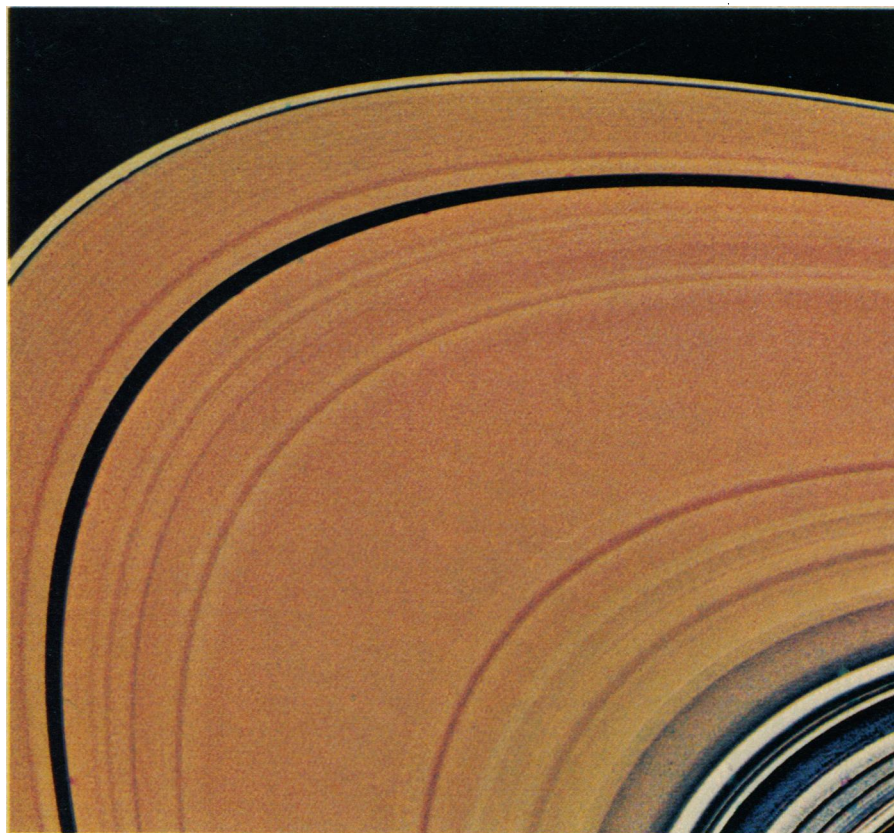


Fig. 33. Saturn's A ring in false color. This view, taken from a range of 2.8 million kilometers, was constructed from green, violet, and ultraviolet frames and processed to enhance subtle color differences between rings. The Cassini division (lower right corner) appears distinctly bluer than the A ring, which is about 15,000 km wide. The inner F ring shepherd satellite (1980S27) is visible near the top of the frame.

time of the last disruption of the coorbiting larger body.

The small satellites near the rings, and possibly the rings themselves, are probably products of a long, complex history of collisional disruption. The coorbital satellites 1980S1 and 1980S3 probably first formed from fragments of a larger parent body that was disrupted early in the period of heavy bombardment. The rings and the small nearby satellites are all conceivably the collisional products of a single parent body.

At the outer edge of the system, the retrograde satellite Phoebe would have had roughly a 50 percent chance of being destroyed, if it had been a member of the system since the time of the last resurfacing of Iapetus. Unlike the interior regular satellites, if Phoebe were disrupted it would not have had time to reaccrete during the history of the solar system, owing to its very small size and extremely large orbit. It is likely, therefore, that Phoebe was captured near or after the time of Iapetus resurfacing.

Thermal evolution and origin. Prior to the Voyager flybys of Jupiter and Saturn, information about the thermal evolution of small bodies was limited to data from the moon and the meteorites and to

inferences from spectrophotometric observations of asteroids. Theoretical studies of the thermal history of small bodies heated only by radiogenic sources of energy suggest that melting and endogenic surface modification should only occur during or just after the cessation of heavy bombardment, as in the case of the moon, or not at all for smaller bodies. For the largest icy satellites of the outer solar system, radiogenic heating models suggested that early melting of the ice was possible, followed by differentiation of the rocky material. Lewis (69) also pointed out that ammonia was a likely constituent in such bodies and that melting could occur at the temperature of the lowest water-ammonia eutectic (170 K). He suggested that evidence for melting in small outer planet satellites might be used to search for objects that had incorporated NH_3 .

Voyager 2 measurements of the mass and radius of Iapetus (51) lead to a mean density of $1.1 \pm 0.1 \text{ g cm}^{-3}$. Densities between 1 and 2 g cm^{-3} suggest mixtures of ice and rock as the most probable composition (4). Dione and Rhea have densities consistent with mixtures that are roughly half ice and half rock, whereas Tethys and Iapetus appear to contain

larger fractions of ice. The densities of all the icy satellites were somewhat lower than expected if they have the same composition as Ganymede and Callisto, even allowing for the effects of self-compression in the Galilean satellites (70) (Fig. 31). A general ice-rich nature is also

suggested by the satellites' high albedos. Except for Enceladus, these satellites all have heavily cratered terrains that are much brighter than the heavily cratered areas on Ganymede and Callisto and even somewhat brighter than the younger grooved terrain on Ganymede. Even if

their collisional evolution resulted in cleaning up their surfaces through re-creation, the last cratering episode that formed their current surfaces apparently contained less non-ice contaminants than on the Galilean satellites.

The Voyager observations of the outer planet satellites have revealed a great diversity of thermal evolution among these bodies: Io is the most volcanically active body known; tiny, icy Enceladus appears to have been resurfaced less than 10^9 years ago; Dione, Rhea, and Tethys all show evidence of significant early resurfacing despite their small size. Two factors are probably responsible for this array of geological activity:

1) Nonradiogenic heat sources. Tidal heating has played a greater role than decay of radioactive nuclides (56) almost certainly for Io and probably for Enceladus. Early high-velocity bombardment may also have been an important source of internal energy for many or most satellites.

2) Composition. The evidence for endogenic activity on the smaller icy satellites suggests that NH_3 or other volatile compounds may be present that result in substantial lowering of the melting point of the mixture of ices in the interior (60). Clathrates may also be present, and their decomposition could lead to gaseous eruptions, in addition to quiescent extrusion of ammonia-water or other solutions.

Information on the composition of Saturn's satellites and rings can be related to models of the early history of the Saturn system (71-73). Three phases may characterize the gravitational contraction history of Saturn: an initial quasi-hydrostatic equilibrium phase, during which Saturn was several hundred times larger than its present size, that lasted 10^4 to 10^5 years (early hydrostatic stage); a hydrodynamic collapse phase during which proto-Saturn shrank to about five times its present size in about 1 year; and another quasi-hydrostatic phase during which Saturn slowly contracted to its present size over the 4.6-billion-year age of the solar system (late hydrostatic stage).

The rings and regular satellites may have formed from a flattened disk of gas and dust that came into being near the end of the hydrodynamic stage, when the outermost portion of proto-Saturn was unable to follow the contraction of the rest due to the proto-planet's very rapid rotation. Temperature conditions in the disk or nebula may have been controlled by Saturn's high intrinsic luminosity at these times, with temperatures declining monotonically with increasing distance

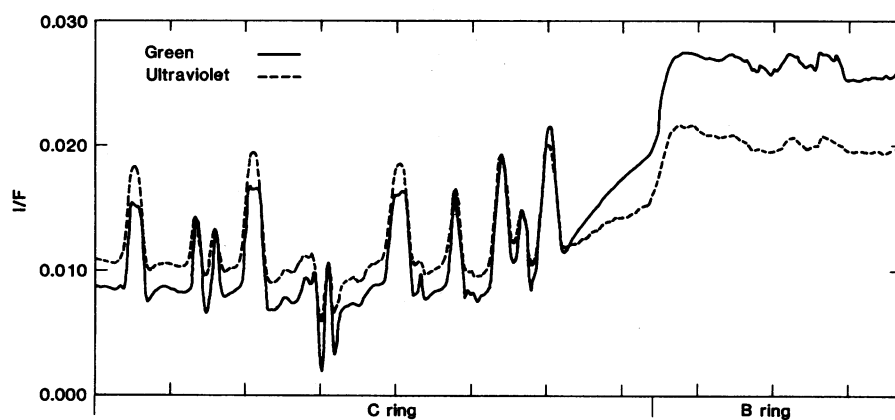
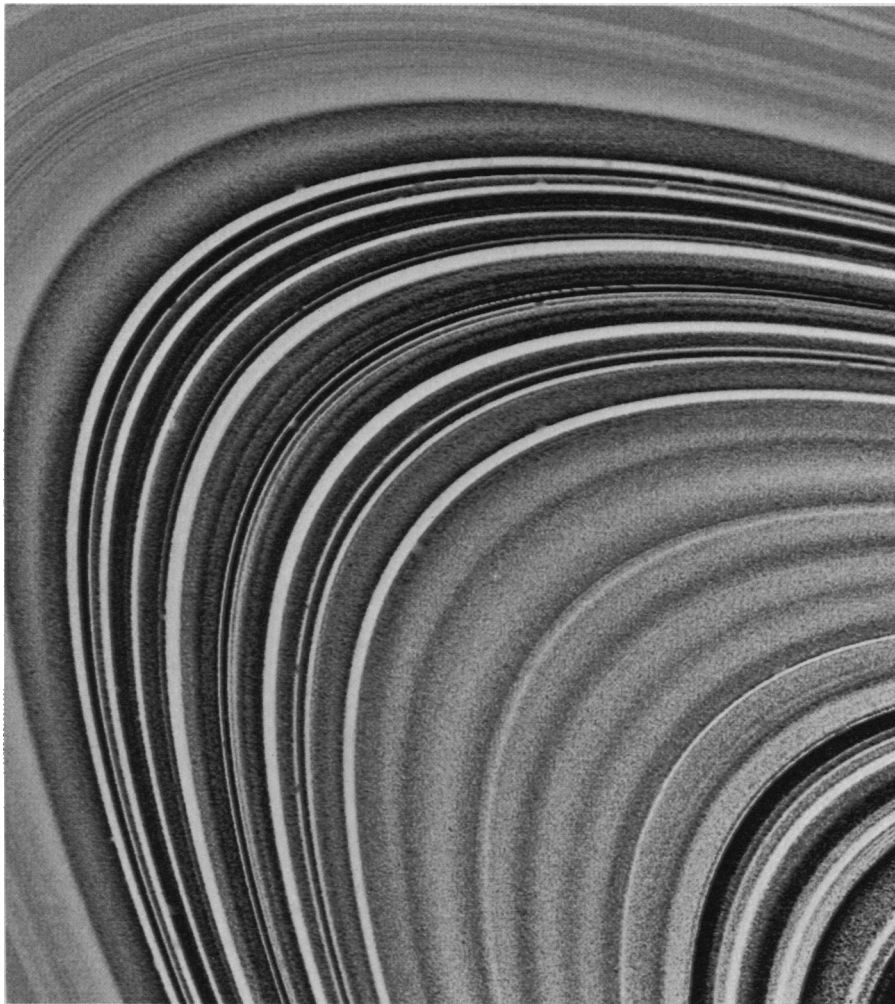


Fig. 34. (Top) False color view of the C ring and inner B ring. Green, clear, and ultraviolet images were used to construct this enhanced view of the C ring recorded from a range of 2.7 million kilometers. A large apparent color difference exists between the C ring (blue) and the inner B ring (yellow), possibly indicating differences in surface composition for the material comprising these two complex structures. This image also reveals three ringlets within the C ring with the same pale yellow color as the B ring. (Bottom) Scan through the boundary of the C and B rings. This scan was made in the radial direction through part of the image above and shows the color differences in green and ultraviolet of features in the outer C ring.

and time (72, 74). These temperatures determine the ability of gases to condense in the nebula and hence the composition of the ring particles and satellites that form by accretion from solid grains. Saturn's intrinsic luminosity may have been about an order of magnitude smaller than Jupiter's at these early times (4). As a result, water ice may have been able to condense during the period of satellite formation at Saturn, while such condensation may have been inhibited close to Jupiter. This conclusion is consistent with the composition of the satellites and rings of Jupiter and Saturn inferred from their mean density, albedo, and other properties (4).

The somewhat colder conditions in the Saturn nebula as compared with the Jupiter nebula permitted ices other than water ice to condense in its outer regions. The occurrence of methane in Titan's atmosphere implies that methane-containing ice may have been incorporated into Titan's interior during satellite formation, with some methane being released into the atmosphere when the interior heated up and outgassed volatiles. It is unlikely that the nebula cooled to 25 to 41 K, the range over which pure methane ice condenses depending on nebular pressure (72, 75, 76); ice was probably methane clathrate ($\text{CH}_4 \cdot 8\text{H}_2\text{O}$), which could form when the temperature fell below about 100 K at Titan's distance. Since at much earlier times the temperature fell below the condensation temperature of water and since some accretionary growth of water ice particles could be expected before methane could form clathrates, methane clathrates were probably a very minor component of the icy part of Titan.

Both ammonia hydrate and pure ammonia ice form at temperatures intermediate between those of water ice and methane clathrate. Thus much of the ammonia in Saturn's nebula may have been able to condense near the orbit of Titan. Through ultraviolet photolysis over the age of the solar system, the gaseous ammonia produced from the ammonia-containing ices in the interior may have helped generate the nitrogen in Titan's atmosphere. For the likely state of oxidation of the Saturn nebula (76), ammonia should be the dominant nitrogen-containing gas. But some molecular nitrogen may have also been present and condensed as a clathrate near the temperature at which methane clathrate forms. This nitrogen clathrate could have been a second source of the nitrogen in Titan's atmosphere.

Ammonia-containing ices would also be expected to form at greater distances

from Saturn, and thus should be an important component of the interiors of Hyperion and Iapetus. In addition, they should be present within some of the satellites interior to Titan, especially those farthest from Saturn. As noted above, the presence of such ices in Enceladus, Tethys, Dione, and Rhea may make it easier to understand the occurrence of internal activity during a portion of their history. Such activity is less likely for Mimas because it is smaller and closer to Saturn, the latter implying that it may lack ammonia-containing ices.

It was pointed out in (4) that there was some tendency for the uncompressed satellite densities to increase outward from Mimas to Titan. With the slight upward revision in the mean density of Tethys and with a question raised about the accuracy of the masses of Mimas and Enceladus determined from ground-based measurements, this trend is less obvious. Analyses of ground-based radio and radar observations indicate that the ring particles are composed almost entirely of water ice, with virtually no silicates (77). If the ring particles are an unfractionated sample of material that condensed in Saturn's nebula during the

period of satellite formation, then a trend of the type suspected does exist. It was suggested in (4) that the innermost bodies of the Saturn system might contain less rock because the planet initially extended into the region they now occupy and so may have kept possession of any silicate-containing grains initially present at these distances. Also, rocky material would have been available to form more distant satellites before the nebula extended into the inner region of the present system.

The low mean density of Iapetus, 1.1 g/cm^{-3} , represents a deviation from any trend of increasing rock content with increasing distance from Saturn. However, it is not markedly different from the density of some of the inner satellites, and can be understood in terms of a mixture of rock and water ice, with the former somewhat below its "solar abundance" value. There is no need to appeal to a large amount of methane ice; indeed, temperatures that are quite low (~ 25 to 41 K) and probably difficult to realize would be needed to permit the condensation of large enough amounts of methane to affect the satellite's mean density.

It was suggested (4) that a stochastic

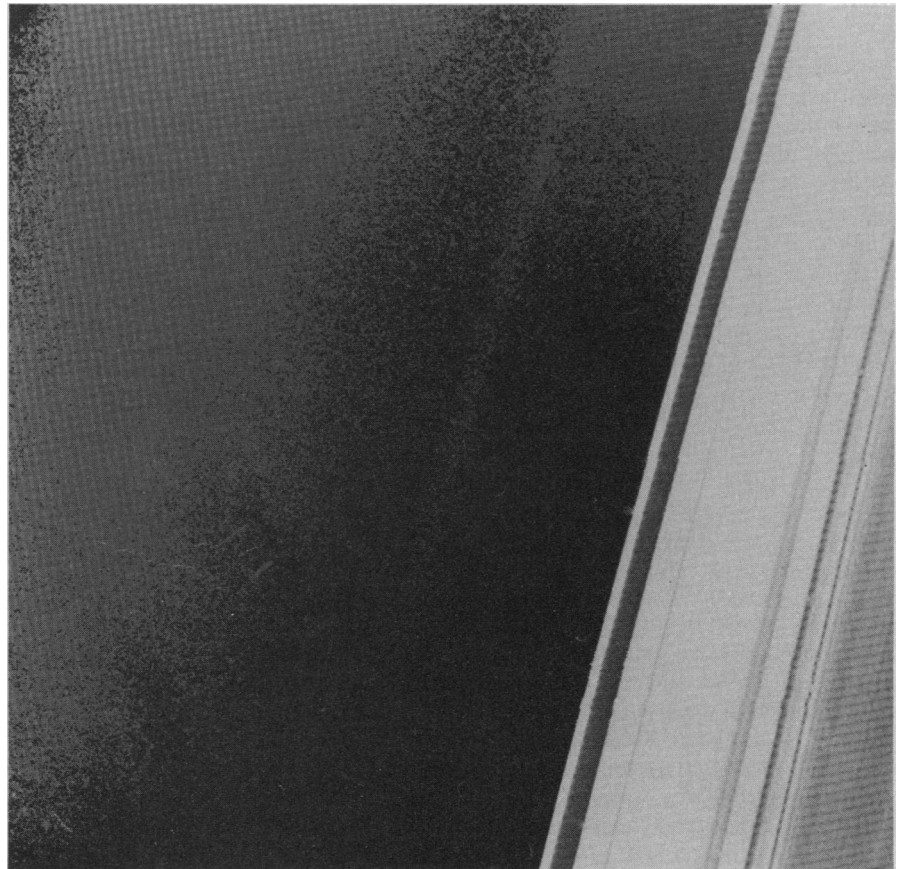


Fig. 35. The G ring, F ring, and edge of the A ring. This long-exposure image shows the faint G ring about 30,000 km outside the outer edge of the A ring in forward-scattered light (phase angle, 160.7°). The broad apparent width of the G ring is due to smear in the image. Smear is also responsible for several star trails visible in the image.

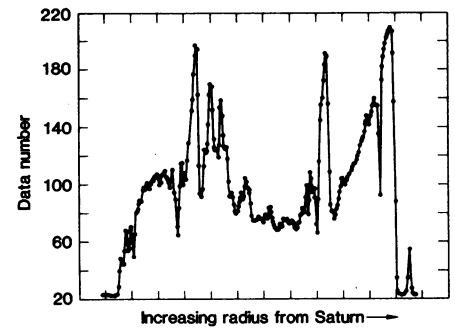


Fig. 36. (Left) Three-color composite (green, clear, violet) of the unilluminated (south) face of the rings. These images were obtained at a range of 3.4 million kilometers and show the A, C, and inner B rings in transmitted solar light. The optically thick outer B ring is illuminated by Saturn-shine and appears brightest at backscattering angles. (Right) Radial scan through the ring in the clear filter. The intensity of transmitted and scattered light is plotted against distance from Saturn.

component is present in the satellites' mean densities and might indicate that the satellites ultimately accreted from a few large planetesimals. This stochastic character is still evident in the density data whether a clear trend exists or not. Another possible explanation of this component is that accretion occurred sequentially. For example, when Titan formed it may have been fed by an accretion zone that included Iapetus' location. But once Titan reached a certain size, gravitational torques may have prevented further accretion, analogous to the way in which "moonlets" may clear gaps in the rings once they reach a certain size (78). Thus, late-condensing ices may have constituted the major source of solid material when Iapetus was finally able to begin forming.

The carbonaceous chondrite characteristic of Phoebe—its low albedo—stands in marked contrast to the composition of the regular satellites and is consistent with a capture origin for Phoebe, as suggested by its retrograde, highly eccentric, and highly inclined orbit. Capture could have occurred as a result of gas drag just before the start of the hydrodynamic collapse (79). The irregular satellites of Jupiter also have photometric properties similar to those of car-

bonaceous chondrites. If the irregular satellites were captured very early in the history of these systems, they may offer a clue to the types of material from which the "heavy element" cores of these planets were constructed (80).

The rings. Voyager 1 (4, 81) revealed the rings to be far more complex than imagined previously, with detail visible down to 100-km resolution or smaller throughout the ring system, from the inner C ring, about 13,000 km above the atmosphere, out to the F ring, a total span of 67,400 km. In addition, Voyager 1 discovered a faint inner D ring, extending to within 7000 km of the planet's atmosphere, and a tenuous G ring 30,000 km beyond the F ring. Even more exciting were the observations of new non-axisymmetric phenomena: the radial "spokes" in the B ring; the presence of several narrow, optically thick, eccentric rings within gaps in the C ring and the Cassini division, and kinks and apparent braids in the multiple strands of the F ring.

In response to these discoveries, substantial revisions were made in the Voyager 2 sequences to increase ring coverage. The Voyager 2 trajectory was more suitable for ring observations, particularly near closest approach, where the

spacecraft was able to view the lit side under favorable geometries. The Voyager 2 imaging sequences included several time-lapse "movies" of the B ring spokes during approach, an extensive search for possible small embedded satellites that seemed likely candidates for clearing ring gaps (77), special efforts to image the rings near the time the spacecraft crossed the ring plane, and a series of high-resolution views of the F ring from above and below, including stereo pairs of frames. Most of these studies were successfully carried out, although seizure of the spacecraft scan platform shortly after ring plane crossing resulted in loss of most of the special F ring observations as well as all the high-resolution images of the dark side of the rings.

In describing the Voyager 2 observations of the rings, we use the classical terminology for A, B, and C rings and for the Cassini division between the A and B rings. We apply the term D ring to the faint structure inside the C ring, and adopt the names F, G, and E for the three rings lying outside the classically known rings. No effort is made to name the thousands of individual ringlets that can be resolved in the high-resolution images; indeed, at scales of tens of

kilometers or less it is probable that the structure is transitory. There has been interest in applying names to a few of the main gaps, and proposals to this effect are under consideration by the International Astronomical Union. The most prominent of these gaps lies about 3000 km inside the outer edge of the A ring and has sometimes been called the Encke division, although it was apparently first clearly seen in 1888 by J. E. Keeler of Lick Observatory (82). Pending a formal decision on gap nomenclature, we will simply call this the A ring gap.

General structure of the rings. The trajectory of Voyager 2 carried the spacecraft much closer to the rings than Voyager 1. In addition, the higher elevation angle of the sun produced brighter rings in the days and weeks before encounter. For 65 hours before closest approach, Voyager 2 observed the lit face of Saturn's rings at higher resolution than attained by Voyager 1. Complete radial coverage was obtained at about 10 km/lp, and selected coverage, at a resolution of a few kilometers per line pair in the wide-angle camera and about 600 m/lp in the narrow-angle camera, was obtained near closest approach. The highest resolution observations were obtained with the aid of image motion compensation. Because the scan platform did not operate for nearly 3 days after ring plane crossing, the highest resolution obtained on the unlit face was only 470 km/lp, taken then with the wide-angle camera.

Figure 32 is an enhanced color composite of the rings made from images obtained in clear, violet, and ultraviolet filters. The resolution is 165 km/lp. The "blueness" of the C ring and the Cassini division is immediately apparent when they are compared with the "redder" or less neutral-colored A and B rings, in agreement with Voyager 1 results (4). With the higher resolution and greater signal-to-noise ratio of the Voyager 2 images, subtle shadings in color are also observed in the A and B rings. The B ring color grades from nearly neutral to more reddish between its outer and inner edges; A ring color seems to vary in the opposite sense. Such subtle differences, which are greatly exaggerated in Fig. 32, may be due to variations in intrinsic particle properties, as we believe is the case for the blueness of the C ring and Cassini division, or merely to differences in scattering phase function, owing perhaps to variations in a complement of tiny particles. Further analysis will be necessary to distinguish between these possibilities.

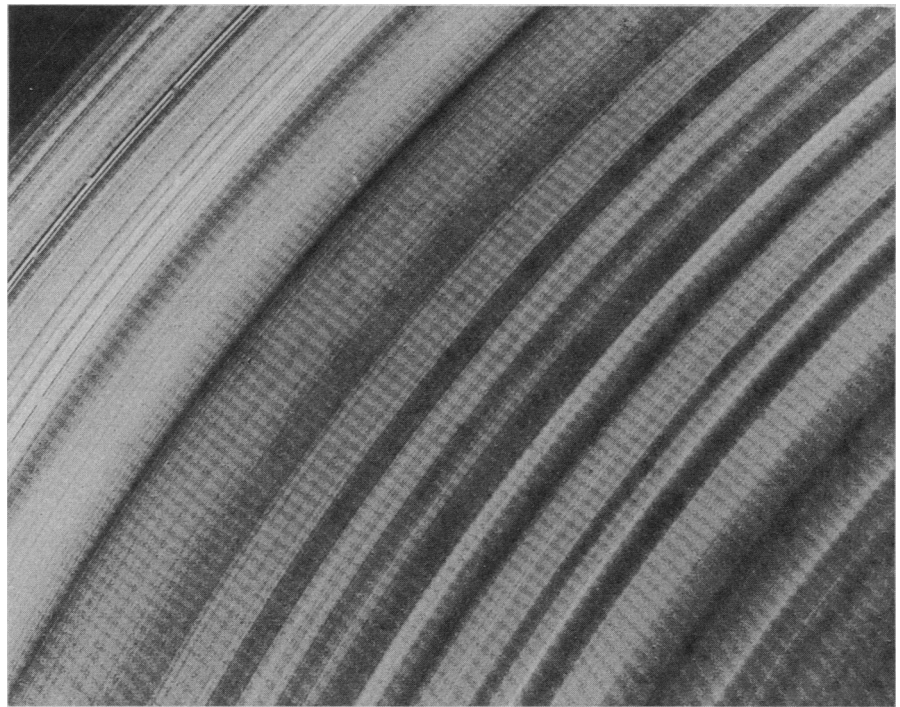


Fig. 37. High-resolution image of outer B ring. This view, taken from a range of 743,000 km, covers about 6000 km of the B ring. Ring structure in this region is composed of features several hundred kilometers wide with 15-km-wide substructure throughout the image. Some of these fine-scale features are believed to be wave phenomena because they have been observed to vary with time and ring longitude.

Voyager 2 was able to extend color coverage to a resolution of about 50 km/lp with nearly complete radial coverage. Figures 33 and 34 show enhanced color composites of the A and C rings, and a line scan through part of the C ring. Of great interest is the existence in both the C ring and the Cassini division of sharply defined color differences. Specifically, two narrow, opaque, eccentric ringlets discovered in these regions by Voyager 1 are significantly different in color from their surroundings; they are more yellow than the relatively neutral C ring and Cassini division material, hence more similar to the A and B ring material. The C ring eccentric ringlet is also slightly darker than the surrounding C ring. Some of this color difference may be due to optical depth; however, other color differences exist between regions of comparable optical depth such as the outer part of the C ring, which is yellowish, and the outer central regions of the C ring, which are less red. Thus both gradual and abrupt color differences exist at a variety of scales in the rings. The maintenance of color differences on such small scales, in the face of continuous erosion and redistribution of ring material, is surely of significance.

Images of the faint G and E rings were obtained by Voyager 2 in forward-scattering geometry. In Fig. 35 the G ring is shown lying about 30,000 km beyond the

F ring. This ring is quite optically thin, with optical depth for conservative scatterers of 10^{-4} to 10^{-5} depending on the phase function of the particles; however, outlying G ring material may have been sufficient to affect the Voyager 2 spacecraft, which passed about 2000 km outside it at ring plane crossing. A Voyager 2 image of the E ring was obtained at a high phase angle ($\sim 166^\circ$). Because this image was obtained at a low elevation angle, enormous foreshortening allows the ring plane to be covered out to very great distances. Any radial concentrations of ring material comparable in optical depth to the E ring (10^{-6} to 10^{-7}) would have been detected well beyond the orbit of Titan. The good agreement of the radial extent of the E ring with ground-based observations (83) gives us confidence that no rings of comparable optical depth exist farther out in the Saturn system.

In spite of the loss of high-resolution observations of the unlit side of the rings, photometric and color information was obtained in abundance at 500-km resolution. Figure 36 shows a wide-angle color composite obtained shortly after observations resumed, and a photometric scan through the image. The high brightness of the outer A ring and inner B ring results from moderate slant optical depth in these regions of bright particles. The other bright regions, in the

outer Cassini division and outer C ring, are brighter than the inner Cassini division and inner C ring by an amount that may not be accounted for by the differences in optical depth alone (4) and indicate brighter particles in these regions. Moderate brightness of the outer B ring shown in the scan is due primarily to "Saturn-shine" on the rings. The large azimuthal variation in the brightness of the B ring seen in Fig. 36 results from preferential backscattering of illumination on the rings from the bright lit face of Saturn. Further analysis of this variation will be useful in constraining ring particle scattering behavior.

Little information was previously available on the structure of the B ring at high resolution, as the best Voyager 1 images had only 70 km/lp resolution on

its lit face and its unlit face was too dark for meaningful observations by Voyager 1. Features seen by Voyager 1 at 100-km resolution were everywhere resolved by Voyager 2 into further fine-scale ringlets, down to the limit of resolution of 10 km/lp (Fig. 37).

Several wavelike features were observed by Voyager 2. The wavelike patterns in the A ring gap vicinity (4) were observed with improved sensitivity and resolution from the lit face; some of these features appear to exhibit azimuthal asymmetry as well. Similar wavelike features were observed in the outer A ring near closest approach. None of these patterns has yet been satisfactorily explained. The wavelike pattern observed in the outer Cassini division by Voyager 1 (84) was observed only very

faintly by Voyager 2; a combination of unexpectedly extreme darkening of the region due to particle scattering properties and loss of several important unlit face observations prevented immediate detection of these features. However, further processing is under way.

Resonances. Gravitational resonances must play a role in driving the rings, as we will show from the observed 2:1 resonance with Mimas of the outer edge of ring B. The tentative list of resonances and suggested correlations for early Voyager 1 observations offered by Collins *et al.* (81) must be considered out of date, if only because of a more recent search by Franklin and Cook (85) for possible resonances with Saturn's figure. Five such resonances are tentatively suggested along with the possibility that the structure within Cassini's division may be affected on a coarse scale (seven such resonances). Franklin and Cook quote a suggestion by R. Smoluchowski that these harmonics could be generated by deep-seated meteorological activity associated with a helium phase change interacting with Saturn's core of metallic hydrogen. In that case the phases and amplitudes would be variable and so would any associated structure in the rings.

Asymmetric ring features. Several different kinds of asymmetric ring features were found in the Voyager 2 images. Several asymmetries can be seen in Fig. 38, which compares four images of the outer B ring and inner Cassini division taken on both ansae over a period of about 6 hours. Two images were taken on the west ansa and two on the east ansa. These images were scaled independently of each other and then registered in order to match up most of the large features in the Cassini division. This procedure assumes that the Cassini division features are not all eccentric by the same amount and locked in phase over a distance > 3000 km. The fine structure in the B ring is found to be highly variable when comparisons are made between opposite ansae or between observations of a single ansa during several hours. Features with radial widths of about 500 km remain correlated, but there is no systematic correlation of the 20-km-wide features. If the B ring fine structure actually reflects wave phenomena or diffusion instabilities (86), these phenomena are probably driven by many different sources with different forcing periods which give rise to the apparently chaotic and uncorrelated morphology.

Also evident in Fig. 38 are large variations in the width of the gap just outside the outer edge of the B ring. The inner

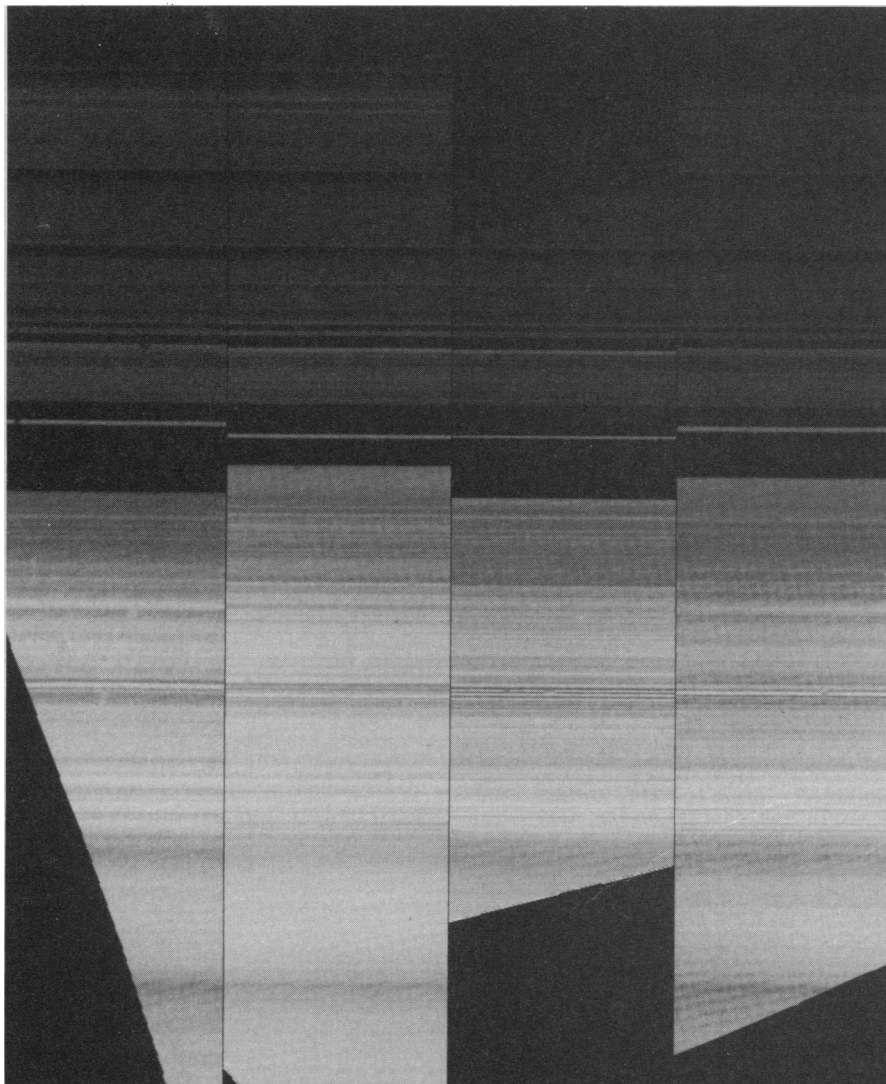


Fig. 38. Four radial slices through the Cassini division (top) and outer B ring (bottom). The middle two slices were taken from high-resolution (< 15 km/lp) images of the east ansa and the outer two slices from the west ansa. Variations of up to 140 km can be seen in the width of the gap separating the B ring from the Cassini division. These variations are believed to be caused by the 2:1 resonance of ring material with Mimas. Also apparent are variations in fine structure in the B ring and the presence of an eccentric ringlet within the variable width gap. All slices were taken within about 7 hours. [Digital processing for this comparison was performed by G. W. Garneau, JPL Image Processing Laboratory]

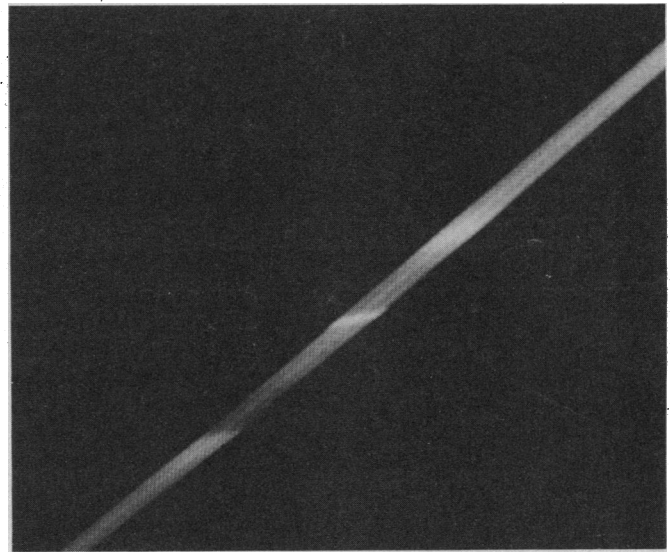
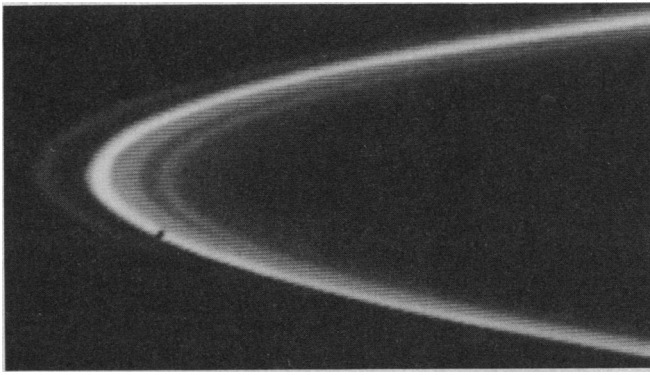


Fig. 39 (left). Nearly edge-on view of the F ring. This image was taken just after ring plane crossing from a range of 103,000 km. At least four faint components are visible separated from one main bright component. The strands have a total radial extent of about 500 km and do not appear to interact in the 25° of orbital longitude visible in this image.

Fig. 40 (right). Detail of the main bright component of the F ring. This wide-angle image was recorded from a range of 55,000 km and shows three images of the F ring caused by spacecraft motion during the exposure. Several bright clumps are visible within the ring. The center clump has sharply defined edges and may be an individual large particle orbiting in the ring. Other, less sharply defined clumps may be local concentrations of smaller ring particles.

edge of this feature varies in radial position by over 140 km on time scales of several hours. This effect was also seen in the sequence of images taken for a spoke movie, which cover this region continuously for about 16 hours. Analysis of these data showed that the B ring edge is not simply eccentric, but has two maxima and two minima, as if the ellipse describing its edge were displaced so that the planet lies at the center of the ellipse instead of a focus. Furthermore, the radial minima of the ellipse follow the motion of Mimas. This behavior strongly suggests distortion of streamline orbits of ring particles by the classical Mimas 2:1 resonance. It has long been known that the outer edge of the B ring is near this resonance and probably related to it in some way. The larger than expected amplitude and the phase of the B ring radial asymmetry suggest that the Mimas 2:1 resonance is essentially coincident with the outer edge of the B ring.

An eccentric ringlet is also shown in Fig. 38 which was found by Voyager 1 in the inner Cassini division gap. This ringlet precesses under the influence of Saturn's oblateness and does not appear to be directly tied to an external resonance. The radial position of this feature varies by at least 40 km, with the ringlet being slightly wider at its greatest radius. This is the same as the behavior of the other eccentric ringlets found in the C ring at about $1.44 R_S$ (4) and $1.25 R_S$. The last feature is close to the expected position of the Titan apsidal resonance. Ring particle orbits at this radius will precess at the same angular rate as Titan's orbital rate of 17.8 deg/day .

Kinky rings. Voyager 1 showed the F ring to be composed of at least three

separate components, the outer two displaying a kinked and twisted appearance (4). To better understand these phenomena, several regions were selected in the F ring for repeated observations at a resolution high enough to resolve the separate components. The areas near the shepherding satellites (1980S26 and 1980S27) were chosen in order to look for changes in the ring after the close passage of these objects. Another region selected was the part of the F ring that was between the shepherds at the time of their conjunction, about 10 days before encounter. Two other regions were chosen at different orbital longitudes in order to cover other parts of the ring and to have a convenient place where the spacecraft could perform an image motion compensation maneuver, to allow subkilometer resolution of a small part of the F ring.

Voyager 2 found the same clumpy and occasionally kinked appearance of the F ring, but surprisingly found only one small region where the rings appeared twisted or braided. Evidently, the twisted appearance of the F ring is either a time-variable phenomenon (possibly modulated by the precession of the eccentricities of the ring and shepherds) or one that occurs over a restricted region of the ring. In total, Voyager 2 imaged

about 15 percent of the F ring with a resolution high enough to see any twisted appearance. The highest resolution showed at least five separate components within the F ring. Figure 39 shows a wide-angle view of the F ring, taken shortly after ring plane crossing, that covers about 20° near 1980S26. With a resolution of about 15 km/lp, one bright and four faint components can be seen. Individual concentrations within these components have also been detected (Fig. 40) and may be responsible for the multiple structure of the ring. Perturbations of large ring particles by the shepherding satellites will take much longer

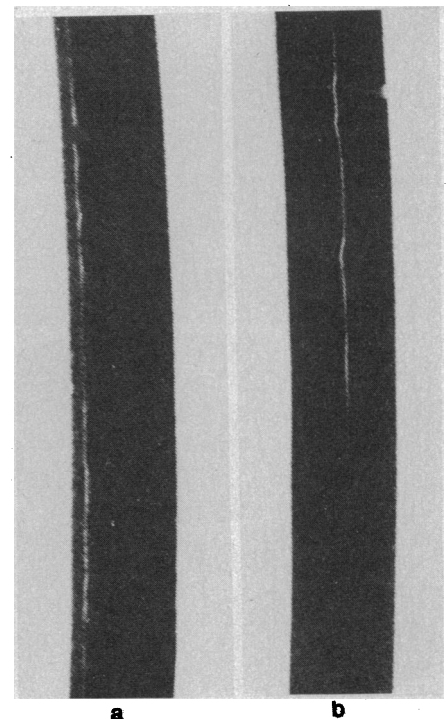


Fig. 41. Two views of the wide A ring gap at $2.21 R_S$, showing two kinky and discontinuous-appearing ringlets within the 325-km-wide gap. In (a) the ringlet is 50 km from the inner edge of the gap, while in (b) it is about 170 km from the inner edge. Two separate rings were seen by Voyager 1 at the same orbital longitude, indicating that the features are two separate discontinuous rings and not one eccentric feature.

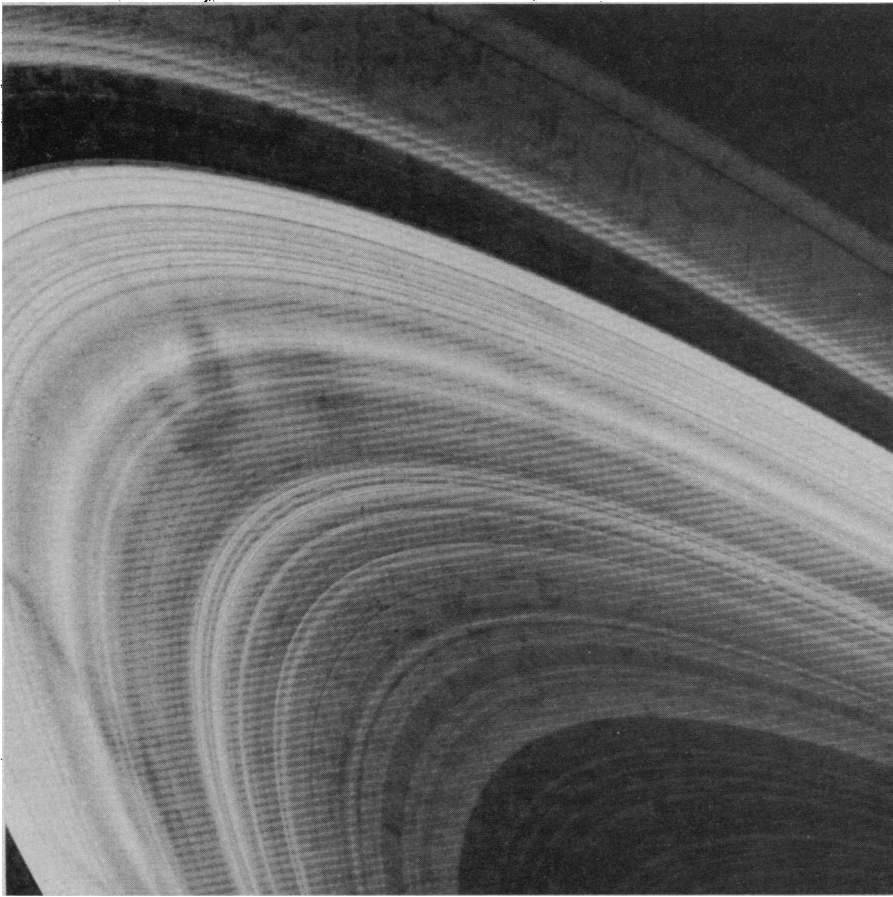
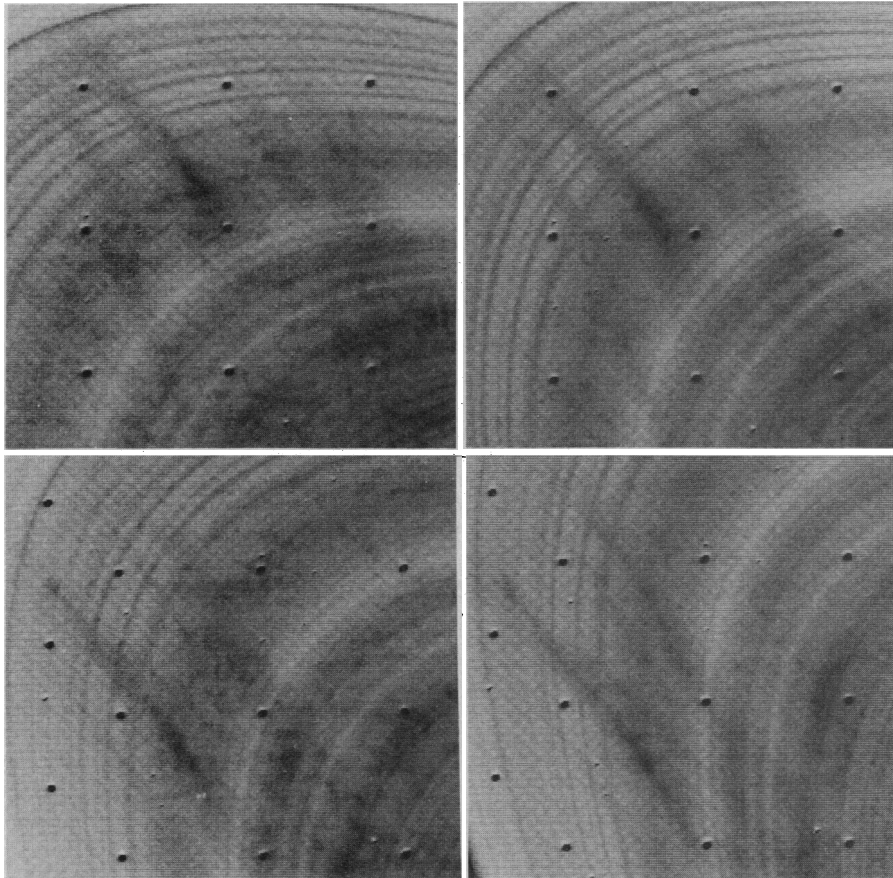


Fig. 42. Image of spokes in the B ring. This image is one frame from a 14-hour-long sequence of narrow-angle images of the B ring. The sequence started at a range of 4 million kilometers and repeated every 5 minutes. A variety of spokes can be seen with varying tilts and widths. The Cassini division is visible at the top and the outer C ring at the lower right.



to damp out than those of smaller particles. Goldreich (87) has suggested that the motions of large particles within the F ring could induce the twisted and clumped morphology observed by Voyager 1.

The clumps in the F ring were observed from about 4 weeks before encounter through closest approach, and then about 3 days after encounter, when the spacecraft scan platform was re-pointed to Saturn. Clumps could be tracked and were recognizable over periods of at least 15 orbits. No apparent variation was found in the longitudinal distribution of clumps. They appear to be fairly uniformly distributed around the ring at intervals of 5000 to 13,000 km (typically about 9000 km). A similar spacing of about 7000 km was observed on Voyager 1, but erroneously reported as 700 km (4). This spacing is comparable to the relative motion of the F ring particles with respect to the shepherding satellites over one orbital period. During this time ring particles will experience a pulse in the gravitational pull from the satellites because of the relative eccentricities between the ring and satellites.

High-resolution images (10 km/lp) of the major A ring gap at about $2.21 R_S$ reveal two apparently discontinuous rings inside the division. Both rings, shown in Fig. 41, appear to vary with longitude in optical depth; they fade in and out and have not been observed together on a single Voyager 2 image. From the Voyager 2 observations it is not clear whether there are two separate rings or one eccentric ring; however, the existence of two rings was established by Voyager 1, which clearly imaged both rings at different radii from Saturn at the same orbital longitude. The clumpiness of these rings can also be observed to orbit as a pattern over times of several minutes and at the orbital period of the rings at that radius. One ring is about 50 km from the inner edge of the 325-km-wide gap and appears to vary in brightness with a length scale of about 3000 km. There are other regions where this ring is not visible for distances over 20,000 km while the other ring is clearly visible. The other ring is found very near the center of the division and also varies in brightness over distances of about

Fig. 43. Sequence of images showing spoke formation. These four images are close-ups of a pattern of spokes in a time sequence from upper left to lower right. Time separations between adjacent frames are 10, 15, and 10 minutes, respectively. In a relatively clear region in the center of the pattern of spokes in the first frame a new spoke appears in the second and third and becomes more conspicuous in the last frame.

3000 km. This ring was found to have a kinked morphology when observed at the highest resolution. The kinks are tens of kilometers in amplitude and about 1000 km apart. It has been shown (88) that similar kinked morphologies can be induced from perturbations by eccentric satellites orbiting very close to a ring. No objects except the clumps in the rings have been found orbiting inside the A ring gap, but because of our restricted sampling of longitudes we cannot put strong observational limits on the existence or sizes of such bodies.

Ring spokes. The radial features or spokes discovered in the B ring have proved to be among the most interesting features in the ring system (4, 81). They appear dark in backscattering and bright in forward-scattering illumination conditions. Spokes were apparent in the rings as soon as Voyager 2 began the observatory phase 82 days before encounter, when the narrow-angle camera resolution was approximately 2000 km/lp. A longer time was afforded for observing the spokes than was available on Voyager 1.

Most of the spokes are confined to the central B ring with an inner boundary at $1.72 \pm 0.01 R_S$ (103,900 km) and an outer boundary at approximately the outer edge of the B ring. Figure 42 shows a typical spoke pattern in the B ring. Spokes can be generally classified as (i) radial or having radial components and (ii) nonradial. It has been suggested that spokes form radially in a reference frame rotating with a period close to the corotational rate of Saturn's magnetic field and then follow the differential orbital motion of the individual ring particles (89). In this model, spokes in the process of formation will have radial components, and the leading and trailing edges of forming spokes should have different periods. Precise rotational velocities of the various portions of spokes have been measured from Voyager 2 images at the JPL Image Processing Laboratory with the same software used for atmospheric feature tracking on Jupiter and Saturn. Features are compared in two or more images with time separations of 10 to 20 minutes. In several cases where radial spoke edges were observed, the leading and trailing edges show distinctly different angular rotational rates. Furthermore, the older or more tilted edges have a Keplerian rate, while the younger or radial edges are closer to the corotational rate of the magnetosphere.

Spokes have been observed in the process of formation in the B ring (Fig. 43). In particular, a new radial spoke appeared in the middle of an existing pattern in a long sequence of pictures

Fig. 44. Spokes as seen from the dark side of the rings. This image is an enhanced version of the clear-filter frame used in Fig. 36. The image has been filtered to show the low-contrast spokes in the outer half of the B ring. The spokes appear bright because they are illuminated by forward-scattered light reflected off Saturn's disk.



taken 5 minutes apart. The spoke did not appear at all in one image, was very faint in the next, and then was clearly visible in every image thereafter. The time scale for formation of the 6000-km feature appears to be at least as short as 5 minutes.

As in the Voyager 1 data, the Voyager 2 images reveal the spokes more easily on the morning ansa (just rotated out of Saturn's shadow). Some spokes can be tracked as they rotate through 360° or more; however, it is not clear whether we really see the identical spoke pattern or a new one that is "reprinted" on top of the old one. If spokes are created as radial features, then mapping their orbital motion backward in time should allow a determination of the point of origin. Spokes mapped backward in this way were found not to have a common orbital longitude of creation. Places of origin also appear unrelated to the shadow of the planet on the rings, although a few spokes appear to have formed within the shadow.

After Voyager 2 passed through the ring plane, the image shown in Fig. 44 was taken of the unilluminated side of the rings, showing spokes for the first time with this viewing perspective. In this image the B ring is illuminated predominantly by sunlight scattered off Saturn's atmosphere and appears brightest in backscattered light. Bright spokes are visible in the region with Saturn-shine phase angles of about 80° to 120° . The fact that these features are only seen in

this region of favorable Saturn illumination indicates that they are dark-side phenomena and not bright-side spokes shining through optically thin parts of the B ring. The shapes seen on the dark side indicate a morphological behavior similar to that observed on the illuminated side, with spokes tilting away from the radial direction in the sense of the Keplerian motion of ring particles. Furthermore, dark-side spokes are not tilted enough to be created on the illuminated side and then passed through the ring plane a quarter of an orbit later. The conclusions that these features may be created on the dark side of the B ring while others form in Saturn's shadow have implications for the mechanism of spoke formation, casting some doubt on the idea that charging of small ring particles by photoionization alone is responsible for levitating them out of the ring plane.

Embedded moonlets. Following the discovery by Voyager 1 of radial structure in the rings, several hypotheses emerged to explain the different types of structure. Several variants of instability or "clumping" mechanisms were suggested (86), as well as the effects of small, embedded moonlets (77, 78). The moonlet hypotheses offered the possibility of understanding both the many narrow features in optically thick regions and the broad, clear gaps in optically thin regions. Because of the importance of the existence or nonexistence of objects with radii as large as 10 to 15 km for

theories of ring origin, Voyager 2 observations of one optimal ring region, the Cassini division, were carefully analyzed. The region contains two empty gaps ~ 250 and ~ 450 km wide which, if cleared by moonlets, would indicate moonlet diameters of 20 to 30 km respectively (77). The region was observed nearly continuously for about 16 hours, longer than a local orbital period, at a resolution of about 80 km/lp. The sequential images of the Cassini gap were reprojected as linear swaths and stacked vertically, with each successive swath shifted horizontally to compensate for Keplerian motion, so that any moonlet present in succeeding photos would line up vertically. The data were filtered to enhance the appearance of unresolved point sources with respect to background noise. By using simulations, it was ascertained that a point source with a signal as low as two to four times the mean noise level would be visible in such a display. Almost 340° coverage of both gaps in the Cassini division was obtained, and no moonlets were detected.

This negative result is a significant constraint on the size of any moonlet embedded within either gap. The limiting size is a function of geometric albedo. Satellites 1980S1, 1980S3, and 1980S28 have albedos of ~ 0.3 at this phase angle. If the albedo of a ring moonlet were as high as 0.3, our observations would rule out moonlets as large as 6 km in diameter in the Cassini gaps; if it were as low as 0.1, only moonlets as large as 10 km in diameter would be ruled out.

Whether a moonlet smaller than the limiting sizes above could clear the Cassini gaps depends on the density of the moonlet and the ring thickness, which is characterized by particle dispersion velocity (77). For values of this velocity as large as 0.5 cm sec^{-1} , obtained by associating observed viscosity with particle collisions (84), the gaps would require a moonlet of density 1.3 g cm^{-3} with a 20-km diameter. Even with particle dispersion velocities at their absolute lower limit, given by the condition of minimal stability to gravitational disturbances, such a moonlet would have to be at least 5 km in diameter. Therefore, a combination of unusually (but not impossibly) low-surface albedo and the lowest possible particle random velocities would be required for the Cassini gaps to be cleared by solitary moonlets. The 350-km-wide A ring gap remains a possible location for several moonlets 10 to 20 km in diameter; the kinky ringlets in this gap may be a clue to the presence of moonlets there. However, neither the A ring gap nor the 250-km-wide "eccentric

ring" gap in the outer C ring at $1.44 R_S$ was observed sufficiently to establish limits on the sizes of possible moonlets there.

BRADFORD A. SMITH

Department of Planetary Sciences,
University of Arizona, Tucson 85721

LAURENCE SODERBLOM

RAYMOND BATSON

PATRICIA BRIDGES

JAY INGE

HAROLD MASURSKY

EUGENE SHOEMAKER

U.S. Geological Survey,
Flagstaff, Arizona 86001

RETA BEEBE

Department of Astronomy,
New Mexico State University,
Las Cruces 88003

JOSEPH BOYCE

GEOFFREY BRIGGS

NASA Headquarters,
Washington, D.C. 20546

ANNE BUNKER

STEWART A. COLLINS

CANDICE J. HANSEN

TORRENCE V. JOHNSON

JIM L. MITCHELL

RICHARD J. TERRILE

Jet Propulsion Laboratory,
Pasadena, California 91109

ALLAN F. COOK II

Center for Astrophysics,
Cambridge, Massachusetts 02138

JEFFREY CUZZI

JAMES B. POLLACK

NASA/Ames Research Center,
Moffett Field, California 94035

G. EDWARD DANIELSON

ANDREW P. INGERSOLL

Division of Geological and Planetary
Sciences, California Institute of
Technology, Pasadena 91125

MERTON E. DAVIES

Rand Corporation,
Santa Monica, California 90406

GARRY E. HUNT

University College London,
London WC1E 6BT, England

DAVID MORRISON

Institute for Astronomy,
University of Hawaii, Honolulu 96822

TOBIAS OWEN

Department of Earth and Space
Sciences, State University of
New York, Stony Brook 11790

CARL SAGAN

JOSEPH VEVERKA

Cornell University,
Ithaca, New York 14853

ROBERT STROM

Lunar and Planetary Laboratory,
University of Arizona, Tucson 85721

VERNER E. SUOMI

University of Wisconsin,
Madison 53706

1. B. A. Smith *et al.*, *Science* **204**, 951 (1979); B. A. Smith *et al.*, *ibid.* **206**, 927 (1979).
2. A. P. Ingersoll, R. F. Beebe, J. L. Mitchell, G. W. Garneau, G. M. Yagi, J. P. Muller, *J. Geophys. Res.* **86**, 8733 (1981).
3. J. L. Mitchell, R. F. Beebe, A. P. Ingersoll, G. W. Garneau, *ibid.*, p. 8751.
4. B. A. Smith *et al.*, *Science* **212**, 163 (1981).
5. M. D. Desch and M. L. Kaiser, *Geophys. Res. Lett.* **8**, 253 (1981).
6. G. M. Yagi, J. J. Lorre, P. L. Jepsen, in *Proceedings of a Conference on the Atmospheric Environment of Aerospace Systems and Applied Meteorology* (American Meteorological Society, Boston, 1978), pp. 110-117.
7. B. A. Smith *et al.*, *Space Sci. Rev.* **21**, 103 (1977).
8. G. E. Hunt *et al.*, *Philos. Trans. R. Soc. London*, in press; G. C. Chatters and V. E. Suomi, *IEEE Trans. Geosci. Electron.* **GE-13**, 137 (1975).
9. J. R. Holton, *An Introduction to Dynamic Meteorology* (Academic Press, New York, ed. 2, 1979), pp. 68-71.
10. S. J. Weidenschilling and J. S. Lewis, *Icarus* **20**, 465 (1973); A. P. Ingersoll, *Space Sci. Rev.* **18**, 603 (1976); in *The New Solar System*, J. K. Beatty, B. O'Leary, A. Chaikin, Eds. (Sky, Cambridge, Mass., and Cambridge Univ. Press, 1981), pp. 117-128.
11. R. Hanel *et al.*, *Science* **212**, 192 (1981).
12. R. Hanel *et al.*, *ibid.* **215**, 544 (1982).
13. R. G. Prinn and T. Owen, in *Jupiter*, T. Gehrels, Ed. (Univ. of Arizona Press, Tucson, 1976), pp. 319-371.
14. S. L. Hess and H. A. Panofsky, in *Compendium of Meteorology*, T. F. Malone, Ed. (American Meteorological Society, Boston, 1951), p. 391; A. P. Ingersoll and J. N. Cuzzi, *J. Atmos. Sci.* **26**, 981 (1969); A. Barcilon and P. J. Gierasch, *ibid.* **27**, 550 (1970).
15. G. P. Williams, *J. Atmos. Sci.* **35**, 1399 (1978); *ibid.* **36**, 932 (1979).
16. F. H. Busse, *Icarus* **29**, 255 (1976).
17. V. N. Zharkov and V. P. Trubitsyn, in *Jupiter*, T. Gehrels, Ed. (Univ. of Arizona Press, Tucson, 1976), p. 133; D. J. Stevenson and E. E. Salpeter, in *ibid.*, p. 85.
18. G. E. Hunt, D. Godfrey, J. P. Muller, R. F. T. Barrey, *Nature (London)*, in press.
19. T. Maxworthy and L. G. Redekopp, *Icarus* **29**, 261 (1976).
20. A. P. Ingersoll and P. G. Cuong, *J. Atmos. Sci.*, in press.
21. R. Suggs and R. Beebe, in preparation.
22. A. P. Ingersoll *et al.*, *Nature (London)* **280**, 773 (1979).
23. G. L. Tyler *et al.*, *Science* **212**, 201 (1981).
24. R. E. Samuelson *et al.*, *Nature (London)* **292**, 688 (1981).
25. W. C. Maguire *et al.*, *ibid.*, p. 683.
26. V. G. Kunde *et al.*, *ibid.*, p. 686.
27. D. Strobel, *Geophys. Res. Lett.*, in press.
28. O. B. Toon, R. P. Turco, J. B. Pollack, *Icarus* **43**, 260 (1980); C. Sagan, *Space Sci. Rev.* **11**, 73 (1981); *Icarus* **18**, 649 (1973); B. N. Khare and C. Sagan, *ibid.* **20**, 311 (1973).
29. G. F. Lindal, H. B. Hotz, D. N. Sweetnam, V. R. Eshelman, G. L. Tyler, *Bull. Am. Astron. Soc.* **13**, 700 (1981).
30. The location of the peak brightness of the main haze layer is probably determined by the photometric function of the aerosols and therefore does not necessarily refer to the altitude of peak number density.
31. P. Smith, *J. Geophys. Res.* **85**, 5943 (1980).
32. J. L. Elliot *et al.*, *Icarus* **26**, 387 (1975).
33. The Minnaert law postulates the following relationship between observed brightness, I , and the cosines of the angles of incidence and reflection, μ_0 and μ : $I = I_0 (\mu_0 \mu)^k$, where I_0 and k are constants. We set k equal to 0.887 and found I_0 , the "normal albedo."
34. L. A. Sromovsky *et al.*, *Nature (London)* **292**, 698 (1981).
35. If Titan's axis of rotation is perpendicular to its orbital plane and thus parallel to Saturn's axis, it would have an obliquity of about 27° and Titan would experience slightly larger fractional seasonal variations of isolation than does the earth. The length of a Titan year is $29\frac{1}{2}$ earth years.
36. G. W. Lockwood and D. T. Thompson, *Nature (London)* **280**, 43 (1979).
37. According to G. W. Lockwood, his final values for the brightness of Titan during the last 2 years are in excellent agreement with the preliminary values used in (12).
38. J. B. Pollack *et al.*, *Geophys. Res. Lett.* **7**, 829 (1980).
39. J. B. Pollack and J. N. Cuzzi, *J. Atmos. Sci.* **37**, 868 (1980).

40. K. Rages and J. B. Pollack, *Icarus* 41, 119 (1980).
41. M. Tomasko, *J. Geophys. Res.* 85, 5937 (1980).
42. A. L. Lane et al., *Science* 215, 537 (1982).
43. D. Strobel, *Planet. Space Sci.*, in press.
44. W. R. Ward, *Icarus* 46, 97 (1981).
45. J. A. Van Allen, M. F. Thomsen, B. A. Randall, R. L. Rairden, C. L. Grosskreutz, *Science* 207, 415 (1980); J. A. Simpson et al., *J. Geophys. Res.* 85, 5731 (1980).
46. *Int. Astron. Union Circ.* 3457 (6 March 1980).
47. *Ibid.*, No. 3466 (10 April 1980).
48. *Ibid.*, No. 3496 (31 July 1980).
49. E. C. Stone, *Nature (London)* 292, 675 (1981).
50. ——— and E. D. Miner, *Science* 215, 499 (1982).
51. G. L. Tyler et al., *ibid.*, p. 553.
52. Y. Kozai, *Publ. Astron. Soc. Jpn.* 28, 675 (1976).
53. D. P. Cruikshank, *Rev. Geophys. Space Phys.* 79, 165 (1979); R. N. Clark and P. D. Obensby, in preparation; U. Fink et al., *Astrophys. J. Lett.* 207, 63 (1976).
54. G. E. Danielson et al., *J. Geophys. Res.* 86, 8683 (1981).
55. A. Dollfus, *Astronomie* 6, 2534 (1968); J. W. Fountain and S. M. Larson, *Icarus* 36, 92 (1978).
56. C. F. Yoder, *Nature (London)* 279, 767 (1979).
57. S. J. Peale, P. Cassen, R. T. Reynolds, *Science* 203, 892 (1979).
58. C. Yoder, *Eos*, in press.
59. A. F. Cook and R. J. Terrile, in preparation.
60. D. L. Stevenson and A. Anderson, *Eos*, in press.
61. D. P. Cruikshank and R. H. Brown, *Icarus*, in press.
62. S. Soter, paper presented at the IAU Planetary Satellite Conference, Cornell University, Ithaca, N.Y., 1974.
63. D. P. Cruikshank, in preparation.
64. A. F. Cook and F. A. Franklin, *Icarus* 13, 282 (1970).
65. J. Degewij, J. Gradie, B. Zellner, *Bull. Am. Astron. Soc.* 9, 503 (1977).
66. E. M. Shoemaker, in *The New Solar System*, J. K. Beatty, B. O'Leary, A. Chaikin, Eds. (Sky, Cambridge, Mass., and Cambridge Univ. Press, 1981), pp. 117–128; E. M. Shoemaker and R. F. Wolfe, *Lunar Planet. Sci.* 12 (Suppl. A), 1 (1981).
67. E. M. Shoemaker and R. F. Wolfe, in *The Satellites of Jupiter*, D. Morrison, Ed. (Univ. of Arizona Press, Tucson, in press).
68. J. H. Oort, *Bull. Astron. Inst. Neth.* 2, 91 (1950); P. R. Weissman, in *Comets, Asteroids, Meteorites*, A. H. Delsemme, Ed. (Univ. of Toledo Press, Toledo, Ohio, 1977), pp. 87–91.
69. J. S. Lewis, *Science* 172, 1127 (1971); *Sci. Am.* 230 (No. 3), 50 (1974); *Space Sci. Rev.* 14, 401 (1973).
70. M. J. Lupo and J. S. Lewis, *Icarus* 40, 157 (1979).
71. A. S. Grossman, J. B. Pollack, R. T. Reynolds, A. L. Summers, H. C. Graboske, Jr., *ibid.* 42, 358 (1980).
72. J. B. Pollack, A. S. Grossman, R. Moore, H. C. Graboske, Jr., *ibid.* 29, 35 (1976).
73. P. Bodenheimer, A. S. Grossman, W. DeCamp, G. Marcy, J. B. Pollack, *ibid.* 41, 293 (1980).
74. A. G. W. Cameron and J. B. Pollack, in *Jupiter*, T. Gehrels, Ed. (Univ. of Arizona Press, Tucson, 1976), p. 61.
75. J. S. Lewis, *Icarus* 16, 241 (1972).
76. R. Prinn and B. Fegley, *Astrophys. J.*, in press.
77. J. N. Cuzzi and J. B. Pollack, *Icarus* 33, 233 (1977).
78. J. Lissauer, F. H. Shu, J. N. Cuzzi, *Nature (London)* 292, 707 (1981); M. Hénon, *ibid.* 293, 33 (1981).
79. J. B. Pollack, J. A. Burns, M. E. Tauber, *Icarus* 37, 587 (1979).
80. W. Slattery, *ibid.* 32, 58 (1977).
81. S. A. Collins et al., *Nature (London)* 288, 439 (1980).
82. J. E. Keeler, *Astron. J.* 8, 175 (1889).
83. W. A. Baum et al., *Icarus* 47, 84 (1981).
84. J. N. Cuzzi et al., *Nature (London)* 292, 703 (1981).
85. F. A. Franklin and A. F. Cook, in preparation.
86. J. Luukkari, *Nature (London)* 292, 433 (1981); D. N. C. Lin and P. Bodenheimer, *Astrophys. J. Lett.* 248, L83 (1981); W. R. Ward, *Geophys. Res. Lett.* 8, 641 (1981).
87. P. Goldreich, private communication.
88. ——— and N. Borderies, private communication; M. Showalter, *Bull. Am. Astron. Soc.* 13, 728 (1981).
89. R. J. Terrile et al., *Bull. Am. Astron. Soc.* 13, 728 (1981).
90. With the completion of the second Voyager Saturn encounter, the Voyager spacecraft have now returned more than 62,000 images of Jupiter, Saturn, and their entourages. More than a

random accumulation of photographs, these images constitute carefully planned and executed time-lapse sequences of atmospheric, volcanic, or ring activity, multispectral mosaics of geologic surfaces, or extensive scans of small-scale ring structure. This treasure of stunning and informative pictures greatly exceeds the original imaging plans for Voyager and represents the successful efforts of several thousand talented individuals who have devoted their skills to this mission. A few of these people, those who are directly associated with this report, are listed below. J. B. Plescia (crater counts); L. A. Sromovsky (Saturn and Titan measurements); P. Thomas (satellite radiometry); T. C. Duxbury (Hyperion); P. Goldreich, J. J. Lissauer, E. Grün, G. Morfill (ring structure and formation);

S. W. Squyres (geology); J. L. Anderson, P. L. Jepsen, and G. M. Yagi (image processing); G. W. Garneau (atmospheric feature tracking for sequence predictions); G. P. Dimit, L. Garcia, D. Godfrey, A. Piumpunyalerd, E. T. Simien, and E. S. Thompson (data handling and manuscript preparation); JPL's photolab and graphics departments, Image Processing Laboratory, and Mission and Test Imaging System; and two reviewers, including M. J. S. Belton. G.E.H. is supported by the Science and Engineering Research Council, Great Britain. This report presents the results of one phase of research carried out at the Jet Propulsion Laboratory under NASA contract 7-100.

30 November 1981

Photopolarimetry from Voyager 2: Preliminary Results on Saturn, Titan, and the Rings

Abstract. *The Voyager 2 photopolarimeter was reprogrammed prior to the August 1981 Saturn encounter to perform orthogonal-polarization, two-color measurements on Saturn, Titan, and the rings. Saturn's atmosphere has ultraviolet limb brightening in the mid-latitudes and pronounced polar darkening north of 65°N. Titan's opaque atmosphere shows strong positive polarization at all phase angles (2.7° to 154°), and no single-size spherical particle model appears to fit the data. A single radial stellar occultation of the darkened, shadowed rings indicated a ring thickness of less than 200 meters at several locations and clear evidence for density waves caused by satellite resonances. Multiple, very narrow strands of material were found in the Encke division and within the brightest single strand of the F ring.*

Shortly after it left the Jupiter system and successfully acquired ultraviolet data on the Great Red Spot and the Jovian clouds (1, 2), the Voyager 2 photopolarimeter (PPS) experienced several operational difficulties. These were associated with the command-decoding processes, which control the analyzer and filter wheel positions (3). Extensive testing during the Jupiter-to-Saturn cruise phase of the Voyager 2 trajectory demonstrated several viable methods of instrument operation to accommodate these new PPS command modes. The data-acquisition technique used at Saturn generated measurements that had the following characteristics: (i) two-color character, ultraviolet at $2640 \pm 150 \text{ \AA}$ and deep red at $7500 \pm 125 \text{ \AA}$; (ii) orthogonal linear polarizations for each color sampled; and (iii) an eightfold increase in count rate discriminability for stellar occultation measurements. These enhanced performance characteristics made it possible for the Voyager 2 PPS to successfully measure the scattering properties of the Saturn and Titan atmospheres, as well as to make a single radial stellar occultation of Saturn's rings, and to measure partial phase curves for Iapetus, Rhea, Enceladus, and Phoebe.

The unfortunate scan platform anomaly that occurred near the crossing of the ring plane prevented acquisition of high-phase-angle data on Saturn and on all the satellites except Titan (4). Those partially completed studies will require more

sophisticated analyses (5). This report contains the initial results from the Saturn and Titan atmospheric scattering studies and the δ Scorpii stellar ring occultation.

Saturn's atmosphere. During the approach phase of the Voyager 2 spacecraft to Saturn, the PPS measured the intensity and polarization of light from Saturn. The instrument used an ultraviolet wavelength filter, 2640 Å, with a bandpass of 300 Å, and an infrared wavelength filter, 7500 Å, with a bandpass of 250 Å. In this report we discuss intensity measurements obtained for a portion of the east-west map of the northern hemisphere and a north-south measurement swath that gives information about the general reflectivity characteristics of Saturn's central meridian. Data for the east-west map were obtained during the Saturn approach at a distance of 4.2×10^6 km and a phase angle of 10.1° . The PPS instrument footprint is circular and had a diameter of 8000 km at this distance for the instrument's 0.11° field of view. The north-south data were obtained at a distance of 1.6×10^6 km and a phase angle of 17.0° , with the instrument footprint equal to 3100 km.

Figure 1a shows the 7500-Å east-west map of Saturn. The intensity is color-coded, with the highest count levels represented by white and the lower count levels represented by dark red. The brightest region on Saturn occurs near the equator just left of center, at the